Fabrication and Characterization of single-crystalline InP Membranes for several Applications

Christian-Albrechts-Universität Kiel
Faculty of Engineering
General Materials Science

Dissertation

zur Erlangung des akademischen Grades
Doktor der Ingenieurwissenschaften
(Dr.-Ing.)
der Technischen Fakultät
der Christian-Albrechts-Universität zu Kiel

written by
Mark-Daniel Gerngroß

Kiel, December 2013

1^{st} referee: Prof. Dr. Helmut Föll
2^{nd} referee: Prof. Dr. Jeffrey McCord
3^{rd} referee: Dr. Petra Granitzer

Day of disputation: May 14^{th}, 2014
Printing permission granted: May 14^{th}, 2014

Abstract

This work presents the fabrication process of single crystalline InP membranes in three steps – the electrochemical formation of an almost perfectly hexagonally close-packed array of currentline-oriented (curro) pores, the photo-electrochemical porosification of the bulk InP wafer back side, and the subsequent photochemical dissolution to open the curro-pore array. The photoelectrochemical and photochemical etching steps were investigated by *in situ* FFT-impedance spectroscopy (FFT-IS). The fitted FFT-IS data allowed to identify characteristic stages in the photo-electrochemical and in the photochemical step and to predict the morphology of the membrane surface after completion of the etching process. The membrane itself can be customized in a large variety starting with the thickness, over the membrane surface with flat or cone-like pore openings, even up to a self-organized 3D-structured highly crysto-porous layer on the membrane back side with an ultra-high surface area. The pore shape can be tuned from elliptic to perfectly rectangular by post-etching under cathodic bias. It also results in a further reduction and homogenization of the pore wall width compared to the state after electrochemical etching of the curro-pore array and a gain in resistivity of the membrane due to the increased SCR coverage of the InP pore walls.

In this work the fabrication of a multifunctional composite consisting of the piezoelectric InP membrane and a magnetic fillers in the form of nanowires and the usage of the InP membrane as anode in Li-ion batteries have been investigated. Multifunctional composites have been formed by galvanic metal deposition in InP pore arrays and membranes. Dense Ni and Fe-Co based nanowires were grown inside ultra-high aspect ratio InP membranes covered with a thin dielectric Al_2O_3 interlayer deposited by ALD prior to the galvanic deposition process. Without the dielectric interlayer only porous Ni nanowires, respectively tubular-like structures could be grown due to the preferential nucleation of Ni crystallites on the pore walls. The galvanic growth of Ni nanowires has been characterized by *in situ* FFT-IS. The fitted data allowed to separate the galvanic deposition into different stages and to consistently interpret them as the adsorption of boric acid on the growing Ni surface facilitating the deposition, the Ni deposition reaction itself, and the passivation of Ni surface by a diffusion-limited species. The magnetic characterization of the nanowires showed the easy magnetization direction of the Ni nanowires along the long nanowire axis z due to the ultra-high aspect ratio of the nanowires. In case of the Fe-Co based nanowires the easy magnetization direction is perpendicular to z. In both cases the coercivity exhibited a maximum in between $\boldsymbol{H} \parallel \boldsymbol{z}$ and $\boldsymbol{H} \perp \boldsymbol{z}$ which could be explained by a combination of two magnetization reversal mechanisms being each energetically favorable under certain angles α.

Porous InP membranes as anode in Li-ion batteries are free from additives, binders, or other passive materials unlike all other InP anodes and exhibit a very high capacity per

area. During lithiation the pore walls undergo drastic structural changes transforming InP into crystalline LiP and In_3Li_{13} becoming visible as oscillations in the pore wall widths in the form of a regular sequence of bulges and necks, in anti-phase to neighboring pore walls. They are even maintained in the delithiated state, when nanocrystalline InP is formed. No delamination or large scale pulverization of the pore walls were observed indicating the capability of porous anodes to compensate for the high volume expansion during lithiation. The cycling performance of the porous InP anode was good without capacity losses in the first cycles, but a progressive degradation in the following cycles. The application of an Al_2O_3 coating of the pore walls was beneficial for the SEI layer formation. The combination of Al_2O_3 coating and a lower discharge voltage limit reduced the gravimetric capacity to less than 50 % of the uncoated anode, but seemed to be beneficial for the cycling stability.

Kurzfassung

Diese Arbeit beschreibt den Herstellungsprozess von einkristallinen InP Membranen in drei Schritten – beginnend mit der elektrochemischen Herstellung von sogenannten "Stromlinien"- Poren ('curro' Poren) in einer beinahe perfekten, hexagonal-dichtest gepackten Anordnung, der fotoelektrochemischen Porosifizierung der Volumen InP Wafer-Rückseite und deren anschließende fotochemische Auflösung, notwendig zur vollständigen Öffnung der 'curro'-Poren. Die fotoelektrochemischen und fotochemischen Ätzschritte wurden zusätzlich per *in situ* FFT-Impedanz-Spektroskopie (FFT-IS) untersucht. Die gefitten FFT-IS Daten erlaubten die Identifikation von charakteristischen Etappen der fotoelektrochemischen und fotochemischen Ätzschritte, sowie die Voraussage der Oberflächenmorphologie der Membranen nach Beendigung der beiden Ätzschritte. Die Membran an sich kann in einer großen Vielfalt an die jeweilige Anwendung angepasst werden, beginnend bei der Membranendicke, über die Membranenoberfläche mit flachen oder konisch geformten Porenwänden; sogar eine selbstorganisierend enstandene, 3D-strukturierte, hoch 'crysto'-poröse Schicht auf der Membranenrückseite mit einer flächenmäßig ultra-hohen Oberflächen ist möglich. Die Porenform der Membran kann eingestellt werden von elliptisch bis perfekt rechteckig mittels Nachätzung unter kathodischer Vorspannung. Dies resultiert außerdem in einer weiteren Verringerung und Homogenisierung der Porenwände im Vergleich zur nur elektrochemisch geätzten Membran. Daneben führt die kathodische Nachätzung zu einem Anstieg des elektrischen Widerstands aufgrund einer stark erhöhten Ausbreitung der Raumladungszone in den InP Porenwänden.

In dieser Arbeit wurden die Herstellung von multifunktionalen Kompositen bestehend aus der piezoelektrischen InP Membran und eines magnetischen Füllers in Form von Nanodrähten sowie die Verwendung von InP Membranen als Anodenmaterial für Li-Ionen-Akkumulatoren untersucht. Die multifunktionalen Komposite wurden mittels galvanischer Abscheidung magnetischer Metalle in InP Porenarrays und InP Membranen hergestellt. Unporöse Ni und Fe-Co-basierende Nanodrähte konnten in InP Membranen mit einem ultra-hohen Aspektverhältnis hergestellt werden. Diese Membranen waren zuvor mit einer dünnen Schicht aus Al_2O_3 per ALD beschichten worden. Ohne diese dielektrische Zwischenschicht konnten nur poröse Ni Nanodrähte, bzw. tunnelartige Strukturen hergestellten werden mit einer bevorzugten Nukleation von Ni Kristalliten an den Porenwänden. Das galvanische Wachstum der Ni Nanodrähte wurde ebenfalls mittels *in situ* FFT-IS charakterisiert. Die gefitteten Daten erlaubten eine Aufteilung der galvanischen Abscheidung in einzelne Etappen, die konsistent interpretiert werden konnten als Absorption von Borsäure auf der wachsenden Ni-Oberfläche – was die Abscheidungsreaktion vereinfacht – als die Abscheidungsreaktion von Ni an sich und als Passivierung der Ni-Oberfläche durch eine diffusionslimitierte chemische Spezies. Die magnetische Charakterisierung der Nanodrähte zeigte, dass die einfach zu magnetisierende Richtung der Ni

Nanodrähte entlang der langen Nanodrahtachse z liegt aufgrund des ultra-hohen Aspektverhältnisses der Nanodrähte. Im Fall der Fe-Co-basierenden Nanodrähte liegt die einfach magnetisierbare Richtung senkrecht zu z. In beiden Fällen wies die Koerzitivfeldstärke ein Maximum zwischen $\boldsymbol{H} \parallel \boldsymbol{z}$ und $\boldsymbol{H} \perp \boldsymbol{z}$ auf, das durch eine Kombination von zwei Ummagnetierungsmechanismen erklärt werden konnte, die jeweils unter bestimmen Winkeln α energetisch bevorzugt sind.

Neben der Verwendung in multifunktionalen Kompositen können die InP Membranen auch als Anodenmaterial in Li-Ionen-Akkumulatoren eingesetzt werden, die ohne Additive, Bindemittel oder andere passive Materialien auskommen, im Gegensatz zu allen anderen InP Anoden. Die porösen InP Anoden wiesen eine hohe Kapazität pro Fläche auf. Während der Lithierung kommt es zu drastischen Strukturveränderungen der InP Porenwände. Hierbei wandelt sich InP in kristallines LiP und In_3Li_{13} um, was sichtbar wurde durch eine regelmäßige Sequenz von Ausstülpungen und Einschnürungen der Porenwände, jeweils in Gegenphase zu den benachbarten Porenwänden. Diese regelmäßige Sequenz blieb sogar im delithierten Zustand erhalten, nachdem sich nanokristallines InP gebildet hatte. Es wurden keinerlei Ablösungen oder großflächige Pulverisierung der Porenwände beobachtet. Dies zeigt, dass diese poröse Anode in der Lage ist, der hohen Volumenexpansion während der Zyklierung standzuhalten. Die Zyklierfähigkeit der porösen InP Anode war gut, da keine Kapazitätsverluste in den ersten Zyklen auftraten. In den folgenden Zyklen kam es dann allerdings zu fortschreitenden Kapazitätsverlusten. Die Verwendung von Al_2O_3 Beschichtungen der Porenwände war vorteilhaft für die Ausprägung eines SEI-Schicht. Die Kombination einer Al_2O_3 Beschichtung mit einer niedrigerer niedrigeren Entlade-Grenzspannung führte zu einer geringeren gravimetrischen Kapazität von etwa 50 % in Bezug auf die unbeschichtete Anode. Allerdings erschien diese Kombination vorteilhaft in Bezug auf die Zyklenstabilität.

Contents

List of Figures

Chapter 1

Introduction

Over the last 20 years the electrochemical micro and nanostructuring of semiconductors by electrochemical etching has arisen as a field of great scientific interest. The electrochemical formation of porous semiconductor materials has gained high interest especially after the discovery of macroporous and nanoporous Si by Föll, Lehmann, Gösele, and Canham [1, 2, 3] in the early years of the nineties, because it is a versatile technique to structure different kinds of semiconductor materials in a feasible way without using sophisticated equipment. Besides the afore mentioned porosification of Si, porous structures could be also formed by electrochemical etching in Ge [4, 5], in II-VI compound semiconductors – such as ZnSe [6], and also in III-V compound semiconductors – such as GaAs [7] or InP. In the case of InP, Takizawa et al. were the first to find crystallographically-oriented (crysto) pores in InP in 1994 [8]. From that point on, scientists around the world have been investigating the electrochemical formation of currentline-oriented (curro) pores and crysto-pores intensively for different carrier concentrations of InP [9, 10], different wafer surface orientations [11, 12], different acidic and alkaline anodization electrolytes [13, 14, 15], and for different electrochemical anodization parameters – from voltage controlled to current controlled conditions [16, 17].

In addition to the fabrication of porous materials by electrochemical etching also the galvanic deposition of ferromagnetic and non-ferromagnetic metals into porous materials has been widely investigated by the scientific community. Especially porous alumina (AAO) membranes have been widely used as template material after the discovery by Masuda [18]. Different metals, no matter if ferromagnetic or non-ferromagnetic, could be galvanically deposited in AAO membranes forming arrays of nanowires [19, 20, 21]. Besides these AAO membranes as template, it was reported for Si that Cu can be deposited in Si macropore arrays from the pore tip to the pore opening by current-controlled galvanic deposition [22, 23], but the deposition of ultra-high aspect ratio ($\geq$ 1000:1) coin metal nanowires was not possible so far. Besides this, it is reported that the deposition of ferromagnetic metals, such as Ni or Co, in Si pore arrays, resulted in the deposition of agglomerated Ni resp. Co crystallites on the pore walls, but not in the formation of dense nanowires [24, 25, 26]. For InP, it had already been shown that it is possible to homogeneously coat the pore walls of an electrochemically etched pore array with coin metals, such as Cu and Pt by pulsed current deposition [27, 28]. Anyhow a galvanic deposition of solid metal nanowires could not be achieved so far in InP pore arrays. The deposition of ferromagnetic nanowires inside InP pore arrays or membranes is of specifically high interest for the fabrication of a magnetoelectric composite being used for

magnetoencephalographic or magnetocardiographic sensors.

A world without Li-ion batteries can not be thought of anymore. So many devices use Li-ion batteries, from consumer electronics over PC and cell phones up to even modern airplanes like the Boeing 787 Dreamliner. But for the large-scale energy storage, necessary e.g. for operating electric cars, the capacity of the battery needs to be increased drastically. Besides Si [29, 30], metal phosphides are an option. In general they allow for gravimetric capacities larger than currently obtained by conventional graphite anodes [31]. Although metal phosphides are not offering the highest gravimetric capacity among the materials forming an alloy with Li, InP as one representative of this group has one big advantage compared to the other metal phosphides. InP can be easily nanostructured by electrochemical / photochemical etching, thus, making it suitable to serve as a model system to study the influence of porosification, coatings etc. on the battery characteristics of the anode and the lithiation / delithiation process itself. State of the art InP anodes for Li-ion batteries are thin film anodes that are deposited on a stainless steel foil as substrate either in a slurry form [32] or by pulsed laser deposition [33]. Since these anodes are thin film anodes, they have an active layer of only several hundreds of nanometers in maximum and thus, a very small energy density due to the steel substrate. On the other hand thin films are highly beneficial for the diffusion of Li into the InP resulting in a higher power density compared to the bulk material. In this work, the energy density of the anode could be increased by fabricating three dimensional structures as active layer with and maintaining the feature size of the thin film anodes, so that the high power density of the thin film anodes can be sustained. The energy density of the anode can be further increased if the heavy substrate [32, 33] and special binders [32] could be avoided, because they add substantial weight to the anode, thus decreasing the energy density of the overall anode.

The present work can be structured into three parts. The first part describes the three-stepped fabrication process for a single-crystalline InP membrane combining electrochemical, photo-electrochemical, and photochemical etching. Additionally, the membrane fabrication process is investigated using FFT impedance spectroscopy. The membrane properties are widely adjustable either during the fabrication process or by post-treatments. A very important post-treatment is the post-etching under cathodic bias that was also developed in the present work.

The second part deals with the galvanic deposition of magnetic nanostructures, such as nanocrystals resp. nanowires based on Ni and FeCo into the previously described porous InP membranes. The problem of the preferential deposition on the membrane pore walls could be circumvented by coating the InP membrane with a thin layer of Al_2O_3 by atomic layer deposition (ALD) resulting now in parallel, highly ordered magnetic nanowires. The magnetic properties of the ferromagnetic nanostructures are investigated by a vibrating sample magnetometer (VSM). This 1-3 composite combines the piezoelectric property of the porous InP membrane and the magnetostrictive property of the magnetic nanowires making it a potentially magnetoelectric composite.

The third part is about the application of porous InP membranes as novel anode material for Li-ion batteries that is three-dimensionally structured being substrate and binder free and electrically contacted by a thin current collector consisting of Au or Cu. The fabricated anode is characterized by standard battery cycling experiments and cyclovoltammetry. All InP structures and galvanically deposited Ni and FeCo nanostructures are structurally investigated by scanning electron microscopy (SEM) and x-ray diffraction

(XRD) additionally to the previously stated investigations.

The present work consists of six chapters in total. Chapter 2 provides the required theoretical background for this work, while in Chapter 3 the experimental setup is described. Chapter 4 presents the results of the measurements which are discussed in Chapter 5. Chapter 6 provides a summary about the obtained new knowledge and gives perspectives for future research.

Chapter 2

Theory

2.1 Electrochemical pore formation in InP

2.1.1 The crystal system of InP

Indium phosphide is a representative of the III-V compound semiconductors with a direct band gap of 1.34 eV [34]. Indium phosphide crystallizes in a face-centered cubic structure with a diatomic basis. The atom positions are at (0, 0, 0) and (¼, ¼, ¼) as depicted in unit cell in Fig. 2.1 a). In the base, the In and P atom are placed. This crystal structure

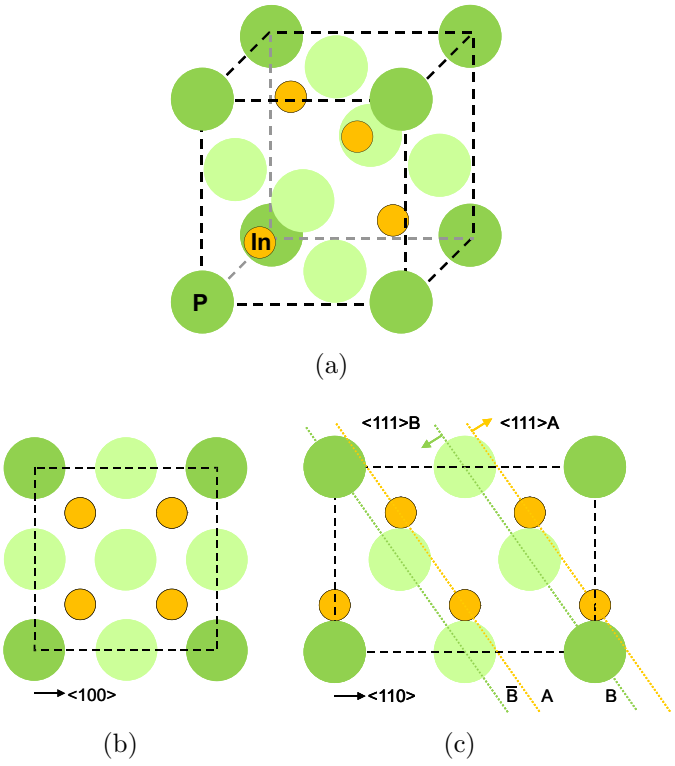

Figure 2.1: Schematic view on the a) InP unit cell, b) {100} plane, and c) {110} plane. The large balls represent P atoms, the small balls In atoms. The dark green balls represent the atoms at the corner of the cube, the light green face-centered atoms, and the yellow balls the atoms in the tetrahedral positions.

is commonly referred to as zinc blende structure, in the Hermann-Mauguin notation $\bar{4}3m$. The zinc blende crystal structure has two sets of planes that contain one kind of atoms. In the present case of InP, either In atoms or P atoms. The two sets of planes are the {100} and the {111} planes. Figure 2.1 b) provides a cut through the unit cell in ⟨100⟩ direction showing constant distances between {100} planes, since two bonds are between the atoms of two adjacent {100} planes.

The zinc blende crystal system is non-centrosymmetric exhibiting an anisotropy in the {111} planes which gives rise to the piezoelectric behavior [34]. This anisotropy is illustrated by the cut through the unit cell in ⟨110⟩ direction in Fig. 2.1 c). This cut shows the {111} planes that contain either only In atoms or P atoms. The {111} planes that are terminated by In are named {111}A, while the P terminated planes are called {111}B. The same nomenclature is true for other zinc blende III-V semiconductors [35]. In particular, the (111), $(\bar{1}\bar{1}1)$, $(\bar{1}1\bar{1})$, and $(1\bar{1}\bar{1})$ planes are In terminated, the remaining four {111} planes are P terminated. From Fig. 2.1 b) can be seen that the distance between {111} planes is not constant, but depends on the termination of the plane. The distance between the planes A and $\overline{\text{B}}$ is short, while it is long for the distance between A and B. The origin of these different distances lies in the different bonding situation. Three bonds are formed between the atoms of the planes A and $\overline{\text{B}}$, while there is only one between atoms of the planes A and B. This difference in the number of bonds between {111} planes has direct consequences for the chemical dissolution rate, meaning the dissolution rate of {111}B planes is higher than of {111}A planes. The etching rate of {100} planes lies in between [34].

2.1.2 Pore formation in InP

In [36], Gerischer and Mindt describe the electrochemical dissolution of semiconductors in terms of chemical reaction equations with special emphasis on the role of holes and electrons.

Compound semiconductors typically consist of a more electronegative and a less electronegative constituent. The strength of chemical bonds between atoms can be weakened by two mechanisms. The first mechanism is to introduce a hole in the bonding orbital. The second possible mechanism is to add an electron in the non-bonding orbital. It depends strongly on the activation energy of each process which mechanism is preferred for weakening the bonds at the semiconductor surface. The approximate difference between both activation energies is proportional to the band gap of the semiconductor. Thus, for high band gap semiconductors, the bond weakening almost exclusively occurs via holes. The concentration of holes at the interface of the semiconductor and the electrolyte depends on the magnitude of the applied anodic potential and increases exponentially with increasing anodic potential [36].

In the next step the less electronegative constituent is preferentially attacked by the more electronegative etching species coming from the electrolyte. The less electronegative atom is removed from the surface of the semiconductor. The involved electronic charge carriers are consumed and the etching reaction stops if no further charge carriers are supplied. The supply of holes is obtained by avalanche breakdown in the semiconductor as described in section 2.2.1.

Besides the role of single holes and electrons in the electrochemical dissolution described above, the further have a strong impact on the dissolution, such as passivation of

the semiconductor surface. The passivation can occur either by the formation of an oxide layer at the semiconductor surface or by chemisorbed ions from the electrolyte. In the case of passivation by an oxide layer, various kinds of oxides ($InPO_4$, In_2O_3, $In(PO_3)_3$) have been observed in InP under various chemical/electrochemical conditions [37]. In aqueous electrolytes the passivating ions are mostly H^+ [38] or OH^- [39]. In the case of III-V semiconductors it has been observed that Cl^- ions can passivate the surface [40].

Crystallographically oriented pores

Crystallographically-oriented pores (crysto-pores) were first discovered in InP by Takizawa in 1994 [8]. This kind of pores got its name because the pore grows along certain crystallographic directions. In n-type InP this is along ⟨111⟩B directions. Crysto-pores have a distinct growth procedure which was investigated in [41]. Starting from an etched tetrahedron enclosed by {111}A planes, the pore grows from a corner of the tetrahedron in ⟨111⟩ B direction as a string of tetrahedrons. In the following the transition zone between connected tetrahedra is dissolved purely chemically forming the pore walls of the crysto-pore. The crysto-pore is then enclosed by {112} planes forming an equilateral triangle as cross-sectional area of the pore. A cross-sectional view on a typical crysto-porous layer is depicted in Fig. 2.2 a). The upwards and downwards going 'channels' are cut along crysto-pores. The single triangles that are presented in high magnification in Fig. 2.2 b) are crysto-pores that are cut in cross-section.

Since all four corners are equal, the crysto-pore can grow in any of the four ⟨111⟩B directions, in principle. For example, the crysto-pore grows downwards (looking from the surface where the pore growth starts from) and after some time a new crysto-pore grows upwards out of the initial pore. This is also illustrated in the upper left part of Fig. 2.2 a). This feature observed in crysto-pores is a phenomenon called branching. Branching describes the nucleation and growth of a new pore out of an already existing pore. It can occur in two different ways, the branching at the pore tip in one of the possible ⟨111⟩ B directions and the branching out of the pore wall. The angle between two branched pores is 109°. In case of branching at the pore tip, it depends on the growth direction

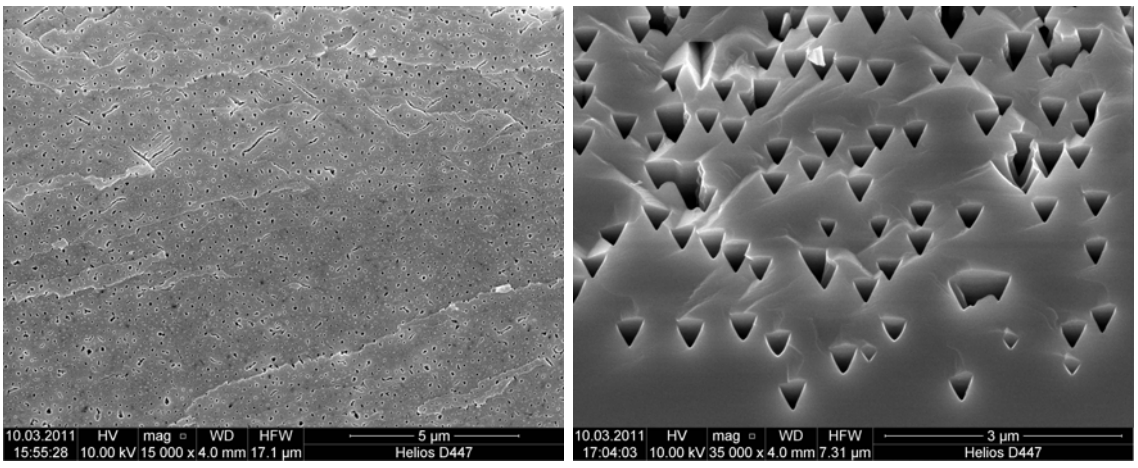

(a) (b)

Figure 2.2: InP crysto-pore array in a) cross-section, (110) plane, and b) in high magnification.

of the crysto-pore in which direction the branched pore grows. If the crysto-pore grows downwards either in the $[\overline{1}\overline{1}\overline{1}]$ or $[11\overline{1}]$ direction. The branching from the pore tip occurs then in the other respective direction, e.g $[\overline{1}\overline{1}\overline{1}]$ as growth direction of the initial crysto-pore, branching in $[11\overline{1}]$. Branching out of the pore walls results in upwards growing crysto pores either in $[1\overline{1}1]$ or $[\overline{1}11]$ direction in case of an initially downwards growing pore. Of course the upwards growing pores can branch at the pore tips either in $[1\overline{1}1]$ or $[\overline{1}11]$ direction depending on the growth direction of the initially upwards growing crysto-pore. The branching from the pore walls of upwards growing crysto-pores results in downward growing crysto-pores.

It has been also observed by Langa that if the tip of a crysto-pore approaches the pore wall of a neighboring crysto-pore, it stops growing before penetrating the pore wall of the other crysto-pore. The intersection of two crysto-pores is only possible when the tips of two neighboring crysto-pores meet. In this case both crysto-pores continue growing after forming a crossing [42].

The differentiation between upwards growing and downwards growing crysto-pores is very easy from corresponding SEM images. Since natural cleavage planes for single-crystalline (100) InP are the (110) and the $(1\overline{1}0)$ planes, the crysto pores are either lying in-plane or form penetration points in the shape of triangles. In (110) planes, the upwards growing crysto-pores are in-plane and the downwards growing ones out-of plane. The corner of the triangle points downwards. The situation is vice versa for $(1\overline{1}0)$ planes.

Since the electrochemical growth of crysto-pores is in principle only a feature of the non-centrosymmetric crystal system, crysto-pores are not solely found in InP, but also in Si [43] and other III-V semiconductors, such as GaAs [7], GaP [44]. In n-type InP, crysto-pores can be obtained in a multitude of different electrolytes from alkaline (KOH [15]) over NaCl [45] to acidic electrolytes (HCl [8]).

Current-line oriented pores

Currentline-oriented pores (curro-pores) were discovered shortly after the discovery of crysto-pores [46]. Curro-pores typically grow at higher current densities in contrast to crysto-pores [47]. The curro-pores nucleate self-organized from a nanometer-sized nucleation layer consisting of crysto-pores. Unlike crysto-pores, curro-pores do not grow only along certain crystallographic directions, but grow perpendicular to the equipotential surfaces, along the direction of current flow as depicted in Fig. 2.3 a). That is why the growth direction of curro-pores does not depend on the crystallographic orientation of the wafer. The shape of curro-pores is columnar varying from perfectly round over elliptic up to rectangular in cross-section depending on the carrier concentration. Ideally, curro-pores are found to grow in a perfectly hexagonally close-packed arrangement. Curro-pores do not intersect each other. The minimum distance between neighboring pores is twice the SCR width during the electrochemical etching process which strictly depends on the applied anodic etching potential and on the carrier concentration of the substrate. With increasing carrier concentration also the curvature of the curro-pore tip increases [9].

The growth rate of the curro-pore array is much higher compared to the crysto-pores. Typical growth rates of about 30 µm/s have been observed highly depending on the electrolyte transport efficiency into the curro-pores [47]. The growth rate typically decreases exponentially for pore lengths of several hundreds of micrometers. The length of the curro-pores can be controlled by the etching time [48]. Besides InP, the growth of curro-

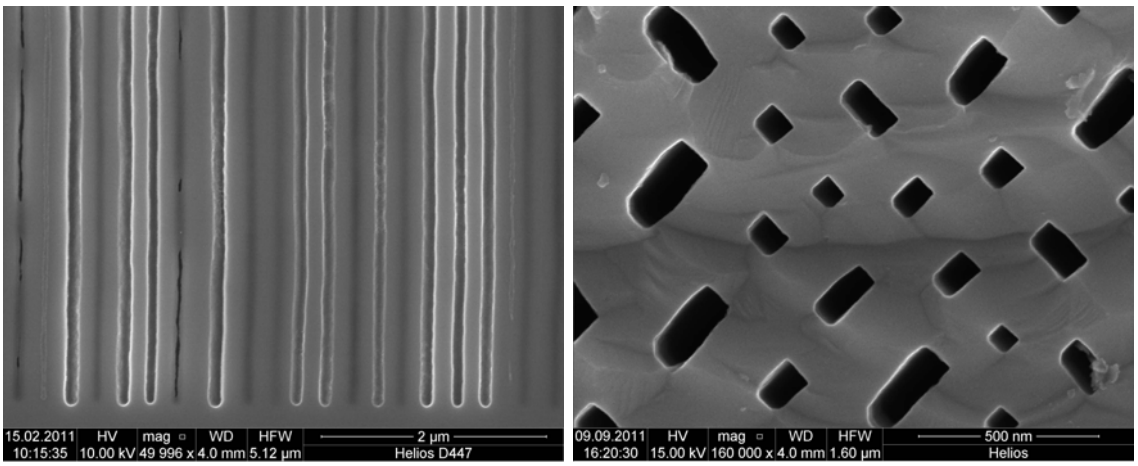

(a) (b)

Figure 2.3: InP curro-pore array in a) cross-section and b) top view after removal of the nucleation layer.

pores is also documented for Si [3], other III-V semiconductors [49], and also for II-VI semiconductors [6, 50]. Depending on the applied voltage or the applied current density respectively, transition between crysto and curro-pores is observed. The transition from crysto-pores to curro-pores is not necessarily sharp, but can involve the formation of curristo-pores, a mixture of curro-pores and crysto-pores.

2.2 Semiconductor contacts

2.2.1 Semiconductor–metal interface

The semiconductor–metal junction is a very well understood interface. There are four different cases of a semiconductor-metal interface depending on the doping of the semiconductor (p- or n-type) and on the work function of the metal with respect to the work function of the semiconductor (ϕ_{metal} higher or lower than ϕ_{semi}). In the present work only n-type semiconductors are used, thus, the p-type semiconductor-metal interface is not considered in the following. In Fig. 2.4 the energy band diagrams before and after a contact is formed between an n-type semiconductor and a metal are displayed for $\phi_{\mathrm{semi}} < \phi_{\mathrm{metal}}$ and $\phi_{\mathrm{semi}} > \phi_{\mathrm{metal}}$ for perfect interfaces, i.e. without surface states.

The work function ϕ is the energy necessary to directly transfer an electron from the solid positioned at the Fermi level E_F into vacuum. The electron affinity χ for solids is the energy difference between the vacuum level E_{vac} and the edge of the conduction band E_C. At ambient temperature, the Fermi level E_F of an n-type semiconductor is positioned near the donor level. The difference between the edge of the conduction band and the valance band E_V is the band gap energy E_{gap} of the semiconductor.

Schottky contact

A Schottky contact forms for a contact between an n-type semiconductor and a metal with a higher work function than the one of the n-type semiconductor assuming a per-

fect semiconductor surface at the contact. The resulting band structure after contact formation is depicted in Fig. 2.4 b).

The contact formation occurs typically at elevated temperatures, e.g by physical vapor deposition or chemical vapor deposition. At this temperature condition, the semiconductor is an intrinsic conductor with the Fermi level near the middle of the band gap. The Fermi levels of the n-type semiconductor and the metal align. At room temperature, the Fermi level of the n-type semiconductor shifts in between the conduction band edge and the donor level. This shift in the Fermi level is accompanied by a band bending directly at the semiconductor–metal interface and thus, by a change in the electron concentration in the conduction band. The maximum barrier height $V_{barrier}$ is determined by the difference between the electron affinity χ of the n-type semiconductor and the metal work function ϕ_{metal}. Due to the bend bending the n-type semiconductor is depleted from electrons in the close proximity of the interface. This region is typically called depletion layer or space charge region (SCR). In this SCR ionized donors are distributed over a larger region as positive space charges. This is due to the comparatively lower concentration of donor

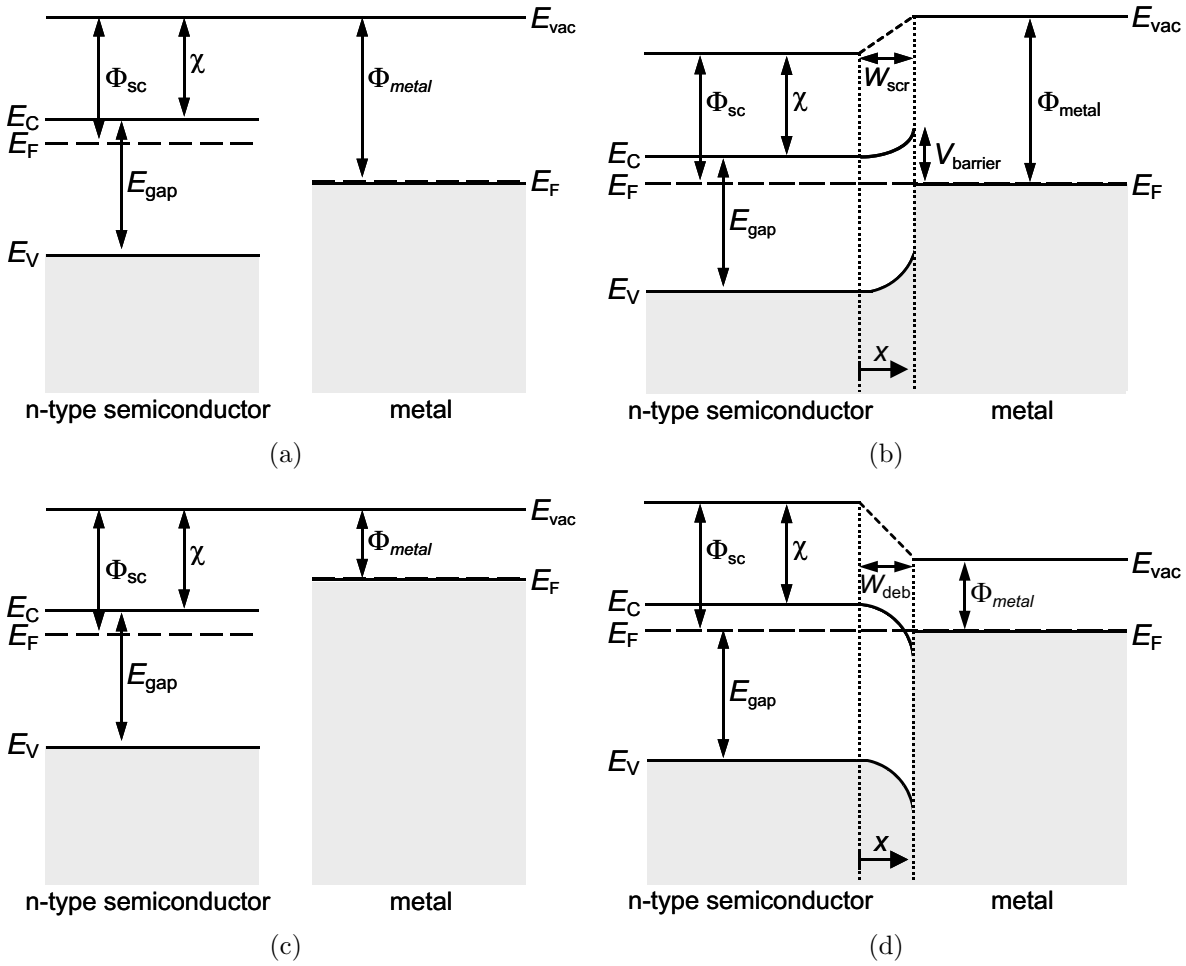

Figure 2.4: Schematic energy band diagrams for n-type semiconductor-metal junctions, (a) with $\phi_{\text{semi}} < \phi_{\text{metal}}$ before contact and (b) after the formation of a contact, c) with $\phi_{\text{semi}} > \phi_{\text{metal}}$ before contact and d) after the formation of a contact. The width of the SCR W_{scr} is larger by orders of magnitude compared to the Debye length W_{deb}.

atoms in the n-type semiconductor. The charge of these positive space charges is directly compensated in the metal by an equal amount of electrons giving rise to an electric field in the SCR and thus, to a voltage V in the SCR. The width of the SCR W is calculated using the Poisson equation. The one-dimensional Poisson equation is given in Eq. 2.1 with the following parameters, the voltage V at position x, the charge density ρ, the vacuum permittivity ϵ_0, and the relative permittivity ϵ_r of the semiconductor.

$$-\frac{\mathrm{d}^2 V_{(x)}}{\mathrm{d}x^2} = \frac{\rho_{(x)}}{\epsilon_r \epsilon_0} \tag{2.1}$$

$$\rho_{(x)} \approx qN_D \qquad x \leq W \tag{2.2}$$

$$\rho_{(x)} \approx 0 \qquad x > W \tag{2.3}$$

$$\frac{\mathrm{d}V}{\mathrm{d}x} = 0 \qquad 0 > x > W \tag{2.4}$$

Using the approximation for an abrupt pn-junction with the boundary conditions given in Eqs. 2.2 – 2.4, leads to a width of the SCR given in Eq. 2.5 with the built-in potential V_{bi} as additional parameter. The built-in potential is determined by the difference in the Fermi energies of both materials.

$$W = \sqrt{\frac{2\epsilon_0 \epsilon_r}{qN_D} \cdot V_{bi}} \tag{2.5}$$

Applying a negative voltage to the semiconductor–metal contact (negative pole of the voltage source connected to the semiconductor) is called cathodic biasing. This leads to a diminishment of the SCR, because the band bending is reduced and thus, the electron concentration is increased. The width of the SCR and the potential barrier height $V_{barrier}$ decrease.

The application of a positive voltage to the semiconductor–metal contact (anodic bias) leads to an enlargement of the SCR, because the band bending is increased resulting in a lower electron concentration and an increased $V_{barrier}$. If the band bending is so strong that the Fermi level is below the band gap mid, holes become the majority charge carrier close to the interface. This results in an inversion layer in the n-type semiconductor in the dimensions of a Debye length. The SCR is still present.

In case of high enough electric fields, avalanche breakdown occurs. Free charge carriers present in the SCR are accelerated due to the electric field of the SCR. Electron-hole pairs are formed by collisions of the accelerated charge carriers with electrons from the valance band. These charge carriers themselves are accelerated by the electric field in the SCR and generate new electron-hole pairs. An avalanche forms with an exponentially increasing concentration of free charge carriers.

Ohmic contact

An ohmic contact forms for a contact between an n-type semiconductor and a metal with a lower work function than the one of the n-type semiconductor assuming a perfect semiconductor surface. The resulting band structure after contact formation is depicted in Fig. 2.4 d).

The contact between both components is formed in the same way as described for the Schottky contact, the Fermi levels of the semiconductor and the metal align. When reducing the temperature to room temperature again, the Fermi level of the n-type semiconductor is shifted in between the conduction band edge and the donor level. As consequence, the conduction band edge and the valence band edge are bent downwards. The conduction band can even bent under the Fermi level as depicted in Fig. 2.4 d). The band bending is accompanied by an increase in the electron concentration in the conduction band at the interface. This region is called the Debye length. The Debye length W_{deb} is by orders of magnitude smaller than the width of the space charge region W_{scr}, because the electrons are free charge carriers and not stationary as the donor atoms. The increased electron concentration in the semiconductor at the interface causes a decreased electron concentration in the metal directly at the interface of only a few Angstroem. This region is also called Debye length, but is not an obstacle for the transport of electrons, since they can easily tunnel through this layer. The width of the Debye length in the metal is much smaller than the Debye length in the semiconductor.

Applying a negative voltage to the semiconductor–metal contact facilitates the electron flow from the semiconductor into the metal, since the band bending is increased. The contact remains ohmic.

The application of a positive voltage to the semiconductor–metal contact facilitates the electron flow from the metal into the semiconductor, since the band bending is decreased. The contact remains ohmic.

2.2.2 Semiconductor–electrolyte interface

The interface between an electrode and the electrolyte is often described by the Grahame model. It combines the Helmholtz model with rigid ions at the interface and the Gouy-Chapman model with a diffuse double layer [51].

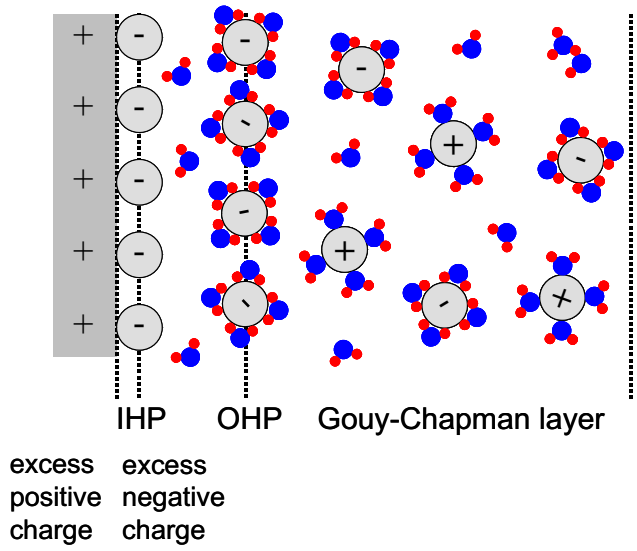

Figure 2.5: Schematic representation of the Grahame model of the interface between the semiconductor surface and the electrolyte with the inner Helmholtz plane (IHP), the outer Helmholtz plane (OHP), and the Gouy-Chapman layer.

In the inner Helmholtz plane (IHP) the electrolyte ions dispensed their solvation shell and are attached to the surface atoms of the electrode compensating the charge of the surface. In the outer Helmholtz shell (OHP) the electrolyte ions still have their solvation shell. In the adjacent Gouy-Chapman layer the ions in the electrolyte are randomly distributed due to the disordering effect of thermal fluctuations that can be described by the Boltzmann distribution. The IHP is in the dimension of several molecule monolayers between 1 and 10 Å, the OHP about 10 Å, and the Gouy-Chapman layer about 10 nm. These dimensions strongly depend on e.g. the concentration of the ions in the electrolyte, the externally applied voltage, and the electrolyte temperature.

Due to the high degree of order in the rigid arrangement of the electrolyte ions in the Helmholtz layer the voltage drops linearly with a higher slope till the IHP and with a lower slope till the OHP. In the Gouy-Chapman layer the voltage decreases exponentially.

The capacity of the electrode/electrolyte interface is a series connection of the effective capacity of the Helmholtz layer and the capacity of the Gouy-Chapman layer. The capacity of the Helmholtz layer can be approximated by a plate capacitor, while the capacity of the Gouy-Chapman layer is more complex and derived in detail in [52].

Semiconductor–electrolyte contact

The semiconductor is well described by the electronic band structure, which is not directly transferable to the electrolyte. An electrolyte consists of ions that can be oxidized and reduced. Each state is associated with a specific energy. The oxidized state E_{ox} is the energetically higher positioned state, the reduced state E_{ed} the energetically lower state. In aqueous electrolytes each ion is enclosed by a solvation shell that can vary due to thermal fluctuations. Thus, the energy necessary for oxidization or reduction also varies. The energies E_{ox} and E_{red} are mean values of the typically Gaussian distributed oxidization and reduction energy. The electrolyte does not have a Fermi level *per se*, but a similar quantity, the electrochemical redox potential E_{redox}. This is schematically depicted in Fig. 2.6 a).

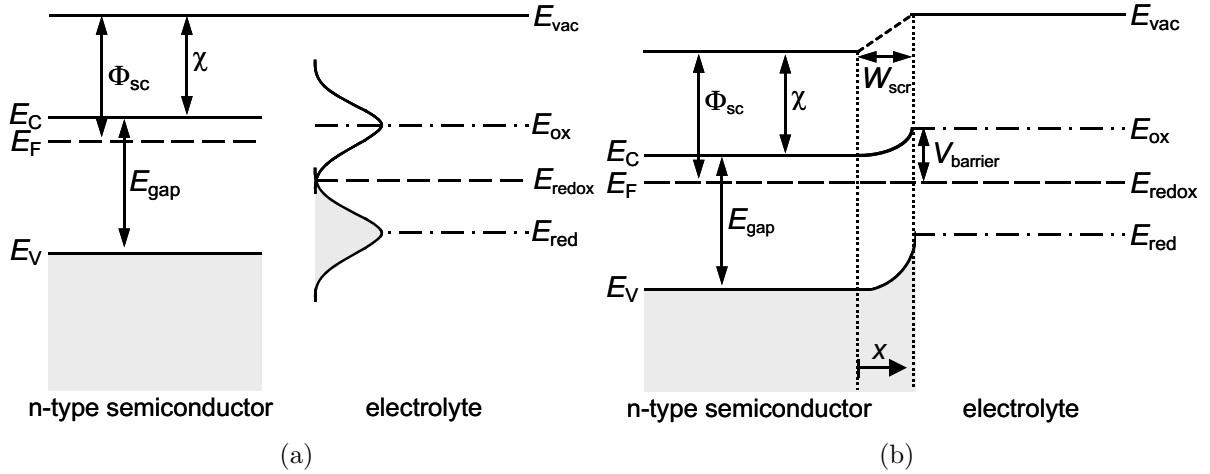

Figure 2.6: Schematic energy band diagrams for an n-type semiconductor-electrolyte junction, (a) before contact including the energy distribution function of the oxidized and reduced state of ions in the electrolyte and (b) after the contact formation.

The redox potential of an electrolyte can be calculated by the Nernst equation given in Eq. 2.6. It consists of the standard electrode redox potential (mean value of E_{ox} and E_{red}) E°_{redox}, the universal gas constant R, the temperature T, the mole number of exchanged electrons z, the Faraday constant F, and the concentration of the oxidized c_{ox} and of the reduced species c_{red}.

$$E_{redox} = E^{\circ}_{redox} - \frac{RT}{zF} \ln \frac{c_{\mathrm{ox}}}{c_{\mathrm{red}}} \tag{2.6}$$

The semiconductor–electrolyte interface can be described in a similar manner as the Schottky contact. The resulting band structure after contact formation is depicted in Fig. 2.6 b). After contact formation the Fermi level and the redox energy align due to a charge flow from the semiconductor into the electrolyte. The electrons originate from the ionized donor atoms in the semiconductor. An SCR develops with the corresponding band bending of the conduction and valence band. The SCR can be calculated in the same ways as presented in section 2.2.1. The same holds for the behavior under anodic and cathodic bias.

2.2.3 Semiconductor and its surface

The above described contacts assume always a perfect semiconductor surface at the interface. The surface of a semiconductor is mostly imperfect, because the bonding situation of the outermost atom layer is different from the bulk. The binding partners of the outermost atom layer are missing, so that dangling bonds at the surface are the consequence. The number of dangling bonds can be reduced by surface reconstruction. As a direct consequence of the different bonding situation at the surface, the band structure changes as well. So called surface states positioned in the band gap pin the Fermi level which has to lie in between the surface states so that charge neutrality is maintained. Since the Fermi level is positioned between the conduction band edge and the donor level in the bulk for an n-type semiconductor, the Fermi levels are different between the surface and the bulk. This case can be described analogue to the Schottky contact between an- type semiconductor and a metal with a higher metal work function.

2.3 Impedance spectroscopy

2.3.1 Impedance

The impedance Z is the electric resistance in an alternating current (AC) circuit. Following Ohm's law, it is defined as the complex ratio of the voltage U and the current I in an AC circuit, see Eq. 2.7. In direct current (DC) circuits the impedance is equal to the resistance R.

In contrast to the resistance R in DC circuits, the impedance is given either in the polar form as a function of the angular frequency ω or the phase ϕ and the amplitude $\tilde{Z}$ or separated into real and imaginary part, as shown in the following formulas, Eq 2.8 and 2.9.

$$Z = \frac{U_{(t)}}{I_{(t)}} \tag{2.7}$$

$$Z_{(\omega)} = \tilde{Z}\exp(i\,\omega t) = \tilde{Z}\exp(i\phi) \tag{2.8}$$

$$Z_{(\omega)} = \mathrm{Re}(Z_{(\omega)}) + i\,\mathrm{Im}(Z_{(\omega)}) \tag{2.9}$$

Generally, the electric circuit is built out of simple electrical elements such as resistors, capacitor and inductors. The corresponding impedance $Z_{(\omega)}$ for a resistor is R for a capacitor $1/i\omega C$ and for an inductor $i\omega L$. These electric elements can be arbitrarily combined in series, in parallel or as combinations of both.

There are several ways to graphically visualize the impedance. A typical way is the Bode plot. Here, the real part and the imaginary part of the impedance Z are plotted separately over the logarithm of the angular frequency ω. This is exemplarily sketched in Fig. 2.7 b). The frequency behavior is directly accessible. Another possibility for visualizing the impedance is the Nyquist plot. The imaginary part of the impedance is plotted over the real part of the impedance as schematically shown in Fig. 2.7 b) for a single RC element. The frequency dependence of the impedance is not directly accessible from the plot compared to the Bode plot. Nevertheless, for the two edge cases, $\omega \to 0$ and $\omega \to \infty$, the frequency dependence of Z is directly visible – Z approaches zero.

In the following impedance analysis, the Bode and the Nyquist plot are used for the fitting of the impedance data as a qualitative measure for the conformance of the measured and fitted impedance.

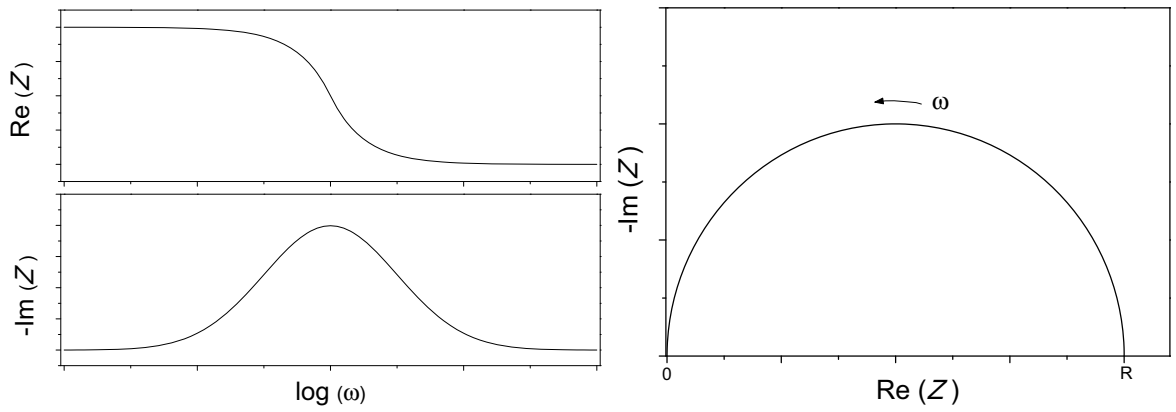

Figure 2.7: a) Bode plot and b) Nyquist plot of a single RC element.

2.3.2 FFT-impedance spectroscopy

The FFT-impedance spectroscopy (FFT-IS) is a modification of the classical impedance spectroscopy for dynamic systems. Impedance spectroscopy in general is the impedance measurement of a system for various discrete AC frequencies [53]. This is achieved by modulating the DC current applied to the system with a sinusoidal AC perturbation current. The system responds to this perturbation with a phase shift ϕ in the measured AC voltage. The impedance of the system is given in Eq 2.10 with the voltage amplitude

$\tilde{U}$, the current amplitude $\tilde{I}$, the angular frequency ω, and the time t. The DC share in this formula is neglected, since it results only in a constant offset of the impedance.

$$Z(\omega) = \frac{U_{AC}}{I_{AC}} = \frac{\tilde{U}\ \exp(i\omega t + i\phi(\omega))}{\tilde{I}\ \exp(i\omega t)} = \tilde{Z}\ \exp(i\phi(\omega)) \tag{2.10}$$

FFT-impedance spectroscopy in particular has the advantage of applying a perturbation signal to the applied current with typically 30 or more different frequencies at the same time compared to standard impedance spectroscopy. For performing reasonable impedance measurements certain requirements must be fulfilled [53]. The first is, the measurement must not change the system to be investigated. The second is, the response signal of the system must only be caused by the applied perturbation signal. Thirdly, the system must linearly reply to the perturbation signal. Fourthly, the impedance measurement must be quick enough so that the system to be investigated does not change during the measurement.

A typical perturbation signal of the current and the corresponding response of the system is shown in Fig. 2.8 a). Since the amplitude and the frequencies of the perturbation signal are known, the unknown amplitude and frequency of the system response can be determined by a Fourier transformation from the time domain to the frequency domain. The result is shown in Fig. 2.8 b). From this the phase shift and the amplitude of the response signal can be obtained allowing to calculate the impedance in the next step according to Eq. 2.10.

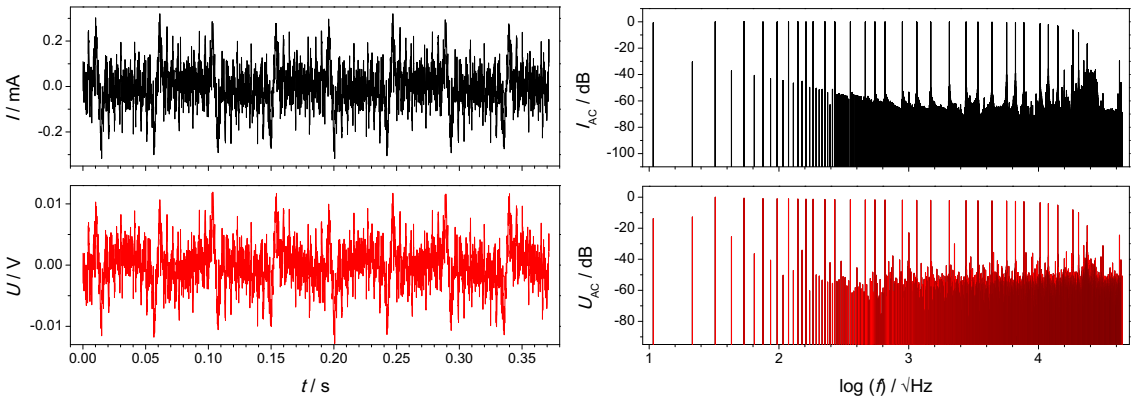

(a) (b)

Figure 2.8: FFT-IS measurement a) perturbation signal I and the response of the system in the time domain and b) power spectrum of the perturbation signal I and the system response of the same measurement in the frequency domain.

Fit models

The impedance of the electrochemical system can be mathematically described by a differential equation. Since only the linear response to the applied perturbation signal is of interest and not higher order effects, the differential equation simplifies drastically. This simplified differential equation can be described by an electrical equivalent circuit, which is expressed as a combination of electric components, such as resistor, capacitors, inductors, and combinations of these. Having a matching model system allows to perform a

numerical fitting for the measured impedance data to extract the quantities associated to each component present in the equivalent circuit. In the second step, these components can be related to their chemical, respectively physical origin. For example, resistors could be related to the electrolyte resistance, capacitors to space charge regions, time constants to the participating electrochemical / chemical reactions.

In this work only the two models presented in Fig. 2.9 consisting of a series resistance R_s in series with RC elements. The RC element is made of a transfer resistor R_p and a capacitance C_p. The equivalent circuit of the first model consists of a series resistor and a single RC element. The total impedance is given in Eq. 2.11. This model is extended by adding two more RC elements in the Maxwell arrangement forming the equivalent circuit for the second model. The total impedance is given in Eq. 2.12.

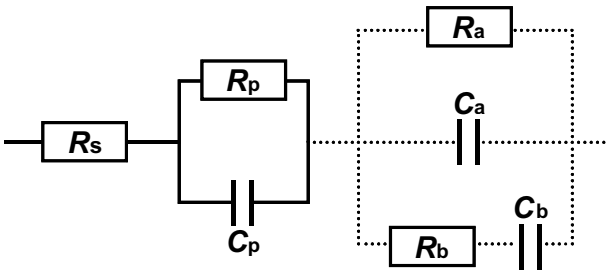

Figure 2.9: Equivalent circuit for fitting of impedance data consisting of a series resistance and one RC element (solid line). It can be easily extended to a three RC element model (dotted line) in the Maxwell arrangement.

$$Z_{(\omega)} = R_S + \frac{R_p}{1 + \mathrm{i}\omega R_p C_p} \tag{2.11}$$

$$Z_{(\omega)} = R_S + \frac{R_p}{1 + \mathrm{i}\omega R_p C_p} + \frac{1}{\frac{1}{R_\mathrm{a}} + \mathrm{i}\omega C_\mathrm{a} + \frac{i\omega C_\mathrm{b}}{i\omega R_\mathrm{b} C_\mathrm{b} + 1}} \tag{2.12}$$

2.4 Determination of the crystallite sizes

The Scherrer formula is commonly used to estimate the particle size of crystallites in a solid based on the peak broadening in the corresponding x-ray diffraction pattern. The x-ray diffraction pattern can be described by Bragg's law with the diffraction order n, the wavelength of the x-rays λ, the distance d_{hkl} between parallel crystallographic planes hkl, and the Bragg angle θ.

$$n\lambda = 2d_{hkl} \cdot \sin(\theta) \tag{2.13}$$

For a crystalline solid only very sharp peaks appear in the x-ray diffraction pattern. In case of crystallites with a very small particle size, the peaks in the diffraction pattern broaden. This broadening of the peaks can be related to the size of the crystallites by the Scherrer-formula [54]. The complete formula is given in Eq. 2.14 with l being the size of the crystalline particle, the dimensionless Scherrer shape factor K, the x-rays wavelength λ, the Bragg angle θ, and the full width half maximum of the diffraction peak $B(2\theta)$. The shape factor varies from 0.89 for spherical particles to 0.94 for square particles. The

application of the Scherrer formula is limited to crystallite sizes below 100 nm. The Scherrer formula provides a lower limit of the crystallite size, because the broadening of the peaks can also originate from other contributions such as mechanical strain in the material or from the instrument itself [55].

$$l = \frac{K\lambda}{\cos(\theta) \cdot B(2\theta)} \tag{2.14}$$

2.5 Galvanic metal deposition

2.5.1 Galvanostatic metal deposition

The galvanic deposition is a well-known and intensively used technique in research and industry [56]. The schematic setup for galvanic deposition with an external current supply is illustrated in Fig. 2.10. The counter electrode (CE) and the working electrode (WE) are both immersed into the same electrolyte and connected to an external current supply, such as a galvanostat. The electric circuit is closed over the electrolyte. Inside the electrolyte the conductivity is obtained by the movement of ions.

In case of a metal ion containing electrolyte, the counter electrode is typically a chemically almost inert metal, such as Pt. The WE can be of any material that allows free electrons to be in contact with the electrolyte at the interface WE / electrolyte. The reference electrode (RE) is not mandatory, but is used to monitor the electrochemical deposition conditions. The thermometer is used to monitor the electrolyte temperature, since the electrolyte temperature can have a drastic influence on the growth of the metal layer [57].

A potential difference between the two electrodes develops as soon as the electrodes are in contact with the electrolyte. Applying an electric current to the electrodes by the galvanostat changes this initial potential between the electrodes. Before metal ions from the electrolyte are reduced by free electrons at the WE / electrolyte interface, the metal ions loose their solvation shell. The hydrolyzed metal ions are transported to the WE / electrolyte interface by convection and diffusion. An additional contribution comes from the migration of ions to the electrodes due to the electric field. The reduced metal atoms form early nucleation seeds on the surface of the WE by surface diffusion. The further growth of these seeds forms the metallic layer on the WE. The additional formation of H_2 gas at the WE can occur as an undesired side reaction in case of a local depletion of metal ions in the electrolyte near to the WE. This side reaction can be reduced by a lower deposition current density or increased convection of the electrolyte.

The half reactions at the CE and WE are exemplarily sketched in Eq. 2.15–2.17 for the Ni deposition from an aqueous $NiSO_4$ electrolyte.

$$\text{reaction at WE :} \quad \mathrm{Ni^{2+} + 2e^- + 4H_2O \rightarrow Ni + 4H^+ + 4OH^-} \tag{2.15}$$

$$\text{reaction at CE :} \quad \mathrm{4OH^- \rightarrow 2H_2O + O_2 + 4e^-} \tag{2.16}$$

$$\text{side reaction at WE :} \quad \mathrm{4H^+ + 2e^- \rightarrow 2H_2} \tag{2.17}$$

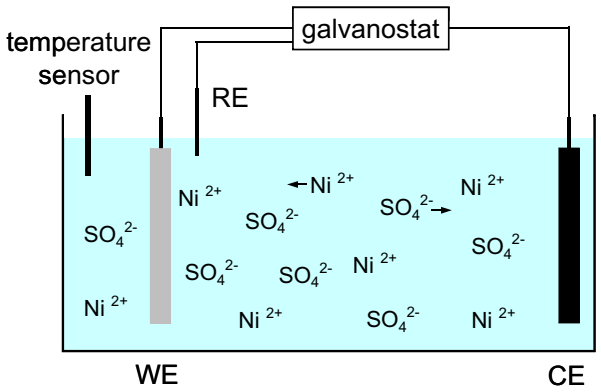

Figure 2.10: Schematic setup for galvanic deposition with external current supply exemplarily shown for Ni deposition from a $NiSO_4$ electrolyte.

2.5.2 Galvanic metal deposition in high aspect ratio pores

The galvanic metal deposition in high aspect ratio pores is well investigated for porous alumina (AAO) [58, 20, 21]. The metal deposition in porous AAO structures can be obtained in two ways. The first way is the deposition directly on a metal surface, such as a plating base predeposited by physical vapor deposition on one of the open sides of the membrane. The metal deposition starts on the metallic plating base filling up the pores to the pore opening. In principle, this method has been already described in section 2.5. The only difference is the more or less pronounced diffusion limitation inside the pores highly depending on the metal ion concentration of the electrolyte and the aspect ratio of the pores. The big advantage of e.g. AAO is that the pore walls are electrically insulating, so that a parasitic island deposition of metal at the walls of the pores is prevented. This condition is not necessarily the case for pore structures consisting of other materials, such as semiconductors.

The second way is the capacitively coupled deposition. Here, the metal deposition on the pore tip does not occur directly on the metal plating base, but through a dielectric barrier between the pore tip and the metallic or semiconducting substrate. Unlike for the direct metal deposition on a metal plating base by DC currents or voltages, it is necessary to use AC currents / voltages. In this case the charges at interfaces of the dielectric barrier are periodically reloaded. The electrons at the dielectric barrier / electrolyte interface reduce metal ions from the electrolyte and thus, the metal deposition in the pores.

2.5.3 Electrolytes

Ni electrolyte

The typical Ni electrolyte is a Watt's type based electrolyte developed by Watts [57]. It is a classical representative of the acidic aqueous metal ion electrolyte. The Ni ions originate from dissolved $NiSO_4$ and $NiCl_2$ salts. The high Ni ion concentration in the electrolyte is beneficial for the deposition inside high aspect ratio structures, because it allows for a sufficiently high concentration of Ni ions at the pore tips. The boric acid is a typical buffer agent that keeps the electrolyte in a predefined pH regime during the deposition.

This kind of electrolyte was already successfully applied for the galvanic deposition of Ni in AAO pore arrays and membranes [58].

Fe-Co electrolyte

A standard electrolyte for the binary galvanic deposition of Fe an Co contains $FeSO_4$ and $CoSO_4$. The ratio of the Fe to Co ions depends on the desired composition of the alloy to be deposited. Like for the Ni electrolyte, the electrolyte is also highly rich on metal ions to prevent a depletion of metal ions in the pore tips. In this electrolyte, the boric acid is also acting as a buffering agent. The ascorbic acid is a complexing agent that stabilizes the Fe^{2+} ions countervailing the oxidization to Fe^{3+} in an aqueous electrolyte.

Variants of this Fe-Co electrolyte have been also successfully applied in the galvanic deposition of Fe_xCo_{1-x} nanowires in AAO membranes [59, 60].

2.6 Magnetism

2.6.1 Definitions of hysteresis loop parameters

A magnetic material is typically characterized by its hysteresis loop. For recording the hysteresis loop, the material is magnetized to positive saturation first. Then the magnetic field is reversed and the sample is magnetized to negative saturation. The loop is completed by magnetizing the sample to positive saturation again. From this hysteresis loop several parameters, like remanence magnetization, coercivity etc. can be extracted. These parameters are strongly affected by e.g. the geometry and size of the magnetic structure, defects, internal stresses, etc. [61].

Remanence magnetization and remanence squareness

The remanence magnetization M_R is the persistent magnetization of a magnetic material at zero external magnetic field after being magnetized to saturation priorly.

A quantity directly associated with the remanence magnetization is the remanence squareness or remanence ratio S. The remanence squareness is a good measure to describe the magnetization state of the sample. For example, a remanence squareness of 0.5 indicates a random orientation of the easy directions in the sample [62]. Besides this, the remanence squareness and the coercive squareness are used to quantify the shape of the hysteresis loop. The remanence squareness is defined as the ratio of the remanence magnetization M_R and the saturation magnetization M_S [61].

$$S = M_R/M_S \tag{2.18}$$

Coercivity

The coercivity is a measure of the capability to maintain the magnetization against an opposing magnetic field [63]. One differentiates between the coercivity and the intrinsic coercivity. The coercivity is the magnetic field necessary to reduce the magnetic flux density B to zero after it was previously magnetized to saturation. The definition of the intrinsic coercivity is analog to the coercivity, but here the magnetization is reduced to

zero. In general, the difference between both quantities is insignificantly small, but plays a more important role for very hard permanent magnets [63]. Thus, the term coercivity will be used in the following also with respect to the magnetization. The coercivity is highly depending on the crystal size of the material [64].

Susceptibility

The susceptibility χ is the connection between the magnetization M and the magnetic field strength H. For dia- and paramagnetic materials, the susceptibility is a constant, while it is depending on the magnetic field strength for ferromagnetic materials. Therefore, the differential susceptibility is more suitable to describe the field dependency of the susceptibility of ferromagnetic materials as defined in Eq. 2.19.

$$\chi = \mathrm{d}M/\mathrm{d}H \tag{2.19}$$

Saturation field strength

The saturation field H_S is the smallest external magnetic field strength that results in complete saturation of the magnetization in the sample. Saturation is reached when the externally applied magnetic field strength equals the anisotropy field [64]. At the saturation field strength the susceptibility approaches zero. Thus, a further increase in the magnetic field strength results in no further increase of the sample magnetization.

Hysteresis losses

The hysteresis losses P_{hys} are the losses occurring when reversing the applied magnetic field from H_S to $-H_S$ and back. The hysteresis losses are frequency dependent and are proportional to the area enclosed by the hysteresis loop. The hysteresis losses under DC conditions are commonly calculated by the following formula with the volume V, the magnetic field strength, and the magnetization M.

$$\frac{P_{hys}}{V} = \int H\mathrm{d}M \tag{2.20}$$

2.6.2 Magnetic anisotropy

Magnetic anisotropy is the preferential alignment of the magnetization in the magnetic material along the magnetically easy directions [61]. In terms of magnetization, easy direction means that this direction is energetically favorable for the alignment of the magnetization. If a magnetic material is behaving magnetically isotropic and is not subjected to an external magnetic field, there is no preferential alignment of the magnetization in the material. There is a multitude of magnetic anisotropies, such as magnetocrystalline, shape, or magnetoelastic anisotropy, etc. [63]. Typically, not only a single magnetic anisotropy is present in a material, but several, e.g. magnetocrystalline anisotropy and shape anisotropy. In the case of several anisotropies present, the alignment of the magnetization depends on the anisotropy constants [63].

Magnetocrystalline anisotropy

The magnetocrystalline anisotropy arises from the spin-orbit coupling and thus from the crystal structure of the material. It is an intrinsic property of the magnetic material. Magnetizing a single-crystalline magnetic material into saturation along certain crystallographic directions results in different shapes of the magnetization curves. Certain crystallographic directions show easy magnetization, others hard magnetization, and others in between both. For Ni, the easy magnetization axis is the $\langle 111 \rangle$ and the hard axis is the $\langle 100 \rangle$, $\langle 110 \rangle$ is in between. For Fe, it is vice versa and for Co the easy axis is the $\langle 0001 \rangle$ [64].

Shape anisotropy

The shape anisotropy arises directly from the sample geometry. It is the result of the competition between the magnetization of the sample and the associated demagnetizing field. In case of spherical particles, the shape anisotropy is zero, while in the case of rods, such as magnetic nanowires with high aspect ratios, the magnetization preferentially aligns along the long nanowire axis. This alignment is the result of the smaller demagnetization field along the long rod axis and the much stronger demagnetization field along the short rod axis. If the sample is not in a single-domain state, but in a multidomain state, the magnetization of each domain causes a demagnetizing field that is interacting with the demagnetizing fields of the neighboring domains [64].

2.6.3 Magnetization reversal

The magnetization reversal is the reversal of the magnetization direction due to an opposing applied magnetic field. It can be divided in coherent and incoherent magnetization reversal. The Stoner-Wohlfarth model describes the coherent magnetization reversal for single-domain particles [65]. The magnetization vectors of all single-domain particles are oriented parallel to each other and change their orientation coherently according to the orientation of the externally applied magnetic field.

Coherent reversal is typically only possible for particles with a particle size below the coherence radius, in the other cases the magnetization reversal is incoherent. For example, it has been shown by finite-element modeling and boundary-element modeling for magnetic Ni nanowires that the magnetic reversal occurs either by transversal or vortex reversal depending on the thickness of the wires [66]. The reversal usually starts at the beginning or end of the nanowire because of the presence of high stray fields with the nucleation of domains where the magnetization is oriented in field direction. This leads to the formation of either head-to-head domain configurations (magnetization vectors face each other) or tail-to-tail configurations (magnetization vectors oppose each other) [64]. These two domains with opposing magnetization are separated either by a transverse or vortex domain wall. The domain walls propagate through the nanowire and may be hindered in motion or even pinned at crystal defects. Transverse and vortex magnetization reversal can occur also in a combined manner [66], while coherent reversal usually only occurs if the switching fields for any other incoherent reversal mode is higher than the switching [67].

2.7 Battery

2.7.1 Definitions of battery parameters

Cell voltage

The theoretical cell voltage U_{cell} can be calculated by the Nernst equation [68] already shown in section 2.2.2. It consists of the electrode potential E, the standard electrode potential E_0, the universal gas constant R, the temperature T, the mole number of exchanged electrons z, the Faraday constant F, and the activities of the oxidant a_{ox} and of the reductant a_{red}.

$$E = E_0 - \frac{RT}{zF} \ln \frac{a_{\mathrm{ox}}}{a_{\mathrm{red}}} \tag{2.21}$$

The discharging and charging of the battery involves a redox reaction that can be split in the oxidizing partial reaction of the anode and the reducing partial reaction of the cathode. Considering the stoichiometry and a negative sign for the oxidizing partial reaction, the cell potential can then be directly obtained by the sum of these partial reactions. In application, the cell voltage should be as high as possible for a high energy density of the battery.

Coulomb capacity

The coulomb capacity of the battery is defined as the amount of charges Q stored in the active material (either cathode or anode) [68]. The maximum amount of charges stored is only limited by the amount of the active material. The coulomb capacity of a battery should not be confused with the electric capacity. In application, the gravimetric capacity is one of the decisive quantities for batteries. The gravimetric capacity is defined as the ratio of the capacity per weight. It also allows for an easy comparison between different anode or cathode materials, respectively. In application the gravimetric capacity shall be as high as possible for a high energy density of the battery.

Energy output

The maximum energy output of a battery is defined as the product of the cell voltage U_{cell} and the coulomb capacity Q [68]. Like the coulomb capacity it is mostly expressed as gravimetric energy density.

Charging rate

The charging rate of a battery is typically expressed as a function of the capacity C of the battery and the charging time t in hours [69]. This nomenclature implies that the charging of the battery is carried out under galvanostatic conditions. In application it is highly desired to achieve high charging rates and thus, low charging times without capacity losses or lifetime reduction of the battery, e.g. due to the degeneration of the electrolyte or the anode material. In practice, the charging rate cannot be increased arbitrarily because transport processes inside the battery, such as the diffusion of Li ions from the electrolyte through the solid–electrolyte interface layer into the anode or cathode respectively, are rate limiting steps [69].

Solid–electrolyte interface

The solid–electrolyte interface (SEI) layer is a passivating layer that forms at the interface between the surface of the anode and the electrolyte. It builds up in the first lithiation and delithiation cycles and consists of several organic and inorganic species from the decomposition of the battery electrolyte, including Li ions. After the anode is effectively passivated from the reactive electrolyte species by the SEI, the decomposition of the electrolyte is stopped [70]. The SEI is nonconductive to electrons, but ion conductive, so that it allows for the in-diffusion of Li ions through the layer into the anode on lithiation and the out-diffusion on delithiation. A key requirement for the SEI layer is therefore the thickness of the SEI. It must be thin enough to allow for a high diffusion current of Li ions and thick enough to allow for an efficient passivation. The thickness of the SEI strongly depends on the electrolyte constituents and their concentration. A $LiPF_6$–based electrolyte proved to form an efficient and protective SEI layer around anodes that quickly rebuilds [70] if it is damaged, e.g. due to the volume expansion and subsequent shrinkage during cycling.

2.7.2 Capacity losses at the anode

Anode fading

The fading is the gradual decrease in the coulomb capacity of the battery including not only irreversible, but also reversible losses. It is commonly calculated as the difference in coulomb capacity between one cycle and the previous cycle of the fully lithiated anode. The fading in Li-ion batteries has a multitude of different origins, such as phase changes in the active material, degradation of the current collector or the electrolyte, overcharge phenomena, etc. [71].

Capacity fading due to phase changes on lithiation and delithiation is primarily an issue of non-intercalation anodes. In this type of anodes, the alloying and dealloying due to the lithiation and delithiation of the anode result in phase changes in the anode itself. These phase changes can induce mechanical stresses. As a result microcracks can form. These microcracks can lead to the partial delamination of the anode material and thus, to capacity fading [71, 72].

The degradation of the current collector can be either related to corrosion of the current collector, the formation of passive films on the current collector resulting in an increased ohmic resistance, or adhesion problems between the active material and the current collector leading to a delamination [71].

Another frequent contribution to fading are chemical side reactions during the battery cycling, such as reactions between Li ions and decomposed electrolyte species forming insoluble compounds, such as LiF etc., depleting Li ions from the electrolyte.

Overcharge phenomena can lead to a deposition of excess Li on the anode surface at spots where the electrode potential is more negative. The deposited Li reacts immediately with reactive species from the electrolyte and forms a layer of insoluble compounds.[71].

Irreversible losses at the anode

The irreversible losses describe the losses occurring in one cycle. They are commonly calculated as the difference in the coulomb capacities between the fully lithiated anode

and the coulomb capacity taken out of the anode during full delithiation. The main contribution to these losses is the formation of the SEI on the anode by the decomposition of the electrolyte [73]. A rebuilding of a damaged SEI layer is another contribution to irreversible losses [72], as well as the irreversible lithiation of the current collector [74].

Coulombic efficiency

The coulombic efficiency describes charging losses during the charge and discharge of the battery due to side reactions, such as the chemical decomposition of the electrolyte *et cetera* [69]. These losses do not include ohmic losses due, e.g. internal resistances of anode material. For high performance batteries, the aim is to obtain a coulombic efficiency close to unity. The coulombic efficiency η is defined as the ratio of the amount of charges $Q_{discharge}$ that leave the anode during the discharge and the amount of charges Q_{charge} that is stored in the anode during charging. The losses due to internal resistances are 1-η.

$$\eta = \frac{Q_{discharge}}{Q_{charge}} \tag{2.22}$$

2.8 Instrumentation

2.8.1 Vibrating Sample Magnetometry

Vibrating sample magnetometry (VSM) is a commonly used technique to investigate the magnetic properties of materials by measuring the magnetic moments. The basic principle of a VSM is the voltage induction due to a moving magnetic material in a static magnetic field according to Faraday's law [75].

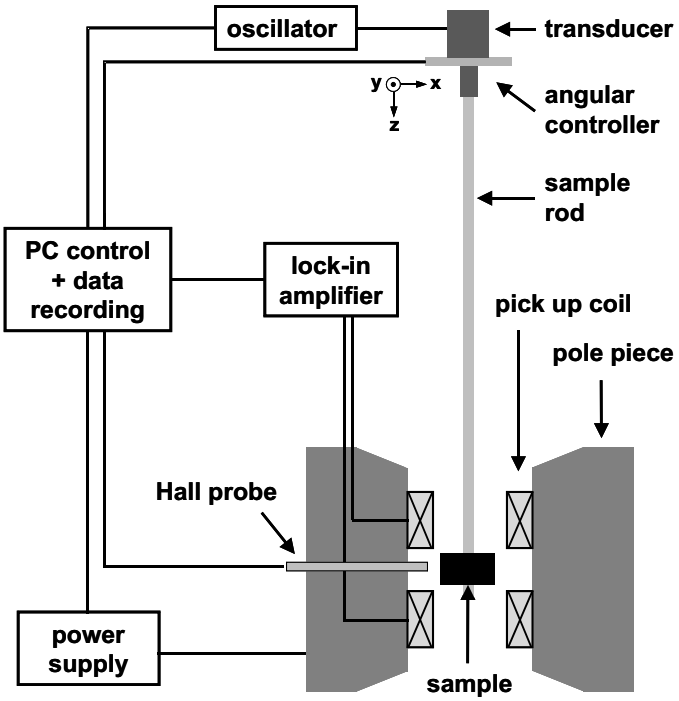

Figure 2.11: Schematic setup of a vibrating sample magnetometer.

The typical schematic setup of a VSM is presented in Fig. 2.11. The magnetic field that is applied to the sample is measured by a standard Hall probe. The magnetic sample itself is fixed to the sample holder rod. The rod is connected to a transducer that applies a sinusoidal vibration signal with a typical frequency of 60 Hz and a typical amplitude of 1 mm from an oscillator to the rod and thus, to the sample. This oscillation of the sample results in an oscillating magnetic field inducing a voltage in the pick up coils. By a lock-in amplifier this voltage signal is amplified and the signal to noise ratio is increased. The connected PC is used to control the entire measurement setup and to record the measured magnetic moments.

If the volume of the magnetic material is precisely known, one can easily calculate the sample magnetization according to Eq. 2.23 with the magnetization M, the sum of the magnetic moments, and the volume V.

$$M = \frac{m}{V} \tag{2.23}$$

2.8.2 Cyclic voltammetry

Cyclic voltammetry is a commonly used technique in electrochemistry to investigate the electrochemical processes at electrodes immersed in an electrolyte. The basic principle is that a potential is applied to the electrode and linearly swept between two fixed potentials. The corresponding current response of the system is measured. For these two fixed potentials it is not necessary to position one in the anodic and the other in the cathodic regime. It is also possible to position both either in the anodic or in the cathodic regime. Classically, the sweep from the negative to the positive potential is called the anodic sweep and from the positive to the negative potential the cathodic sweep [76]. The sweep rate is constant and lies in the typical range from 0.1 mV/s to 5 mV/s for quasi-steady state conditions depending on the electrochemical system [76].

The current response of the system can result in peaks in the measured current density *vs.* voltage diagram, which originate either in electrochemical reactions (oxidization or reduction), the formation of new compounds, or in adsorption / desorption processes. Another important contribution to the measured current is due to the capacitive effects, such as double layer charging. If the sweep rate is very small, these capacitive current contributions can be almost neglected [76].

This technique is well suited to qualitatively analyze the resulting reactions of an electrochemical system at certain applied potentials.

Chapter 3

Experimental

3.1 Samples

The InP samples used in this work originate from a single-crystalline ingot grown by Crystacomm Inc according to our specifications. The ingot is sulfur doped with a carrier concentration of $1.1 - 1.5 \times 10^{17}\,\mathrm{cm}^{-3}$. The resistivity is about $0.014 - 0.019\ \Omega$ cm and the electron mobility of around $3000\,\mathrm{cm}^2/\mathrm{Vs}$. The wafers have a diameter of 50.6 mm (2" wafer) and are $(100) \pm 0.1°$ oriented. The front and back side of the wafers are polished and epitaxy-ready.

Three different wafer thicknesses are used, 300 µm, 400 µm, and 500 µm, each ± 10 µm. The samples were cut in 6×6 mm^2 by a diamond cutter. The active etching area is circular and encloses an area of 25 mm^2.

3.2 Electrolytes

3.2.1 Pore etching and membrane formation

The electrolyte used for the electrochemical pore etching and membrane formation is an aqueous 6 wt% HCl electrolyte. The electrolyte temperature is maintained constantly at 20 °C. These conditions have proven to be optimal in previous works [42, 77, 78].

3.2.2 Post-etching

Post-etching is the essential step to obtain quasi-intrinsic InP by overlapping space charge regions (SCR) in the pore walls. The electrolyte is optimized for InP to show an isotropic etching behavior over the entire pore length with a very low dissolution rate. It is further optimized to show a self-limiting etching behavior at the SCR surrounding each pore [77]. The electrolyte is tested to be stable under various electrochemical conditions – from open circuit to cathodic potentials of up to -2 V.

The used post-etching electrolyte is a combination of mineral and organic acids and alcohol. It consists of HF (48 %), HNO_3 (65 %), acetic acid (96 %), and ethyl alcohol (99 %) in a mixing ratio of 3 : 8 : 24 : 15. The electrolyte composition is not trivial and follows the general idea of HF working as etchant, HNO_3 as oxidant, and acetic acid and ethyl alcohol as surfactants. The ethyl alcohol is thought to have also a passivating influence.

The solution is mixed in the following sequence to avoid uncontrolled chemical reaction between single constituents. At first, the ethyl alcohol and the acetic acid are mixed, followed by HNO_3 acid and finally HF. In the presence of HNO_3, ethyl alcohol and acetic react to ethyl acetate and water. This reaction results in a strong heating of the electrolyte. For the post-etching the electrolyte temperature is maintained constantly at 20 °C.

3.2.3 Galvanic deposition

Ni deposition

The used electrolyte is a typical Watt's type Ni electrolyte adjusted to *p*H-value of 3 with H_2SO_4. The electrolyte is a very metal ion rich electrolyte to prevent metal ion deficiency in the depth of the pores. The electrolyte consists of 300 g/l $NiSO_4$, 45 g/l $NiCl_2$, and 45 g/l H_3BO_3. Deionized water is used as solvent. The H_3BO_3 serves as buffering agent. The electrolyte temperature is maintained constantly at 20 °C or 35 °C depending on the experiment.

FeCo deposition

The used electrolyte is a simple buffered FeCo electrolyte. As the Ni electrolyte described before, this electrolyte is also very metal ion rich for the same reason. The electrolyte consists of 180 g/l $FeSO_4$, 60 g/l $CoSO_4$, 30 g/l H_3BO_3, and 4 g/l ascorbic acid. H_3BO_3 acts as buffering agent, while the ascorbic acid stabilizes Fe^{2+} ion against oxidation to Fe^{3+}. The electrolyte temperature is maintained constantly at 30 °C.

3.3 Electrochemical cells

3.3.1 Etching cell

The porous structures are etched in an electrochemical double cell. The double cell consists of two parts, a big bottom cell and a much smaller top cell. The double cell consists of Teflon. Teflon is stable against HF and organic solvents such as esters preventing a chemical interaction between the etching electrolyte and electrochemical cell. Each half cell has an orifice through which the InP sample is exposed to the electrolyte of each half cell. To prevent leakages at these orifices fluorinated O-rings are used. Fluorinated O-rings are necessary because of their extremely high chemical stability, since highly corrosive chemicals are used as etching electrolyte. The InP sample is mounted on the O-rings in between the two half cells and pressed together. The both half cells are mounted on an optical bench system and fixed by screws preventing an uncontrolled opening of the half cells during the etching process.

The bottom half cell is completely sealed from light. It has two opposing electrolyte inlets in the sample near region and two opposing outlets below the inlets. This design guarantees an optimal homogeneous electrolyte flow near the sample surface. The top half cell has an inlet on one side and an outlet on the opposing side through which the electrolyte is flowing. For an additional back side illumination a sapphire glass is inserted into the top part of the top half cell sealed by a fluorinated O-ring. This double cell is based on the double cell presented in [79], but further optimized based on personal

experience to withstand the harsher chemical conditions of post-etching, the necessity for high power back side illumination, electrolyte flow in parallelized systems, and highly reduced maintenance effort.

For the successful fabrication of post-etched InP membranes, it is necessary to maintain a perfect alignment of the porous InP sample in the double cell for all process steps. Thus, the porous InP sample is never taken out completely of the double cell between each process step. This procedure also minimizes the chance of wafer breakage.

The bottom cell contains two electrodes, the counter electrode (CE) and the reference electrode (RE). Both electrodes are made out of a Pt wire. The CE is far away from the sample surface and has a big area compared to the sample surface. This is necessary for obtaining an homogeneous electrical field on the sample surface during the electrochemical etching. The CE is connected to a banana jack for external connection through a tiny hole in the Teflon wall of the bottom half cell. This hole is sealed against leakage by a combination of neoprene and Teflon band. The same sealing concept is applied for all other electrodes that are permanently integrated in the double cell.

Since the voltage at the InP surface (effective WE) / electrolyte interface is the decisive quantity for the electrochemical reaction on the InP surface, this voltage is measured by two reference electrodes, the reference electrode and the sense electrode (SE). This allows to compensate for the voltage losses in the electrolyte, cables, and contacts. The RE is a pseudo-reference electrode. It is positioned in the nearest proximity of the sample surface without touching the sample surface. It is externally contacted in the same way as the CE. In contrast to a standard RE, such as a standard hydrogen electrode or Ag/AgCl electrode, it is possible to measure AC voltage signals with a Pt electrode, which allows to perform *in-situ* impedance spectroscopy.

The SE is an additional pseudo-reference electrode that allows to decouple the voltage measurement from the current measurement in a four electrode configuration. When the two half cells are pressed together with the InP sample in between, the Al stripe is in direct contact to the sample surface, so that the potential at the sample surface is measured by the SE. The SE consists of commercially available Al foil that is folded in two layers. Then the Al stripe is fixed on the top part of the bottom cell with scotch tape. Close to the O-ring the Al foil is cut, so that the sample can be exposed to the electrolyte. It is very important that the Al is not coming in contact with the electrolyte, because it will start to corrode, so that it cannot be used as sense electrode afterwards. To save the Al stripe from corrosion outside the double cell it is protected with scotch tape from top and bottom leaving some space for the electrical contacting by a crocodile clip.

The top cell contains only one electrode, the working electrode (WE). This electrode is also made out of Pt. It also has a big area compared to the sample surface due to the same reason as for the CE. The back side of the InP sample is contacted to the WE by an electrolyte contact providing an easy and reproducibly good contact compared to an unhandy solid-state contact.

The electrical connection of the double cell for the formation of the curro-pore array is a typical four electrode arrangement with four electrodes positioned at four different positions in the double cell, as described above in detail and depicted in Fig. 3.1 a).

Figure 3.1 b) shows the electrode arrangement for the membrane fabrication. Since the membrane formation has to be performed in the same double cell as the formation of the curro-pore array, the possible electrode positions are limited. It is essential for the success of the membrane formation that the electrodes in the bottom cell are not

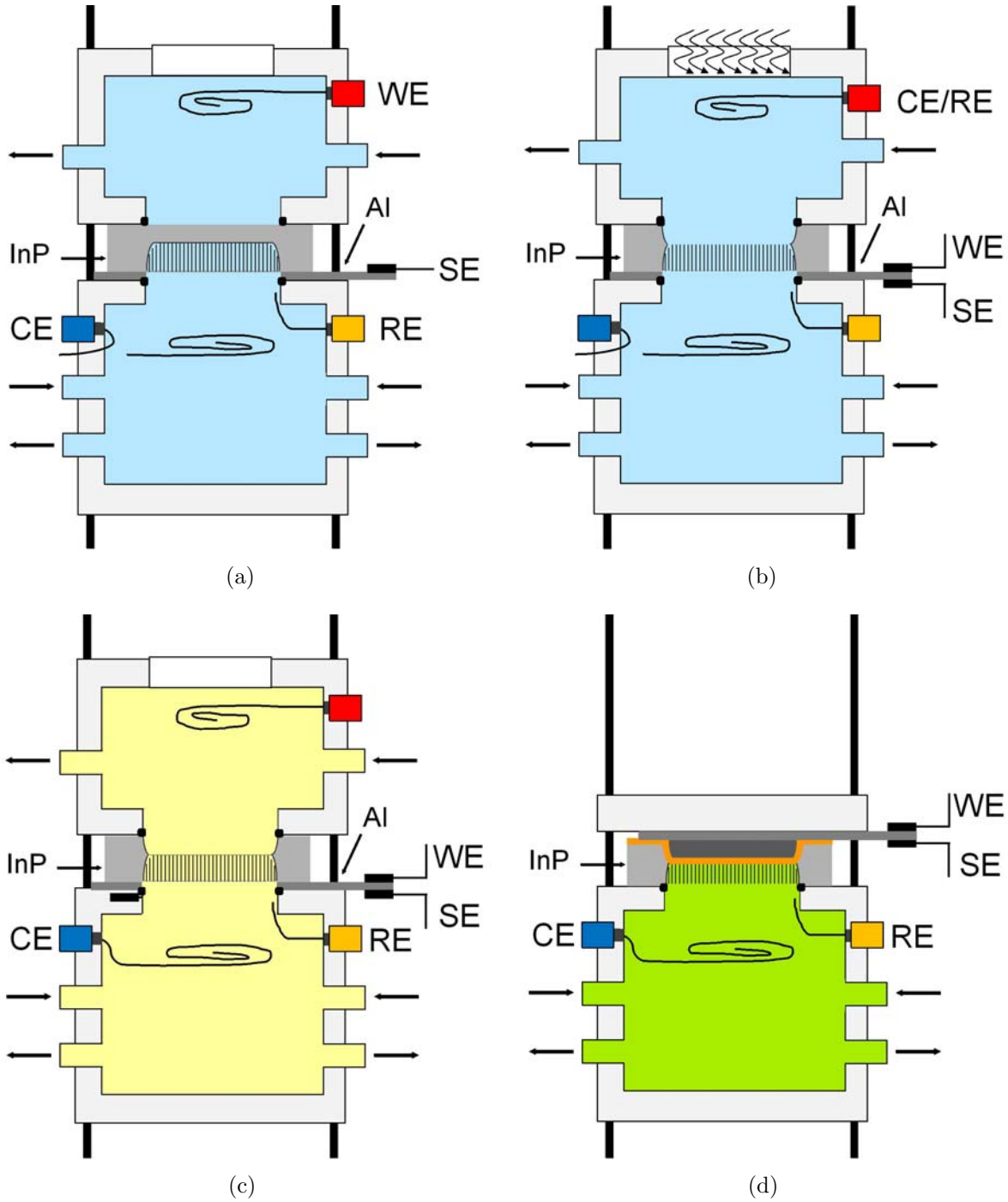

Figure 3.1: Schematic cell setup in cross section and electrical connection for a) pore etching in InP, b) membrane formation, c) post-etching of porous InP pore arrays / membranes, and d) galvanic metal deposition.

used for the membrane formation, because this would result in the complete dissolution of the previously etched curro-pore array. Therefore, the electrode arrangement for the membrane formation is completely different compared to the formation of the curro-pore array. It is basically a two electrode arrangement with compensation of voltage losses in the contacts and cables. The WE is contacted to the Al stripe as well as the SE that

is clipped at a different position on the Al stripe. The Pt electrode in the top cell is connected to the CE and the RE simultaneously. This means, a finite current flows also through the RE. The electric contact area of the InP sample to the Al electrode is big and ohmic enough, so that it is not necessary to have a separate SE in contact with the sample. Nevertheless, the loss in the Al stripe / InP contact is not compensated.

The quality of the FFT impedance spectroscopy could be improved by introducing a second electrode as RE in the top cell. But this would result in a partial shading of the sample surface during the illumination with blue light, since this electrode needs to be positioned in the very proximity to the sample surface. The impedance spectroscopy is primarily used as a qualitative characterization tool for the membrane fabrication process, and not to investigate the pore growth in complete detail. Therefore, it was renounced to integrate an additional reference electrode into the top cell.

The post-etching was performed for InP pore arrays and membranes, but the cathodic post-etching procedure was optimized only for InP membranes. Thus, the following description focuses only on the cathodic post-etching of InP membranes. The electrode arrangement for the post-etching is a combination of the two previous arrangements. The WE and SE are connected to the Al stripe, while the CE and RE have the same positions in the bottom cell as already described for the curro-pore array formation. This electrode arrangement is basically a three electrode arrangement and does not allow for a decoupling of the voltage measurement and the current measurement, but nevertheless voltage losses in the electrolyte, contacts, and cables can be compensated.

The electrochemical double cell is stacked in a holder with a tilting of about 45° during the etching experiments. This ensures that evolving small gas bubbles on the sample surface are instantaneously removed from the surface by the constant flow of the electrolyte and transported out of the half cells through the top outlets. This removal of gas bubbles is highly important for the success of the etching experiments, because an agglomeration of gas bubbles results in an interruption of the electrical contact between the sample surface and the electrolyte and thus, in an electric break-down or at least in an inhomogeneous etching result of the sample.

3.3.2 Galvanic deposition cell

Instead of using a double cell setup, a single half cell is used for the galvanic deposition. The half cell is identical to the bottom half cell used for the etching experiments. The CE and RE are made out of Pt and are located at the same positions in the bottom cell.

In case of the galvanic metal deposition into pore arrays the InP sample is the WE. It is glued to a two-layer Al stripe with conductive silver for leveling out the surface roughness and to provide a good electrical contact. The Al stripe itself is contacted by a crocodile clip. In the case of the InP membrane the metal layer deposited on the back side of the membrane serves as working electrode. It is electrically contacted to a Pt stripe by InGa to level out any height differences and to provide a good electrical contact to the Pt sheet. The Pt sheet itself is contacted with a crocodile clip. The Pt stripe is pressed on the sample with a Teflon cover plate fixed by screws. This establishes the electric contact to the WE.

The galvanic deposition setup is a three electrode setup, since the SE is also connected to the Pt stripe, resp. Al stripe as the WE, as shown in Fig. 3.1 d). Thus, this electrode arrangement does not allow a complete decoupling of voltage measurement and current

measurement, but nevertheless voltage losses in the electrolyte, contacts, and cables can be compensated.

3.4 Etching setup

3.4.1 Pore etching and membrane formation

The schematic setup for the electrochemical pore etching is shown in Fig. 3.2. The setup consists of five basic elements, namely the PC control unit, the potentiostat, the thermostat, the peristaltic pump, and the electrochemical double cell which has been described in section 3.3.

The PC control unit is a standard PC equipped with a PCI DAS 1602/16 measuring board from PLUG-IN to control the potentiostat and the JULABO F25 thermostat by the *SiPor* software. The potentiostat is an ELYPOR-02 combined potentiostat and galvanostat from ET&TE GmbH with an integrated FFT-impedance spectrometer that allows to apply 30 frequencies in the range from 3 Hz up to 20 kHz. The controlled voltage range of the potentiostat is from −20 V to +70 V with a maximum current up to 200 mA. A potentiostat is a controlled voltage source with an integrated voltmeter and amperemeter, while a galvanostat is a controlled current source with an integrated voltmeter and amperemeter.

A voltage is applied between CE and WE by the potentiostat and the corresponding voltage between RE and SE is measured. This voltage is compared to the demanded voltage between RE and SE and the voltage between CE and WE adjusted accordingly, so that the measured voltage between RE and SE is in agreement with the demanded voltage between RE and SE. This feedback loop assures that the demanded voltage between RE and SE is maintained constantly, even under changing loads. In the case of a galvanostat, the feedback loop works in the same way, but a predefined current is applied instead of a voltage.

For the FFT-impedance spectroscopy an AC voltage signal generated by the sound card integrated in the PC control unit is superimposed with the DC voltage signal of the potentiostat being applied in the electrochemical experiment. In case of a galvanostatic experiment an AC current signal from the sound card is superimposed with the DC current signal from the potentiostat. The potentiostat has to be very broadband, since a broad frequency spectrum is applied simultaneously to the electrochemical system. In addition, the AC current response of the electrochemical system, resp. the AC voltage response in the case of a galvanostatic experiment is measured phase correctly. Additionally, a Pt 100-temperature to voltage integrator is integrated into the ELYPOR-02.

The four cell electrodes – WE, SE, RE, and CE – of the double cell are connected to the potentiostat by standard copper wires. The two electrolyte containers are made out of Teflon for the same reasons as the electrochemical double cell. They are double walled and actively temperature regulated by the thermostat. The electrolyte temperature is measured by a Pt-100 thermometer. In each container 300 ml of electrolyte are stored. The electrolyte is pumped into each half cell in a separate loop to prevent an electrical short-circuiting of the double cell via the electrolyte. As pump an ISMATEC IP 65 MCP Process peristaltic pump is used operated at a pumping speed of 50 rpm. TYGON LFL tubes with an inner diameter of 4.8 mm are used to connect the electrolyte containers and

the double cell. For the membrane formation an ENFIS Uno Tag LED array is mounted on top of the top half cell operated at a constant current of 200 mA with a radiant flux density of roughly 300 mW/cm^2. The typical wavelength of the emitted light is about 470 nm and lies in the blue range of the visible spectrum.

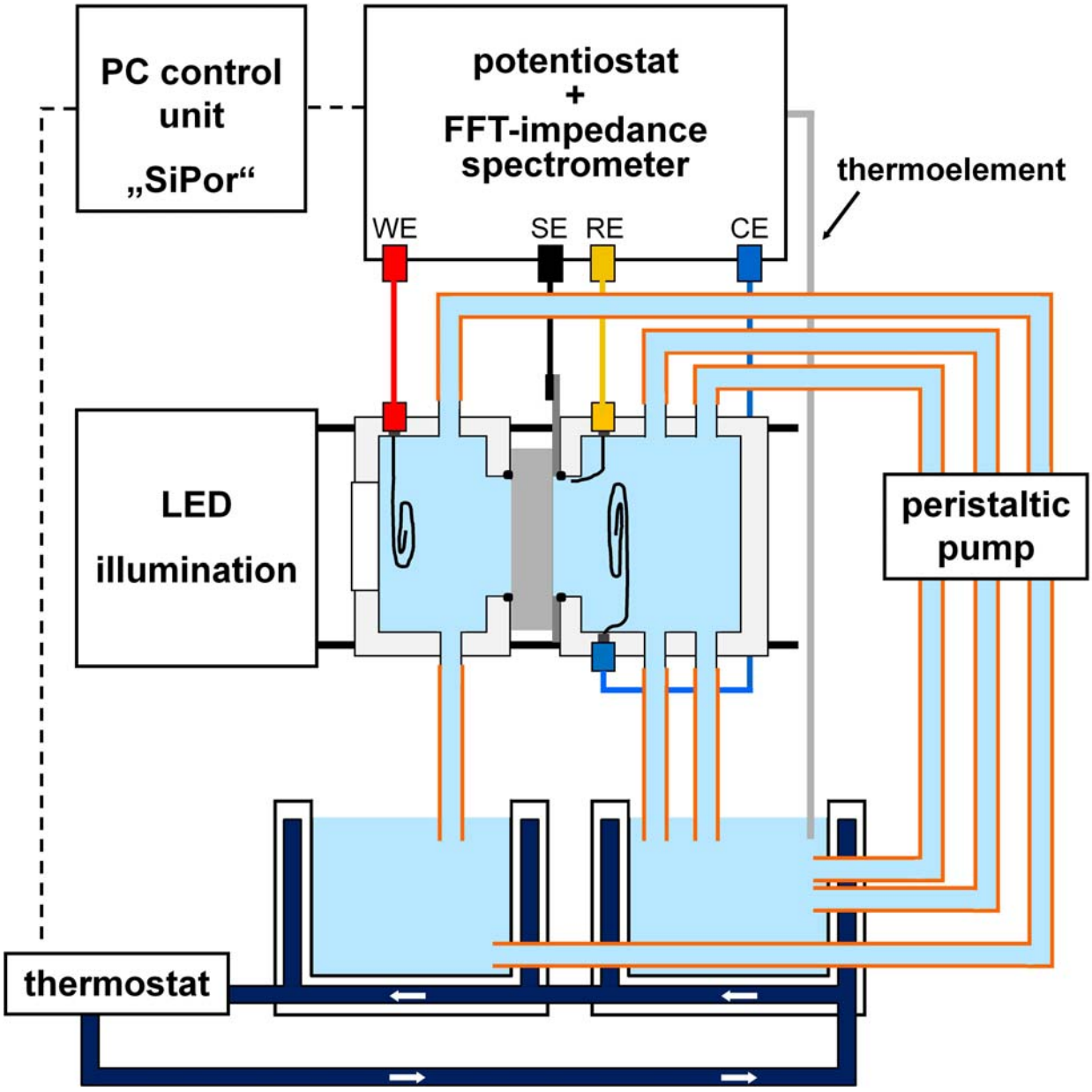

Figure 3.2: Schematic setup for electrochemical pore etching and membrane formation. The *SiPor* software on the PC control unit controls the potentiostat and the temperature of the etching electrolyte via the thermostat. The potentiostat is electrically connected to the four electrodes of the two half cells. For the membrane formation an additional high power LED array can be positioned on top of the top half cell. The two half cells are fed from different electrolyte containers in separate loops by a peristaltic pump.

3.4.2 Post-etching

For the post etching experiments the previously shown setup is slightly modified as presented in Fig. 3.3. Instead of feeding the double cell from separate electrolyte containers, one big electrolyte container is used. This container allows to feed several double cells with electrolyte simultaneously. In contrast to the previous setup, TYGON SE 200 tubes

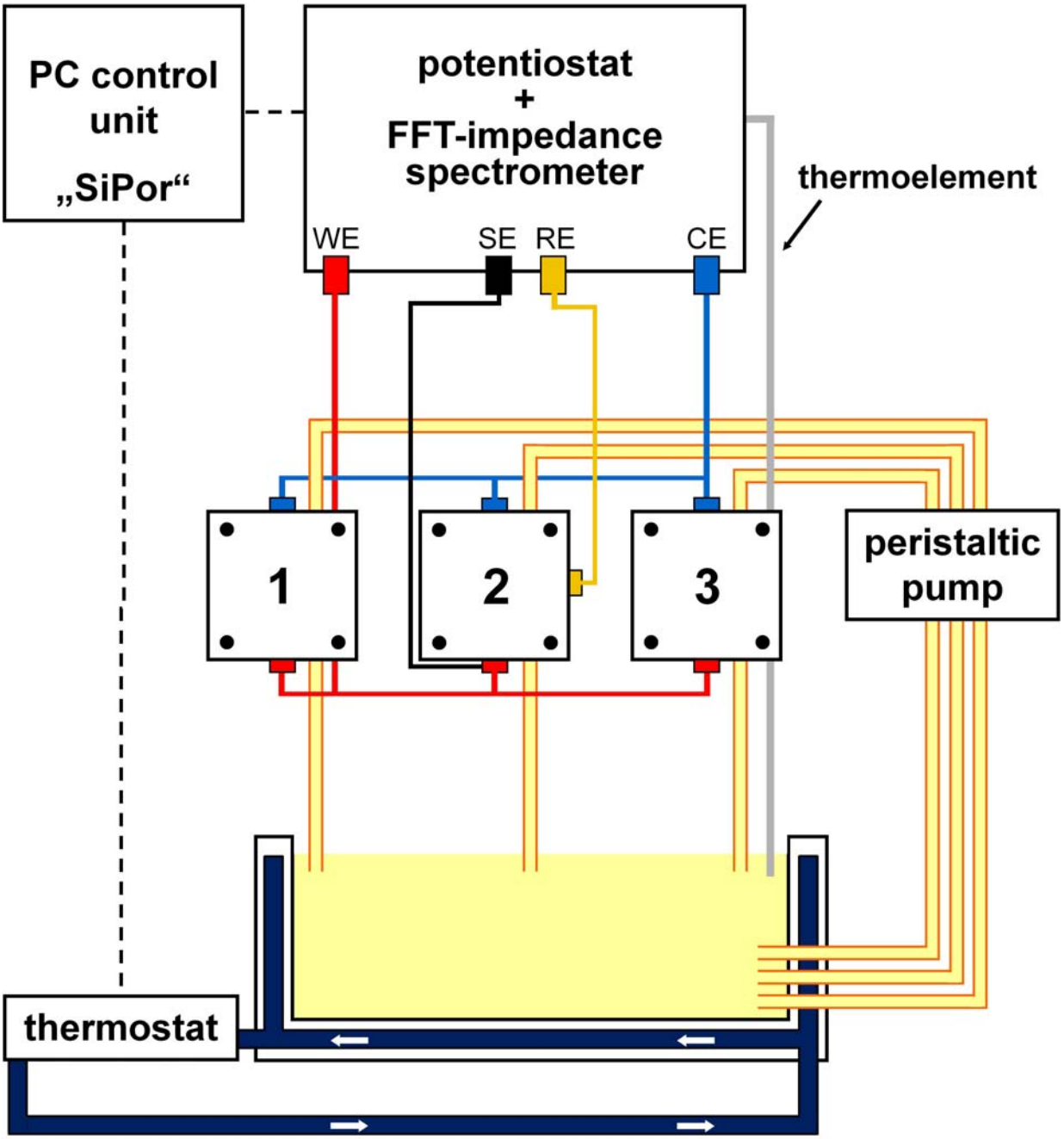

Figure 3.3: Schematic post-etching setup for post-etching of three InP membranes under cathodic bias. The setup is very similar to 3.2, but uses a single big electrolyte container and allows post-etching of multiple cells in parallel columns. In each column up to three cells can be integrated. The electrolyte is flowing in series through each column. The electrical connection of all cells is in parallel.

are used, because the post-etching electrolyte consists of HF and ethyl acetate, which is a powerful organic solvent. The SE 200 tubes have an additional inner fluoropolymer tube that is chemically inert to organic solvents and strong acids and bases. The pump is operated at a pumping speed of 100 rpm. The post-etching can be performed for a single cell or in parallel for multiple cells. Figure 3.3 shows the schematic arrangement of three

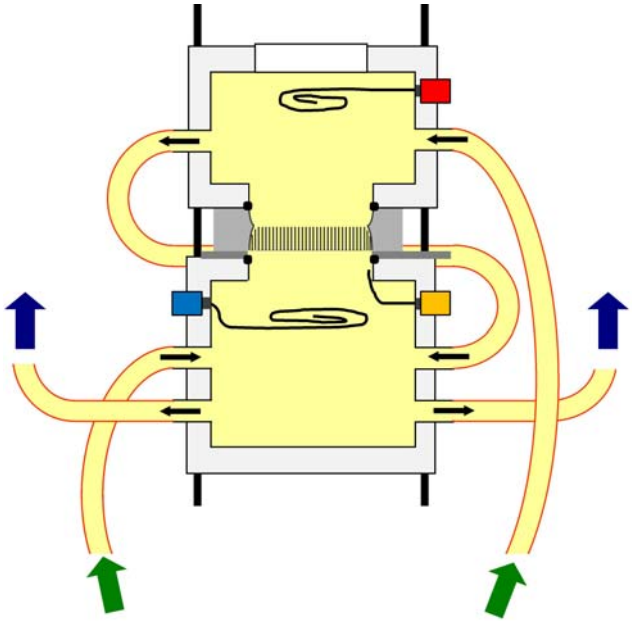

(a)

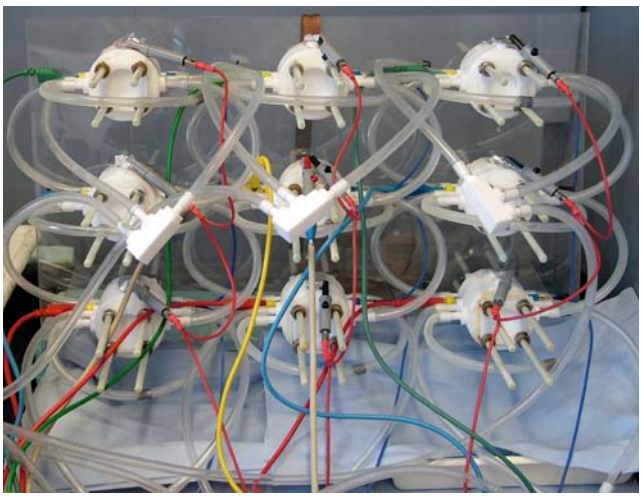

(b)

Figure 3.4: a) Schematic arrangement for in series tube connection of double cells for simultaneous post-etching. The green arrows indicate the electrolyte flow into the cell coming either from the electrolyte container or the previous cell. The blue arrows indicate the flow out of the cell going either into the electrolyte container or into the inlet of the next cell. b) Setup for simultaneous post-etching under cathodic bias of multiple cells. The colored extra cables are used to measure the voltage between RE and WE in each cell to check for errors during the post-etching process.

double cell columns that are electrically connected in parallel to the potentiostat. The SE and RE are only connected to column 2. The three columns are fed with the post-etching electrolyte from the electrolyte container in a parallel arrangement. The amount of post-etching electrolyte strongly depends on the total number of cells and the tube length. In the case of a single cell, typically 400 ml are needed, for three cells 600 ml, and for nine cells 800 ml.

Figure 3.4 a) shows the typical tubing of a single double cell for post-etching. In the case of one double cell per column the electrolyte is pumped into the cell directly from the electrolyte container, as indicated by the green arrows, simultaneously pumped through the top and bottom half cell, and then back into the electrolyte container as indicated by the blue arrows.

It is also possible to integrate multiple double cells into a single column. Up to three cells per column have been tested experimentally. In this case the electrolyte flows through the entire cell column before it is pumped back into the electrolyte container. The connection of multiple double cells in series is done as follows. The first cell in the column is fed from the electrolyte container directly, while the following cells in the column are fed from the previous cell in the column. The electrolyte outlets of the first cell – see the blue arrows – are connected to the inlets of the next cell – see the green arrows – in the same column. This procedure is continued for the following cells in the column. The last cell in the column is than connected to the electrolyte container.

In case of multiple cells per column, the individual cells in each column are electrically connected in parallel. Each of the three columns is also electrically connected in parallel, so that all cells are electrically connected in parallel to the potentiostat. All cells are stacked into a sample holder under an angle of 45° to ensure that possibly evolving gas bubbles are efficiently transported out of the cell and do not stick to the sample surface.

Figure 3.4 b) presents a picture of an early state of the setup of the simultaneous post-etching of multiple cells. In this state all cells are equipped with an external connection cable for the RE (colored cables attached to the yellow banana jack). This allows to externally measure the potential between each RE and SE/WE in each cell, so that possible failures can be easily detected – such as mechanical breaking of the sample, or the corrosion of the Al stripe as WE, *et cetera*.

In case of the parallel post-etching of nine samples a sample failure results in the loss of nine samples. Thus, in terms of time efficiency and reliability it is preferred to post-etch only one cell per column. Figure 3.4 b) presents an earlier state of the setup, the tubing of the cells. Thus, the tubing is not completely identical to the schematic tubing shown in Fig. 3.4. The main advantages of the schematic tubing shown in Fig. 3.4 a) are the optimized electrolyte flow almost preventing the formation of air bubbles and shorter tube lengths that highly reduce temperature losses of the electrolyte.

3.4.3 Galvanic Ni deposition

The schematic setup for the galvanic metal deposition is presented in Fig. 3.5. The basic setup is identical to the electrochemical etching setup and already known from the electrochemical pore etching shown in Fig. 3.2.

Since the metal deposition inside the InP pore array / InP membrane does not require a double cell, only one temperature controlled electrolyte container is needed. The typical amount of electrolyte is 200 ml. As already known from all other setups, the cell is stacked

into a cell holder under an angle of 45°.

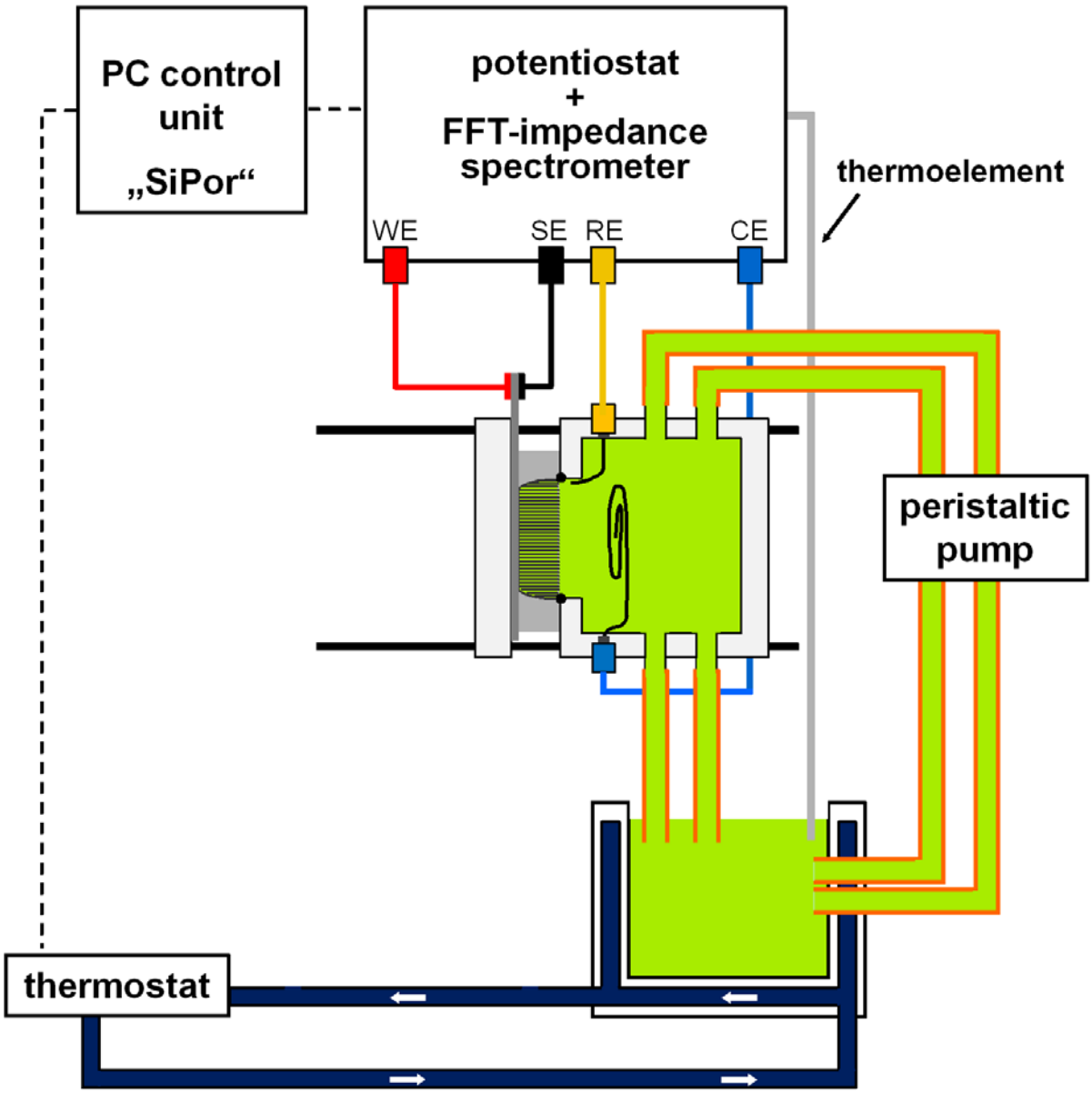

Figure 3.5: Schematic setup for galvanic metal deposition in InP pore arrays and membranes. The setup is very similar to Fig. 3.2, but uses only one electrolyte container. Instead of a double cell, a half is sufficient for the galvanic deposition.

3.5 Electrochemical parameters

Typically, electrochemical experiments are either performed at a constant voltage – also referred to as potentiostatically – or at a constant current – also referred to as galvanostatically. Besides these two basic modes, the voltage can be varied with time – also referred to as potentiodynamically – or in the case of a varying current with time – galvanodynamically. In this section the final electrochemical parameters of the single experiments are described omitting the parameters of the numerous intermediate experiments necessary

for the optimization of each process. The ideas and reasons for the parameter choices are discussed later in Chapter 5.

3.5.1 Curro-pore formation

The formation of curro-pores always follows the same scheme. A short, but high voltage pulse is applied to the sample for 1 s to obtain a homogeneous nucleation of the curro-pores. The etching potentials are optimized to the charge carrier concentration of the InP wafers, but follow the procedure given in [42, 78].

Depending on the charge carrier concentration of the used InP wafer the voltage pulse is in the range between 12 V and 17 V. The voltage pulse is followed by a constant voltage in the range between 7 V and 12 V depending on the charge carrier concentration. A slightly higher carrier concentration requires typically lower etching potentials to achieve an optimal curro-pore growth. The length of the curro-pores is controlled by the etching time in which the constant voltage is applied. The etching time scales exponentially with the curro-pore length.

3.5.2 Membrane formation

The electrochemical parameters for the membrane formation always follow the same scheme. Before the membrane formation is started the thin InP oxide layer on the back side of the sample has to be removed. This is done by a purely photochemical etching in the same double cell and in the same HCl-based electrolyte for 30 min.

The first part is etching a crysto-porous layer in the bulk InP back side until the tips of the underlying curro-pores are reached. The second step is to dissolve this layer photochemically till the underlying curro-pore array is completely opened. The crysto-porous layer is grown by applying a DC current density of typically 14 mA/cm^2 to the back side of the sample under galvanostatic conditions and illuminate simultaneously with blue light for 80 min. The simultaneous illumination already dissolves the surface of the crysto-pore layer. The blue illumination of the being etched InP back side is necessary for selective etching of the crysto-porous layer.

In the second part a DC current density of 0 mA/cm^2 is applied for typically 30 min under continued blue illumination to photochemically dissolve the remaining highly crysto-porous layer and to obtain a homogeneous and flat membrane back side surface. This etching condition is almost identical compared to switching to open circuit conditions. But as a benefit, it is possible to measure the FFT-impedance signals by applying a small perturbation to the current and measure the associated linear response in the voltage signal. During the entire membrane formation process FFT-impedance spectroscopy is performed. Every two seconds a spectrum of 16 frequencies from 75 Hz to 2750 Hz is recorded.

The third step is an optional step to structure the front surface of the membrane. The front surface comprises the nucleation of the curro-pore array. It can be removed by applying a DC current density of 4 mA/cm^2 to the front side of the membrane under galvanostatic conditions and illuminate simultaneously with blue light for 10 min. Afterwards a DC current density of 0 mA/cm^2 is applied for 20 min to obtain a flattened surface.

3.5.3 Post-etching under cathodic bias

The post-etching is performed under various conditions for InP pore arrays and membranes from open circuit conditions to a cathodic bias up to −1.5 V and for various post-etching times ranging from 1020 min to 2880 min.

3.5.4 Galvanic deposition

In all experiments the galvanic deposition is executed in a current-controlled mode, either galvanodynamic or galvanostatic and the resulting voltage is recorded if not stated otherwise.

Ni deposition

In case of the InP pore array, a current density of –20 mA/cm^2 is applied galvanodynamically in pulses of 0.8 s with a recovery time of 4.6 s in which a current density of 0 mA/cm^2 is applied. These pulses are constantly repeated for 60 min.

In case of the uncoated InP membrane, a current density of –20 mA/cm^2 is applied galvanodynamically in pulses of 0.8 s with a recovery time of 4.6 s in which a current density of 0 mA/cm^2 is applied. These pulses are constantly repeated for 180 min.

In the case of the InP membrane coated with 8 nm of Al_2O_3 by atomic layer deposition (ALD), a constant DC current density of –17 mA/cm^2 is applied for 120 min.

FeCo deposition

A galvanodynamic deposition in pulses is performed for the FeCo deposition in InP membranes coated with 8 nm of Al_2O_3 by ALD. A current density of –15 mA/cm^2 is applied for 0.8 s followed by –5 mA/cm^2 for 4.6 s. These pulses are constantly repeated for 120 min.

3.6 Sample characterization

The structural analysis was performed with a FEI Helios D477 and a ZEISS Supra 55 VP SEM. The crystallinity of the samples was investigated using a SEIFERT XRD 3000 TT with a Cu K_α radiation with a wavelength of 0.154 nm. The magnetic properties were measured with a LAKESHORE 7300 vibrating sample magnetometer.

For the InP battery experiments half battery cells were prepared with the porous InP membrane as the anode and Li metal as cathode. The electrolyte used is a LP 30 electrolyte which is a conventional electrolyte for Li-ion batteries. The electrolyte consists of 1 mol/l of $LiPF_6$ in an 1 : 1 solution of ethylenecarbonate and dimethylcarbonate. In total 0.5 ml of this electrolyte is used for the half-cells. The separator was a glass fiber microfilter from Whatman with a typical pore diameter of 1 µm.

Cyclic voltammetry experiments were carried out with a scan rate of 0.1 mV/s in the voltage limits between 0 V and 2 V for 20 cycles. The operating voltage regime of the standard battery cycling experiments is between 0.15 V and 1.85 V. The charging rate is $C/10$ at room temperature meaning that the lithiation and delithiation of the anode takes 10 h each. In case of the uncoated InP anode, the anode is charged to the maximum anode

capacity in the first lithiation cycle. For further cyclings, the anode is only charged to 80 % of its maximum capacity. The lithiation was carried out under galvanostatic conditions until a voltage limit of 0.15 V is reached. At this point the charging mode is switched to potentiostatic mode. The galvanostatic charging is continued until the charging current declined to 10 % of its original value or when the capacity limit is reached. The same procedures hold also for the delithiation of the anode. When the discharging current is declined to 10 % of its original value, the discharging is switched to the potentiostatic mode until a voltage limit of 1.85 V is reached.

The procedure for charging and discharging of the Al_2O_3 coated InP anode is very similar. The voltage limits are changed to 0.3 V for lithiation and to 0.9 V for delithiation. The switch-off current limit is 2.8 % of the initial charging current.

Chapter 4

Results

This chapter presents the results on the formation of a single-crystalline InP membrane, the modification of membrane properties and the FFT-impedance spectroscopy of the membrane formation. The second part shows results on the cathodic post-etching of InP pore array and InP membranes. In the third part of the results chapter the galvanic deposition of metal clusters and nanowires in InP pore arrays and membranes is shown. In the following when referred to pore arrays, it is meant that the curro-pore array is unopened and still has the bulk InP back side, while membranes are opened pore arrays. The fourth part describes the results of single-crystalline InP membranes as anode material in Li-ion batteries.

4.1 InP membrane fabrication process

The membrane production process in single-crystalline InP consists of three major parts. At first, the current-line oriented pores (curro-pores) are electrochemically etched in the InP wafer followed by the photo-electrochemical porosification with crystallographically oriented pores (crysto-pores) of the remaining bulk back side of the InP wafer. The third step is the photochemical dissolution of the highly porous back side of the InP wafer.

4.1.1 Electrochemical etching of the curro-pore array

As described in section 3.5.1 a curro-pore array is electrochemically etched in a single-crystalline InP wafer in a self-organized manner. Due to the very short high voltage pulse in the beginning of the electrochemical etching process the pore nucleation is very homogeneous resulting in an ordered array of curro-pores as shown in Fig. 4.1 a). The curro-pores are all aligned in parallel and exhibit a common pore front parallel to the surface of the wafer back side. The growth of the curro-pores is stopped as soon as the distance between the curro-pore tips and the surface of the wafer back side is reduced to approximately 40 µm or less. It is crucial that the curro-pore tips never reach the surface of the wafer back side, because this will result in the complete chemical dissolution of the pore array. Besides this, the distance between the curro-pore tips and the surface of the wafer back side should also not exceed much more than several tens of micrometers, for reasons that will be discussed in detail in section 4.1.2.

During the electrochemical pore formation a granular oxide layer is forming on the wafer back side, as shown in Fig. 4.1 a). The thickness of this oxide layer strongly depends

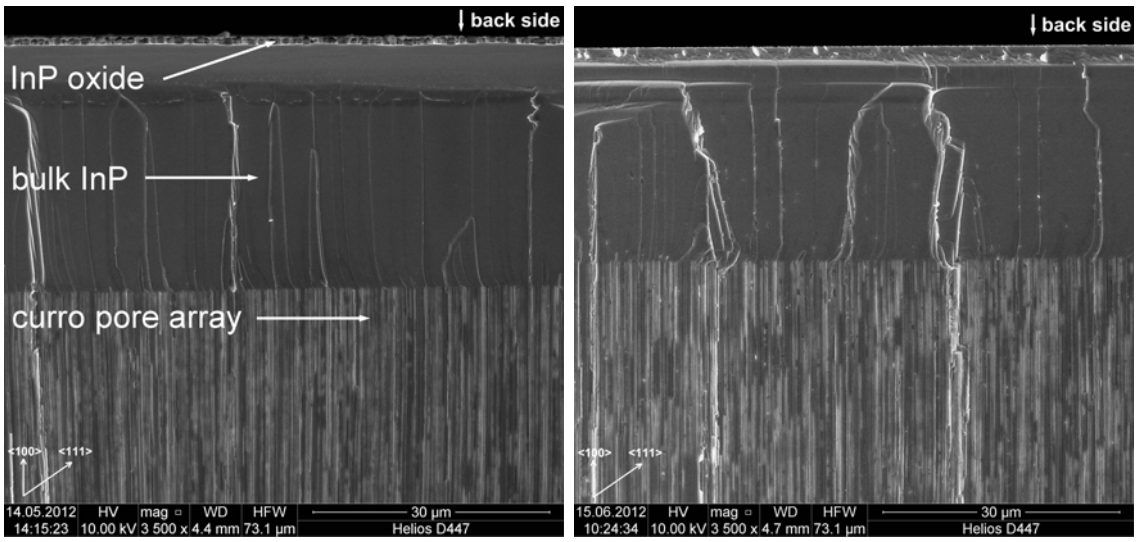

(a) (b)

Figure 4.1: Cross-sectional SEM images of the {110} plane of the curro-pore array close to the back side surface of the InP wafer after electrochemical pore formation a) as-electrochemically etched and b) after photochemical oxide layer removal. The vectors indicate the pore orientation.

on the electrochemical etching time of the curro-pore array. It is of high importance for the subsequent photo-electrochemical etching step to completely remove this oxide layer, since otherwise the nucleation of the crysto-porous layer would be inhomogeneous. After the photochemical dissolution of the oxide layer the resulting surface of the wafer back side is smooth and even, without any crysto-pores forming at the surface of the wafer back side, as shown in Fig. 4.1 b).

4.1.2 Porosification of the bulk wafer back side by photo-electrochemical etching

There are two main issues in the porosification of the bulk wafer back side that needed to be overcome. The first issue is to avoid under-etching at the O-ring sealing the gap between the InP sample and the etching cell. This is important because the under-etching at the O-ring will result in the formation of electrolyte leakages and ,thus, in the destruction of the entire sample. The second issue is to prevent the destruction of the previously etched array of curro-pores when the crysto-pores reach the tips of the curro-pores. Therefore it is necessary that the etching process used for the porosification is either self-limiting or at least strongly slowed down as soon as the crysto-porous layer reaches the pore tips of the curro-pore array. These two issues are solved by using a low etching current density combined with a high illumination intensity of the back side with blue light as described in section 3.5.2. The high-intensity blue light is absorbed in the surface-near areas resulting in an increased dissolution rate of the surface-near crysto-porous layer. Using red light instead of blue light does not result in a surface-near dissolution of the crysto-porous layer, but in an increased porosity below the surface and the subsequent irregular delamination of the overlying crysto-porous layer. This indicates implicitly that diffusion is not the

decisive effect of the photo-generated minority charge carriers.

Figure 4.2 a) shows the crysto-porous layer at the back side surface of the InP wafer in the beginning of the photo-electrochemical dissolution step. The crysto-pores grew homogeneously from the surface into the depth. The surface is not flat anymore, but consists of triangular features. These features are the remaining pore walls of the crysto-pores that are being dissolved photochemically. Moreover, a significant increase in the crysto-pore size within the first hundred nanometers below the surface is found compared to the underlying crysto-pores. The depth to which an increase of the crysto-pore size is observed can be adjusted by the illumination intensity and is most probably directly

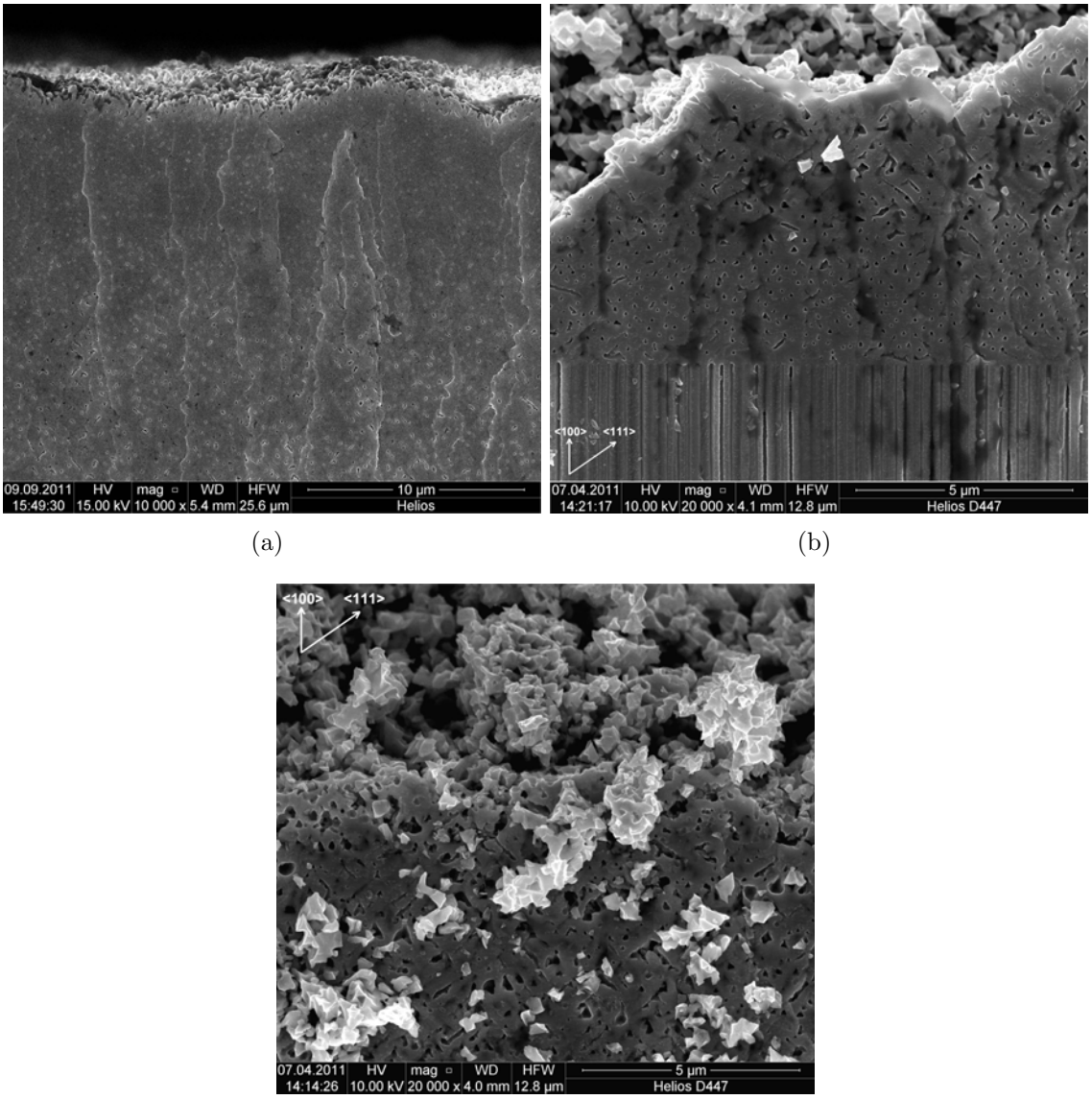

Figure 4.2: Cross-sectional SEM images of the $(1\bar{1}0)$ plane of the a) crysto-porous layer grown from the wafer back side, b) curro-pore array / crysto-porous layer interface in an intermediate state of the photo-electrochemical etching step, and c) magnified surface of the crysto-porous layer in an intermediate state of the photo-electrochemical etching step. The vectors indicate the pore orientation.

related to the ohmic losses in the electrolyte and the remaining crysto-porous layer.

In Fig. 4.2 b), the photo-electrochemical dissolution is stopped in the last part before switching to photochemical dissolution. The crysto-pores already reached the tips of the curro-pore array and the overlaying crysto-porous layer is reduced to about 10 µm. The growth of the crysto-pores into the depth stops almost completely at the tips of the curro-pores without destroying the pore walls of the curro-pores. An intergrowth of the crysto-pores into the curro-pore array is also not observed. The dissolution of the crysto-porous layer seems rather inhomogeneous, but this is just a cleavage artefact, since the crysto-porous layer is very brittle.

The highly magnified view on the surface of the crysto-porous layer is presented in Fig. 4.2 c). Since the used blue illumination has only a small penetration depth, the dissolution at the surface of the crysto-porous layer is facilitated and thus, the porosity of the top part of the crysto-porous layer highly increased. This finally leads to a lift-off of undissolved pore wall fragments, as shown in Fig. 4.2 c). This is an effective way to gradually thin the crysto-porous layer without destroying the underlying curro-pore array.

4.1.3 Photochemical dissolution of the porous wafer back side

The photochemical dissolution of the highly crysto-porous layer is the last step required to obtain the InP membrane. In Fig. 4.3 the photochemical dissolution is interrupted and shows a state in which the crysto-porous layer is not completely dissolved. The crysto-pore size is highly increased compared to the previous etching step [Fig. 4.2 a) and b)]. The remaining pore walls are only loosely connected, resulting in an increased dissolution due to the increased surface area. Even when the underlying curro-pore layer becomes visible – as shown in the top view on the crysto-porous layer in Fig. 4.3 b) – no relevant diameter increase of the curro-pores or intergrowth of crysto-pores into the curro-pore array is observed, although the pore walls of the curro-pores are also illuminated.

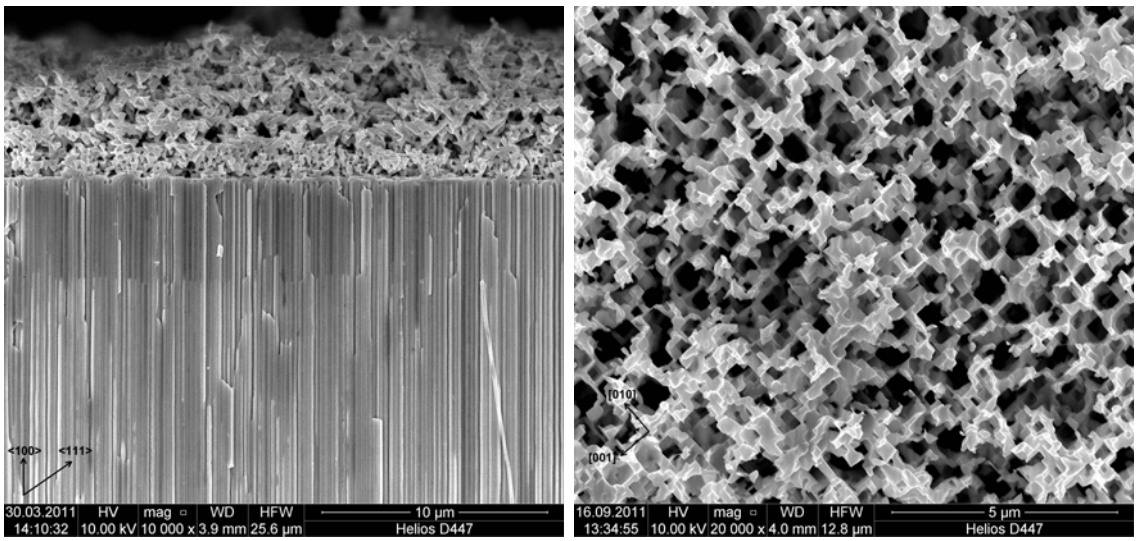

(a) (b)

Figure 4.3: a) Cross-sectional SEM view on the $(1\bar{1}0)$ plane of the InP membrane in the last phase of the membrane formation, b) top view on the (100) plane of the crysto-porous layer. The vectors indicate the pore orientation.

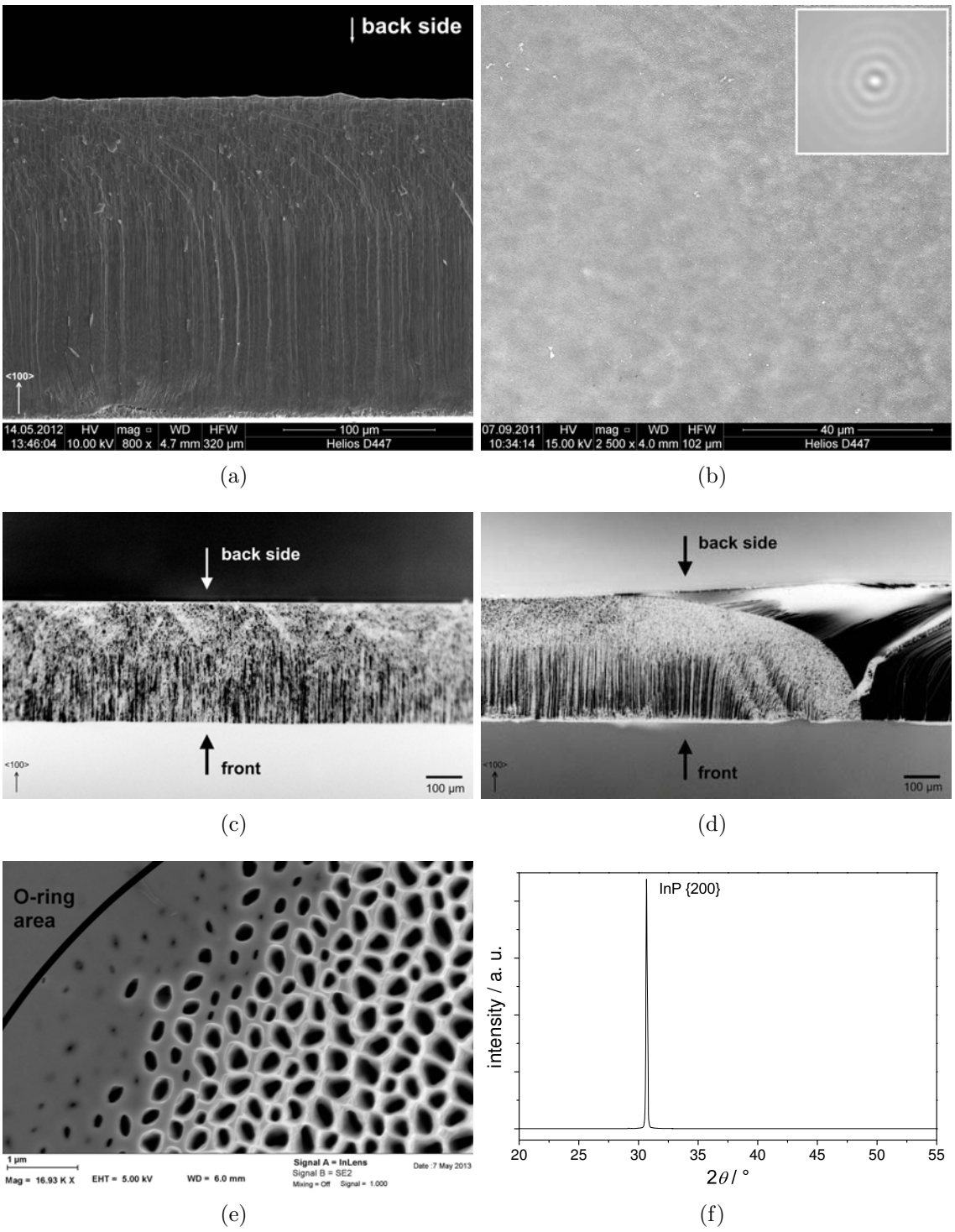

Figure 4.4: a) Cross-sectional SEM image of the {110} plane of the membrane center after complete photochemical dissolution of the crysto-pore layer, b) top view on the (100) plane of the opened back side, inset: auto-correlation function; cross-sectional optical microscopy images of the {110} plane of c) the membrane center of a thicker membrane, d) the outer part of the membrane in the surroundings of the O-ring, e) SEM top view near the O-ring, and f) XRD pattern of a completely processed InP membrane. The vectors indicate the pore orientation.

When the photochemical dissolution is continued to the end, the crysto-pore layer is completely dissolved resulting in an open InP membrane as shown in Fig. 4.4 a). The top view on the membrane back side directly after the photochemical etching – given in Fig. 4.4 b) – shows an extremely homogeneous surface without any remaining crysto-porous parts. The inset in Fig. 4.4 b) is the auto-correlation function of the porous InP membrane structure of Fig. 4.4 b). It clearly shows the six-fold symmetry of the hexagonally close-packed arrangement of the curro-pores. The correlation length extends up to the fifth nearest neighbor which is very high for structures grown in a self-organized manner. This means it is possible to achieve an extremely regular pore pattern and an almost constant pore wall thickness across the entire sample by self-organized pore etching.

In principle, the thickness of the membrane can be freely adjusted. There are two natural limits for the membrane thickness. The first is that the maximum membrane thickness is limited to the thickness of the starting wafer. The second limit is given by the mechanical stability of the membrane during the fabrication processes defining the minimum thickness. Self-evidently, it is much easier to fabricate a thin membrane starting from a thin InP wafer, since the growth depth of the crysto-pores is highly restricted by the concentration of the reactive species in the electrolyte and the etching current density. Figure 4.4 a) and c) show InP membranes with two different thicknesses, one with about 210 µm thickness [Fig. 4.4 a)] and a membrane with an 50 % increased thickness of 330 µm [Fig. 4.4 c)]. The typical aspect ratio of 210 µm thick membranes is about 1500:1, but it can be easily increased up to about 3300:1, if an InP starting wafer with a thickness of 500 µm is used. Nevertheless, thin InP membranes can also be obtained by sequential thinning of the bulk wafer back side when using a thick InP wafer. The sequential thinning requires a precise process control to obtain a homogeneous membrane surface back side.

Figure 4.4 d) presents a cross-sectional view on the outer part of the membrane near the O-ring. No under-etching near the O-ring is detectable on the back side of the membrane. The top view on the O-ring membrane back side in Fig. 4.4 e) shows that the dissolution of the wafer back side is significantly reduced near the O-ring compared to the remaining back side, leaving a transition line of partially open curro-pores of about 2 µm between the opened membrane and the bulk surrounding of the membrane.

The x-ray diffraction pattern of a typical InP membrane is presented in Fig. 4.4 f). It shows only one extremely sharp and narrow peak which is identified as the {200} peak of InP with a zinc blende crystal structure. This is a clear hint that the pore walls of the InP membrane remain single-crystalline after electrochemical pore etching and the photo-electrochemical / photochemical membrane etching step. Since the used InP wafers exhibits a (100) crystal orientation, it is not astonishing that the pore walls of the completely processed membrane also shows this crystal orientation.

4.1.4 Tailoring the InP membrane back side surface by photo-electrochemical / photochemical etching

Certain applications require a modification of the membrane properties, such as the surface of the membrane, the pore shape, or the mean pore wall width. For other applications, such as cell cultivation experiments or as substrate for the deposition of catalysts, it may be favorable to keep a crysto-porous layer on top of the curro-pore array. The results of the tailoring of the membrane back side surface are presented in this section, while the results on modifying the pore shape and the mean pore wall width are presented in

section 4.2 where the results of post-etching of InP pore arrays and membranes under open circuit conditions and cathodic bias are described.

Tailoring the InP pore openings of the membrane back side

The shape of the pore opening of the membrane back side can be tailored by adjusting the applied photo-current during the photo-electrochemical and photochemical etching process and by the photochemical etching time. The pore opening can be varied between flat or cone-like. Applying a high photo-current density during the complete photo-electrochemical and photochemical etching process results in a flat membrane back side

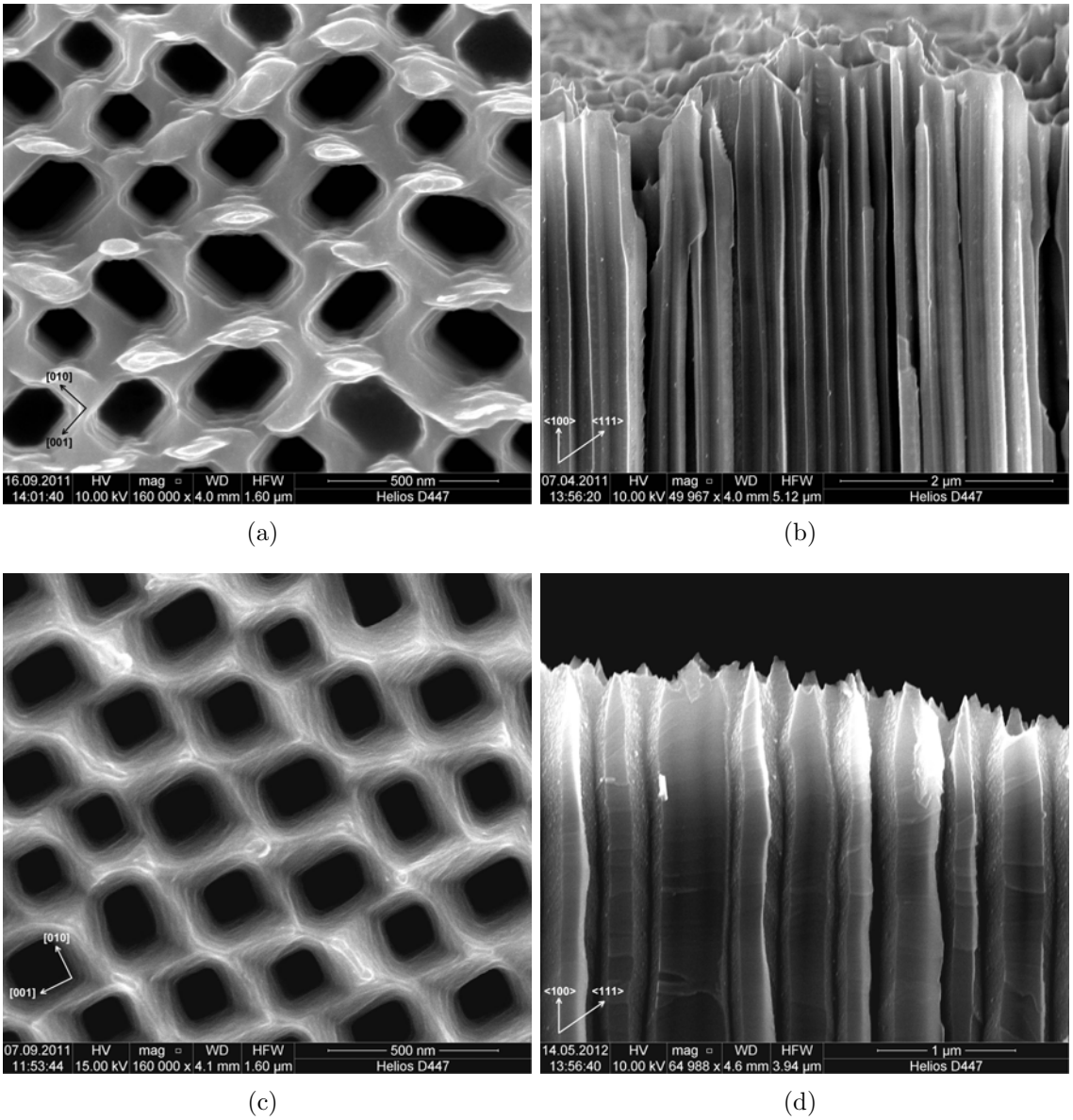

Figure 4.5: SEM images of the InP membrane after complete removal of the crysto-porous layer at high photo-current density, a) top view, b) cross-sectional view on the {110} plane, and at low photo-current density and extended photochemical etching time, c) top view, and d) cross-sectional view on the {110} plane. The vectors indicate the pore orientation.

surface, as shown in Fig. 4.5 a) and b). If the applied photo-current is reduced by a factor of 10 and the photochemical etching time is extended simultaneously, a sharpening of the pore walls is found resulting in cone-like pore openings as shown in Fig. 4.5 c) and d).

Crysto-porous layer on membrane back side

A crysto-porous layer on top of the curro-pore array is an intermediate state in the membrane fabrication process, as already presented in section 4.1.2. This layer can be maintained on top of the membrane back side by decreasing the etching times of the photo-electrochemical process step. The subsequent photochemical etching step can be used to adjust the resulting crysto-pore surface. The macroscopic surface – shown in

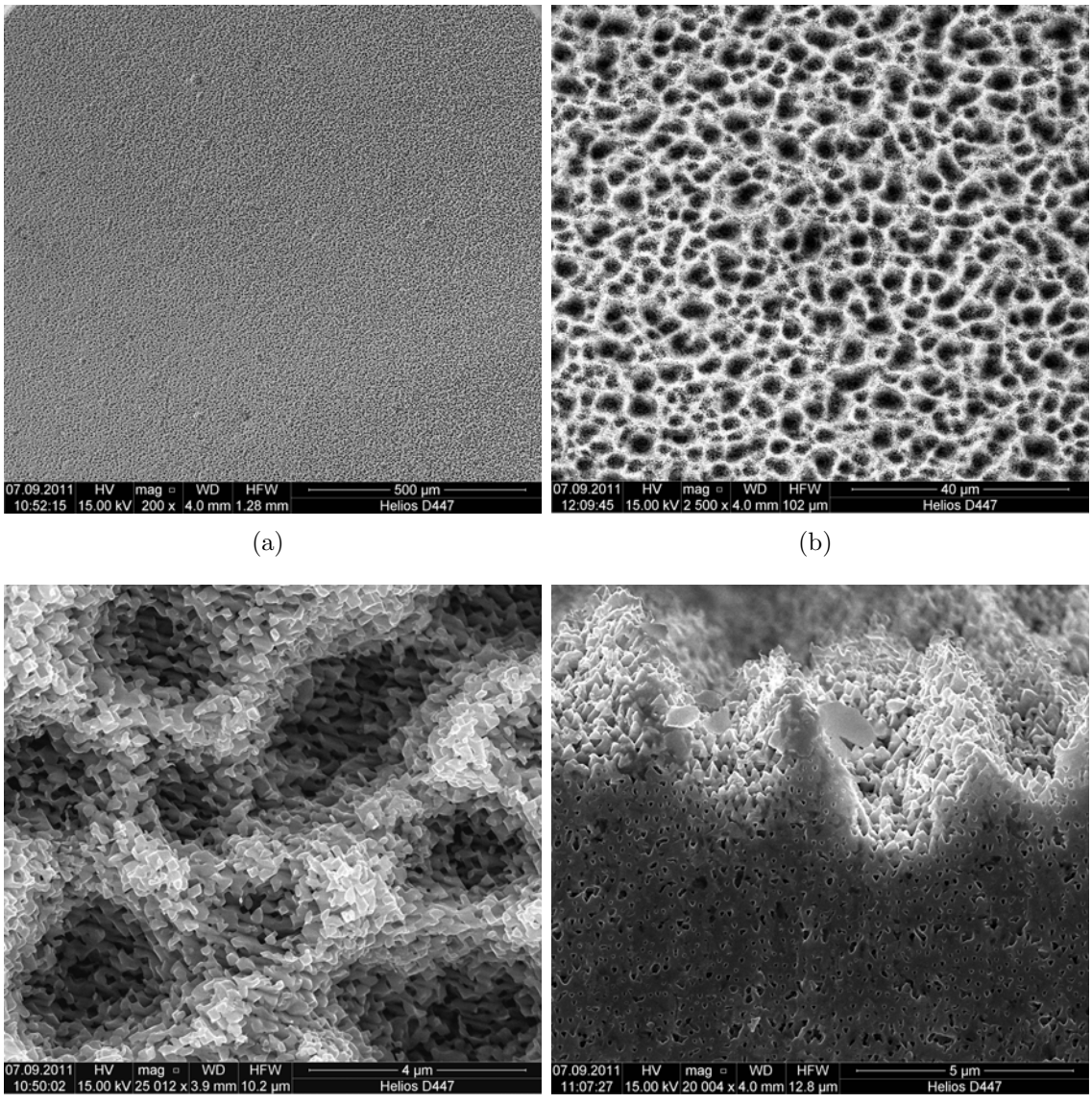

(a) (b)

(c) (d)

Figure 4.6: a) SEM top view on the back side surface of the InP membrane with crysto-porous top layer, b) micron-scale view, and c) submicron-scale view and d) cross-sectional SEM view on the {110} plane of the top part of the crysto-porous layer.

Fig. 4.6 a) – is very homogeneous. Zooming in into the micrometer-scale of the surface structure, as done in Fig. 4.6 b), exhibits an up-hill and down dale structure consisting of roundish bows that are separated from each other by interconnectioned walls. A further zoom-in given in Fig. 4.6 c) reveals mesoscopic cones in sizes ranging from around 2 µm to 8 µm. The interconnected walls are not bulk InP, but crysto-porous with a terraced slope. The surface of the walls consists of nanoscopic needle-like structures as shown in Fig. 4.6 d). The typical depth of these bows is in the range of several microns. This structure is formed in a self-organized manner and provides an ultra-high surface area with its micro-topographic and nano-sized structure.

4.1.5 FFT-impedance spectroscopy of the photo-electrochemical and photochemical etching process

The impedance data were recorded as stated in the experimental chapter in section 3.5.2. All impedance data could be very well fitted by using a simple model consisting of one resistor R_s which is connected in series with a parallel arrangement of a resistor R_p and a capacitor C_p. This fitting model applies for the photo-electrochemical and the photochemical etching process. In Fig. 4.7 the typical Nyquist plot obtained from FFT during the membrane fabrication process is presented. The small boxes are the measured data, while the black line is the result of the fitting with the model described above. Figure 4.7 illustrates clearly the high quality and stability of the used fitting model.

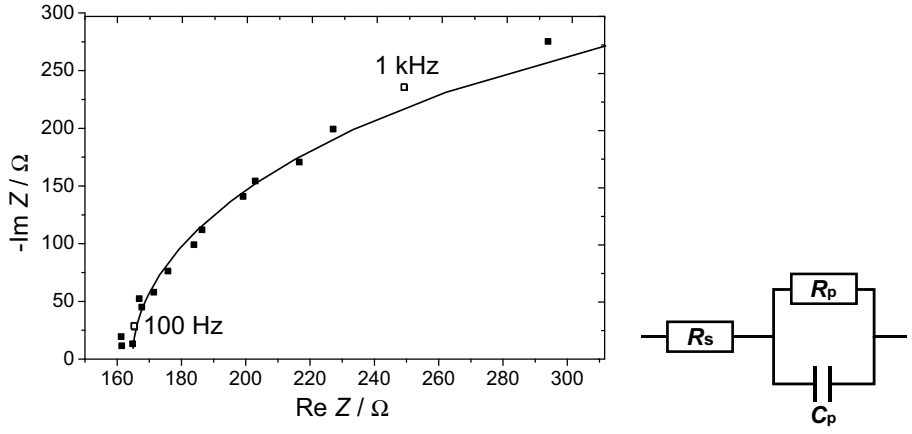

(a) (b)

Figure 4.7: a) Typical Nyquist plot of the FFT-IS measurement during the membrane fabrication process. The small boxes are the measured data. The black line is the fit. b) Corresponding electric equivalent circuit.

Photo-electrochemical etching step

The time dependence of the measured etching voltage U and the three fit parameters, the series resistance R_s, the transfer resistance R_p, and the capacity C_p, during the photo-electrochemical etching process at a current density of 12 mA/cm^2 and blue illumination is shown in Fig. 4.8. Quite obviously, the time curve of the etching voltage U has four different slopes. Thus, it can be subdivided into four regions as marked by the dotted

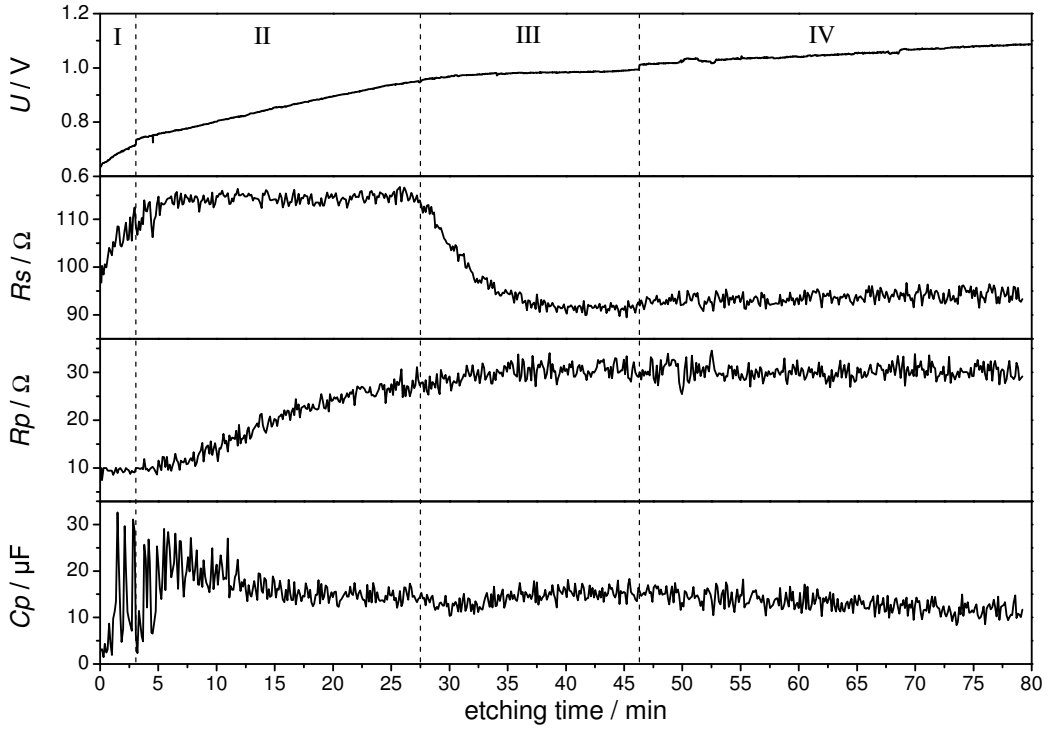

Figure 4.8: Etching voltage U and the fit parameters, the series resistance R_s, transfer resistance R_p, and capacity C_p, as a function of the photo-electrochemical etching time at a constant etching current density of 12 mA/cm^2 and blue illumination.

vertical lines in Fig. 4.8. Corresponding to the changes in the slope of the etching voltage-time curve, the three fit parameters show significant changes in their time dependence. This shows impressively that the impedance data contain additional information and allow to separate different stages in the photo-electrochemical etching process which are not easily identified from the etching voltage-time curve alone. In region I, the series resistance R_s is linearly increasing, while the transfer resistance R_p remains constant and the capacity shows heavy oscillations. In region II, R_s stays constant, while R_p is increasing and C_p decreases. The most prominent region is region III because here, R_s declines exponentially, R_p reaches its saturation value and U and C_p remain basically constant. In region IV, R_s and R_p remain constant, while C_p slightly decreases.

Photochemical etching step

In Fig. 4.9 the time dependence of the measured etching voltage U and the three fit parameters, the series resistance R_s, the transfer resistance R_p, and the capacity C_p during the photochemical etching process at a current density of 0 mA/cm^2 and blue illumination is shown.

Figure 4.9 a) is a typical example for a homogeneous and perfectly proceeded photochemical etching step. The transition from the photo-electrochemical to the photochemical etching step is discontinuous in the applied etching current density. This discontinuity is also found in the etching voltage U and the transfer resistance R_p, while the series resistance R_s and the capacity C_p are continuous. After a certain moment in time – marked by the vertical dotted line – a dip in R_s occurs.

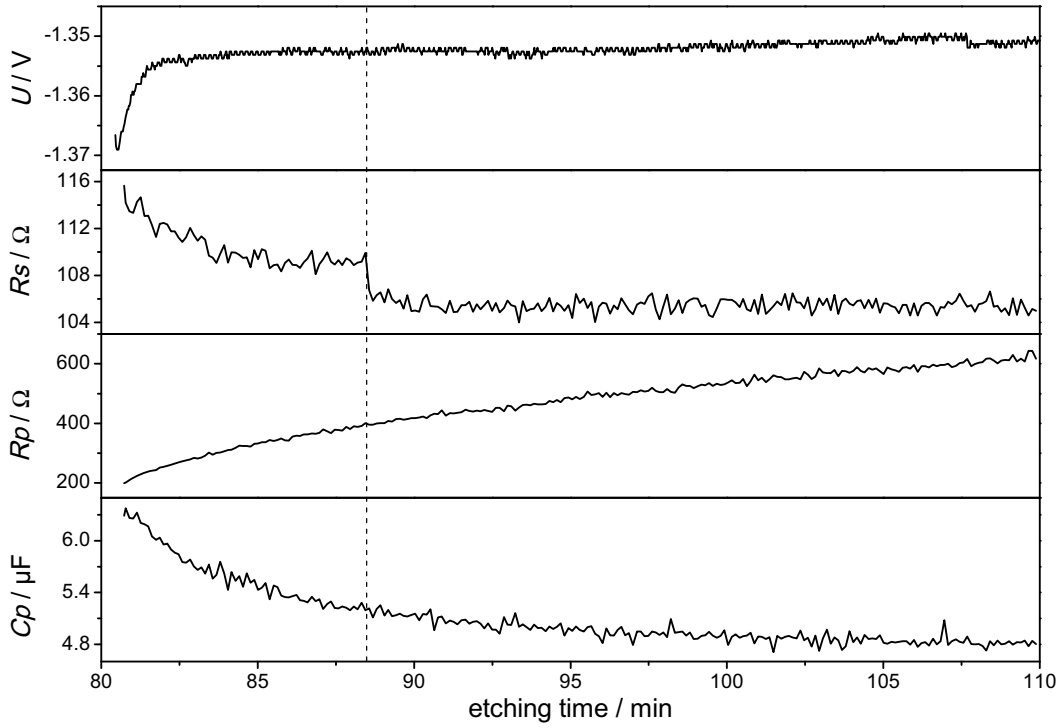

(a)

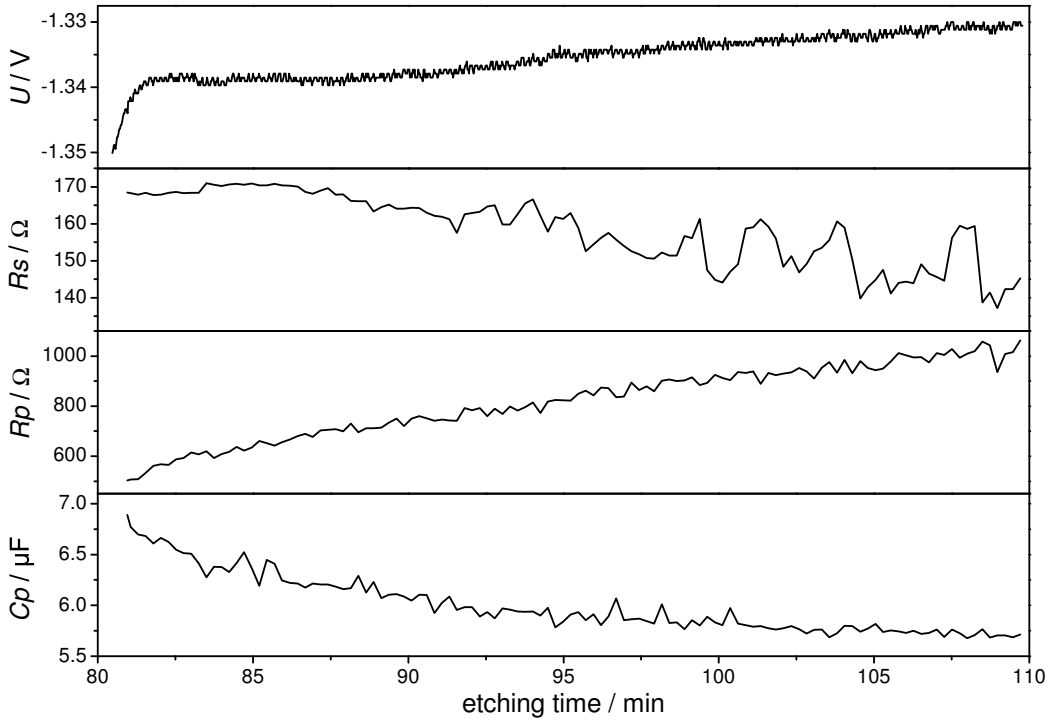

(b)

Figure 4.9: Etching voltage U and the fit parameters: the series resistance R_s, transfer resistance R_p, and capacity C_p as a function of the photo-electrochemical etching time at a constant current density of 0 mA/cm^2 and blue illumination for a a) homogeneously and perfectly elapsed and b) inhomogeneous and flawed photochemical etching process.

Besides the characterization of the membrane fabrication process, the FFT-impedance spectroscopy also helps to identify malfunctions during the photo-electrochemical and photochemical etching processes, so that it is possible to react to appearing issues, e.g. by adaption of process parameters. Figure 4.9 b) provides a nice example for such malfunctions. Looking at R_s, one observes strong oscillations starting in the middle of the photochemical etching after around 95 min. These oscillations are not found in the voltage or any other fit parameter. The ex-situ optical inspection of the membrane back side after the completed etching step revealed silvery round spots where the membrane is unopened. This indicates the formation of gas bubbles on the back side, as will be discussed in more detail in section 5.1.3.

4.2 Post-etching of porous InP under cathodic bias

It is possible to modify the mean pore wall width and the cross-sectional pore shape of InP pore arrays and membrane by chemical post-etching. As described in the experimental section 3.2.2 the used post-etching electrolyte contains hydrofluoric acid as etchant, nitric acid as oxidant, ethyl alcohol and acetic acid as surfactant, and the ethyl alcohol also for passivation. This electrolyte has been optimized to exhibit an isotropic etching behavior over the entire pore length accompanied by a low etching rate [30, 77]. The most important feature of this electrolyte is the self-limiting etching behavior in InP, i.e. the post-etching is stopped automatically in a self-organized manner as soon as the space charge regions surrounding each pore start to overlap [77]. A further self-limited and isotropic reduction of the mean pore wall width is only possible if the width of the SCR around each pore is decreased, so that more InP area, which is unprotected by the SCR, can be dissolved before the etching stops again. This can be done by applying a cathodic bias to the InP pore arrays or membranes during the post-etching. Besides the effect on the SCR, the cathodic bias also slows down the anodic dissolution of InP pore walls, but the oxidative power of HNO_3 remains, so that the anodic dissolution continues even under cathodic bias.

In addition to the influence on the electric properties of porous InP, the post-etching has also an effect on the mean pore wall width and on the cross-sectional shape of the pores, which is described in the following paragraphs.

4.2.1 Modifying the pore shape of pore arrays and membranes

By purely chemical post-etching under open circuit conditions it is possible to modify the cross-sectional shape of the curro-pore from nearly rectangular / square-like, see Fig. 4.10 a), to elliptical / roundish, see Fig. 4.10 b). The edges of the pores are less straight and tend to bulge out. It is clearly visible that the pores have expanded into these directions where the space charge regions of neighboring pores are not preventing the dissolution. Thus, the homogeneity of the pore distribution increases. Varying the post-etching time between no post-etching and self-limited post-etching time (around 48 h) leads to intermediate pore shapes, such as rectangular / square-like pores with rounded-off corners, but with still almost straight edges.

By applying an additional cathodic bias to the InP pore array during the post-etching, the pore shape changes again to rectangular / square-like with slightly rounded corners,

but with straight edges. The strong size difference between rectangular and square-like pore almost vanishes and is barely visible.

The application of a cathodic bias to an InP membrane during post-etching results in a highly rectangular / square-like pore shape depicted in Fig. 4.10 d). The corners of the rectangles / squares are very pronounced and show a nearly perfect right angle. Due to the applied cathodic bias the pore walls are extremely straight and have an almost equal thickness. The size difference between rectangular and square-like pores is slightly reduced compared to the only electrochemically etched pores [Fig. 4.10 a)], but more pronounced than for cathodically post-etched pore arrays. If corners of two neighboring pores are meeting along a ⟨110⟩ direction and the distance between both is sufficiently small, as shown in the bottom center of Fig. 4.10 d), the pore wall can be completely dissolved and the two pores can intergrow, while all other pore walls are maintained. This is possible because at these adjacent corners the electric field strength is much higher due to the extremely small curvature radius of the corners compared to other corner arrangements and edges. Already a slight offset between the corners prevents the occurrence of the above described pore intergrowth. The inset of Fig. 4.10 d) shows the auto-correlation function up to the nearest neighbor of the porous structure directly after cathodic post-etching. The six-fold symmetry indicated by the six bright peaks around the center peak is maintained throughout the cathodic post-etching step – as expected. Thus, the curro-pores are growing in an almost perfect hexagonal arrangement. The center peak exhibits a four-fold symmetry indicated by the two perpendicularly crossed black rays in the corners of the center. This is due to the preferential alignment of curro-pores, which are oriented either in [001] or [010] direction. This alignment is best shown by the larger, rectangular curro-pores shown in Fig. 4.10 d). Besides this, there is no evidence indicating a preferential choice for one of these two directions.

4.2.2 Modifying the mean pore wall width of InP pore arrays and membranes

The typical mean pore wall width of InP pore arrays and membranes obtained after electrochemical etching – as described in 3.5.1 – lies in the range of 190 nm and 220 nm. The mean pore wall width of the just electrochemically etched pore array shown in Fig. 4.10 a) is about 220 nm. One can clearly see that the pore wall width [see left part of Fig. 4.10 a)] between large rectangular pores is significantly larger than between smaller square-like pores. This is an effect of the self-organized nucleation and growth of the curro-pore array. For an InP wafer with a given carrier concentration, the mean pore wall width is basically determined by the anodic etching potential during the electrochemical pore etching. If the anodic pore etching voltage is below a certain limit depending on the charge carrier concentration of the wafer, no close-packed array of straight curro-pores is formed, but an array of curvy pores with varying diameters are obtained. Above a certain anodic pore etching voltage an uncontrolled dissolution of the wafer occurs. Thus, the variation of the mean pore wall width by electrochemical pore formation for a given charge carrier concentration is very limited.

After post-etching under open circuit conditions for 48 h the mean pore wall width of the pore array, shown in Fig. 4.10 b), can be reduced down to about 150 nm. A further extension of the post-etching time will not further decrease the mean pore wall width due to an overlapping of SCRs surrounding each curro-pore, thus, a further dissolution of the

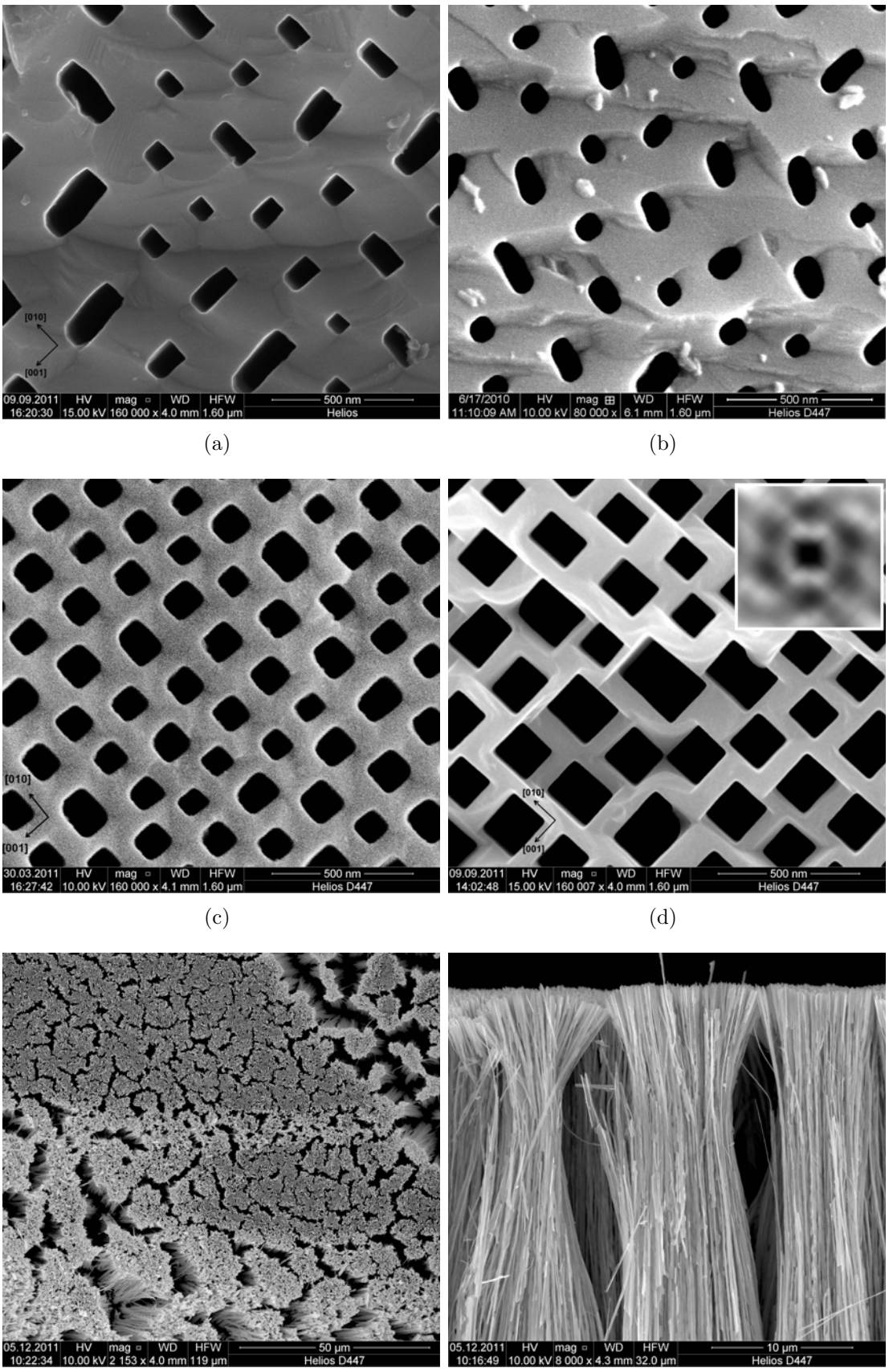

(a) (b)

(c) (d)

(e) (f)

Figure 4.10: SEM top view on the curro-pore array a) as electrochemically etched, b) post-etched under open circuit conditions, c) post-etched under cathodic bias, and d) on the membrane back side after post-etching under cathodic bias, e) under too high cathodic bias; f) same sample in cross-section. The vectors indicate the pore orientation.

pore walls is almost completely stopped.

Applying an additional cathodic bias during post-etching causes a further decrease in the mean pore wall width compared to the post-etching under open circuit conditions. The average pore wall width of the pore array presented in Fig. 4.10 c) is about 100 nm. The mean pore wall width can be adjusted by varying the magnitude of the cathodic bias. Since the post-etching of the InP pore arrays is performed in an electrochemical double cells, the cathodic bias results in a slight etching of the bulk back side. Higher cathodic bias voltages result in an uncontrolled chemical dissolution of the bulk back side and finally in the destruction of the pore array. The problem of the dissolution of the back side does not apply to membranes, because here the bias voltage is directly applied to the membrane and electrolyte is pumped through the membrane. This allows also to apply high cathodic bias voltages. Figure 4.10 d) shows the resulting pore structure of a membrane post-etched under a cathodic bias of about -0.3 V. The mean pore wall width is decreased from around 220 nm to around 80 nm. By varying the post-etching voltage it is possible to tune the mean pore wall thickness to the desired value.

In Fig. 4.10 e) the pore structure of a membrane after post-etching under a high cathodic bias voltage is shown. Small tufts with sizes of around 10 µm have formed. These tufts consist not only of single pore walls – see the mid and bottom part of Fig. 4.10 e), but also of small still connected pore walls [top part of Fig. 4.10 e)]. A cross-sectional image of single tufts is presented in Fig. 4.10 f). They look like typical wheat sheaves. Due to the "wet hair effect" the nanowires stick together. The controlled collapse of the pore structure can be used to produce single-crystalline InP nanowires.

4.2.3 Parallelization of the post-etching process

There is a great need to have a high number of post-etched InP pore arrays and membranes for the galvanic metal deposition experiments inside the pores. The issue here is that the post-etching step takes 48 h for each membrane. This issue can be overcome by parallelization of the post-etching process. The post-etching under open circuit conditions can be easily parallelized by immersing the InP pore arrays in the post-etching electrolyte under constant stirring for 48 h. Post-etching under cathodic bias requires, in principle, a single electrochemical cell, a separate potentiostat, and a separate temperature controlled electrolyte container for each pore array / membrane, which is not feasible in a typical university lab, since it requires too much equipment.

As described in more detail in section 3.2.2, three electrochemical cells are electrically connected in parallel. Each cell is fed with the post-etching electrolyte from a common temperature controlled electrolyte container. This post-etching setup can be extended by adding more cells in series to the three starting columns. The maximum number of InP membranes that have been post-etched in single electrochemical cells in parallel are nine membranes. It can be clearly seen in Fig. 4.11 that parallel post-etching of nine membranes under cathodic bias produces acceptable results with respect to the mean pore wall width. Only slight differences in the mean pore wall width within a single column and between different columns are detectable. These differences originate not only from the post-etching step, but can be also attributed to slight variations in the carrier concentration over the InP wafer resulting in small differences in the mean pore wall width after anodic pore formation. Although working properly, it is not advisable to post-etch more than three pore arrays / membranes under cathodic bias at the same

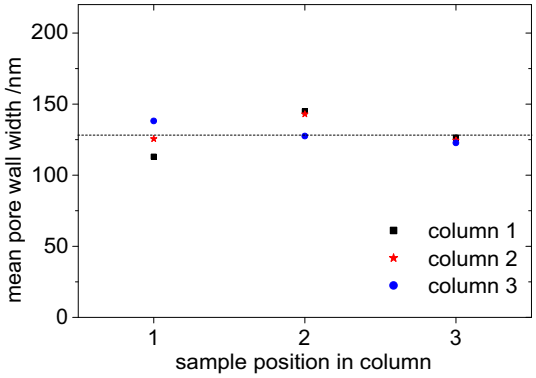

Figure 4.11: Post-etching under cathodic bias of three parallel columns, each consisting of three cells connected in series. The dotted line represents the overall mean pore wall width.

time, because a single failure in one of the electrochemical cells can destroy all membranes at the same time. Thus, the parallel post-etching of only three pore arrays / membranes represents the best compromise between homogeneity in pore wall width over all samples and manufacturing time.

4.3 Galvanic fabrication of magnetic nanostructures in porous InP

To obtain a multifunctional composite it is necessary to fill the porous InP pore arrays / membranes completely with a magnetic material. The most preferred technique for this purpose is the galvanic deposition, since it is a clean, cheap, and versatile technique. In general the galvanic deposition is a well characterized and highly often used technique in industry, but when it comes to nanogalvanics of high aspect-ratio porous semiconductors, galvanic processes are almost not investigated at all.

Typically, the galvanic deposition can be done potentiostatically, galvanostatically, or in a pulsed voltage or pulsed current mode. In contrast to the later discussed Al_2O_3 coated InP membranes, it turned out for high aspect ratio InP pore arrays that potentiostatic as well as galvanostatic deposition result in a preferential metal deposition near the pore openings. Thus, the pore openings are plugged after a very short time preventing the galvanic filling of deeper parts of the pores. This behavior is of course highly unwanted for a homogeneous pore filling and can be overcome e.g. by pulsed current deposition. Pulsed current deposition has the advantage that a metal ion depletion of the electrolyte in the deeper parts of the pores is effectively prevented, because each current pulse is followed by a recovery time for the metal ion concentration in the electrolyte.

The characterization of the magnetic metal nanostructures embedded in InP pore arrays / membranes is divided in two parts: structural and magnetic characterization. The structural characterization contains SEM and XRD analysis. The magnetic characterization contains VSM measurements, in the case of the solid nanowires also angular dependent VSM measurements. In addition, the *in situ* FFT-impedance data is measured for the galvanic growth of Ni nanowires in an InP membrane.

4.3.1 Structural characterization of the deposited magnetic nanostructures

Ni nanoparticles embedded in an InP pore array

Figure 4.12 a) presents the cross-sectional view on the InP pore array after the Ni deposition on the InP pore walls by pulsed current deposition. One observes a high density of Ni particles that are attached to the pore walls. These particles are homogeneously distributed over the entire length of the pore, from the pore opening down to the tips. The aspect ratio of the InP pore array – depicted in Fig. 4.12 a) – after electrochemical etching and post-etching is about 500:1. The deposited Ni particles seem to have a roundish shape and are of almost equal size. The average particle size is about 50 nm. At several positions, these particles have merged starting to form a tubular structure. The dark parts in Fig. 4.12 a) are areas where the pore structure is destroyed during sample cleavage necessary for the SEM analysis. This is not an intrinsic feature of the filled pore array. Further SEM images of this composite are depicted in higher magnification in the appendix A.1.

The XRD pattern of the Ni particles / InP pore array composite is depicted in Fig. 4.12 c). It shows one huge peak and several much smaller peaks. This huge peak is identified as InP {400}. Three peaks can be assigned to Ni, namely {111}, {200} and {220}. According to [80], two peaks refer to Ni_2O_3 {200} and {202}. The asterisk-marked peak cannot be related to InP, Ni, or Ni oxides and is rather an aperture artifact. The Ni crystallite size is estimated from the diffraction peaks by the Scherrer formula (Eq. 2.4). The average Ni crystallite size obtained from the three Ni peaks is about 10 nm.

To prevent the deposition of metal crystallites at the pore walls the pore array was covered by a 4 nm thick interlayer of SiO_2 to passivate the pore walls. Similar to the metal deposition in anodized aluminum oxide (AAO) pore arrays [58], a pulsed current is applied to the pore array, but not resulting in metal deposition [depicted in Fig. 4.13 a)]. Even the application of high electric fields under potentiostatic conditions does not result in an electric breakdown at the pore tips, so that no metal deposition is observed as shown in Fig. 4.13 b). Therefore, the following deposition experiments are performed only in InP membranes.

Porous Ni nanowires embedded in an InP membrane

The cross-sectional view on the porous Ni nanowires / InP membrane is depicted in Fig. 4.12 b). The aspect ratio of the InP membrane after electrochemical etching and post-etching is about 1600:1. One can see the 1 µm thick Ni plating base that was galvanostatically deposited prior to the pore filling on the bottom of the membrane. By pulsed current deposition, Ni particles are deposited on the pore walls of the InP membrane. The average Ni particle size is about 50 nm. By coalescence of these Ni particles porous Ni nanowires form, mostly starting from the Ni plating base. The porosity is a direct result of the growth mode, since the deposition of the Ni particles occurs on the InP pore walls, thus, narrowing the diameter of the pores so efficiently that a further Ni deposition is almost suppressed and the center of the pores remain basically open. Thus, the nanowires consists of an almost solid shell with mostly voids in the center of the nanowires. Further SEM images also in higher magnifications are depicted in the appendix A.2.

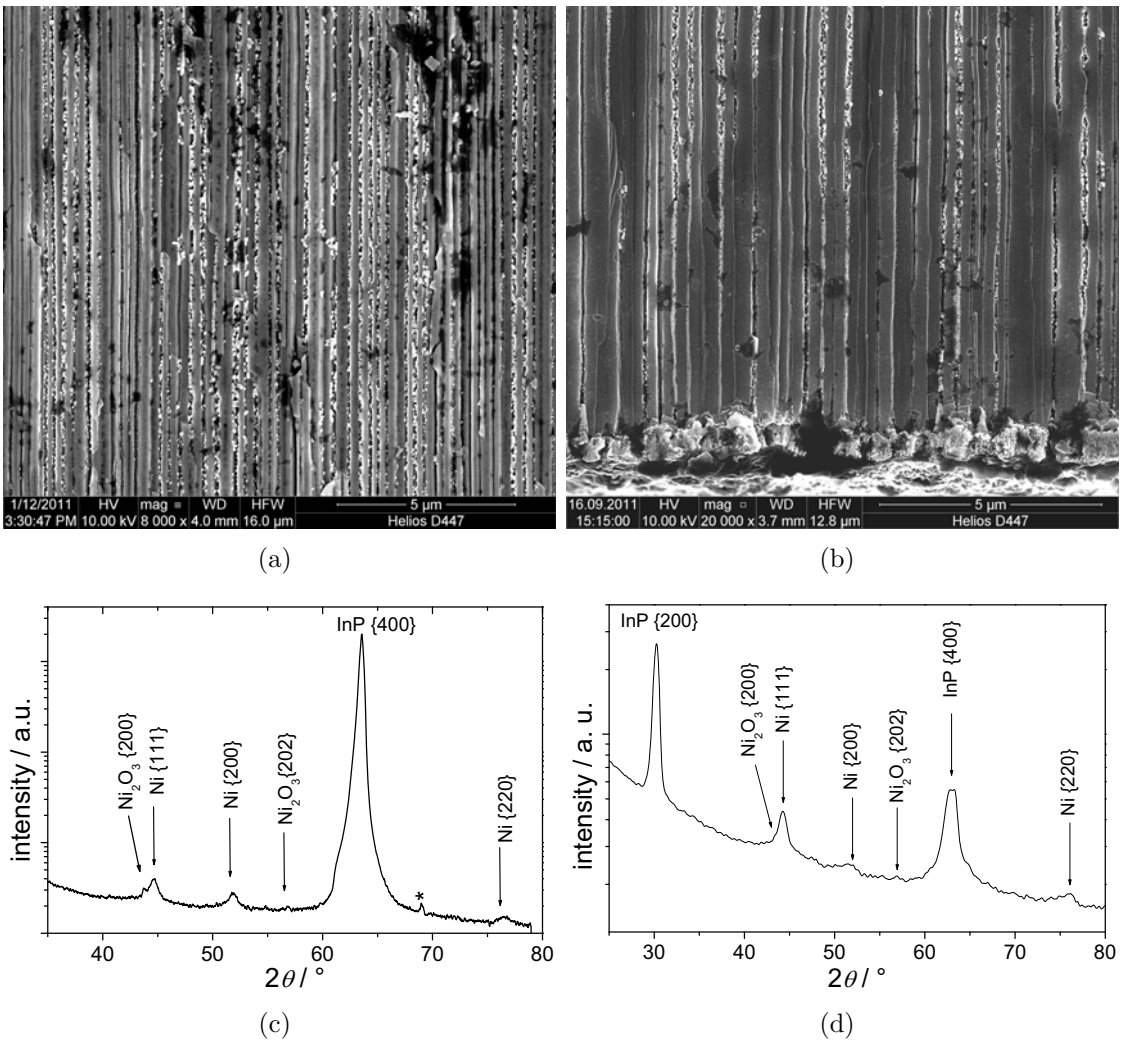

Figure 4.12: Cross-sectional SEM view on the a) Ni nanoparticles embedded in an InP pore array, b) porous Ni nanowires embedded in an InP membrane, c) XRD pattern of the composite from a), and d) XRD pattern of the composite from b).

Prior to the XRD measurement, the Ni plating base was mechanically ground off, so that the XRD analysis is free from effects of the Ni plating base. The porous Ni nanowires / InP membrane composite exhibits a similar XRD pattern. The two very pronounced peaks belong to InP {200} and InP {400}. Three peaks can be assigned to Ni, namely {111}, {200}, and {220}. The Ni {111} peak is very pronounced, in contrast to the Ni {200} and {220} peaks, which are very broad and indistinct. The Ni {220} peak is more distinct compared to the Ni {200} peak. As well as for the Ni particles / InP pore array composite crystalline Ni_2O_3 peaks are also found here. The Ni_2O_3 {200} peak positioned on the left slope of the Ni {111} peak is barely visible, while the Ni_2O_3 {202} peak is more pronounced. This is in good agreement with the relation between the Ni {200} and Ni {220} peak. The Ni crystallite size is estimated from the diffraction peaks by the Scherrer formula. The average Ni crystallite size obtained from the Ni {111} peak is around 10 nm, while the Ni {200} and {220} peaks yield a crystallite size of around 6 nm. This indicates a minor preference of the grain growth in ⟨111⟩ direction.

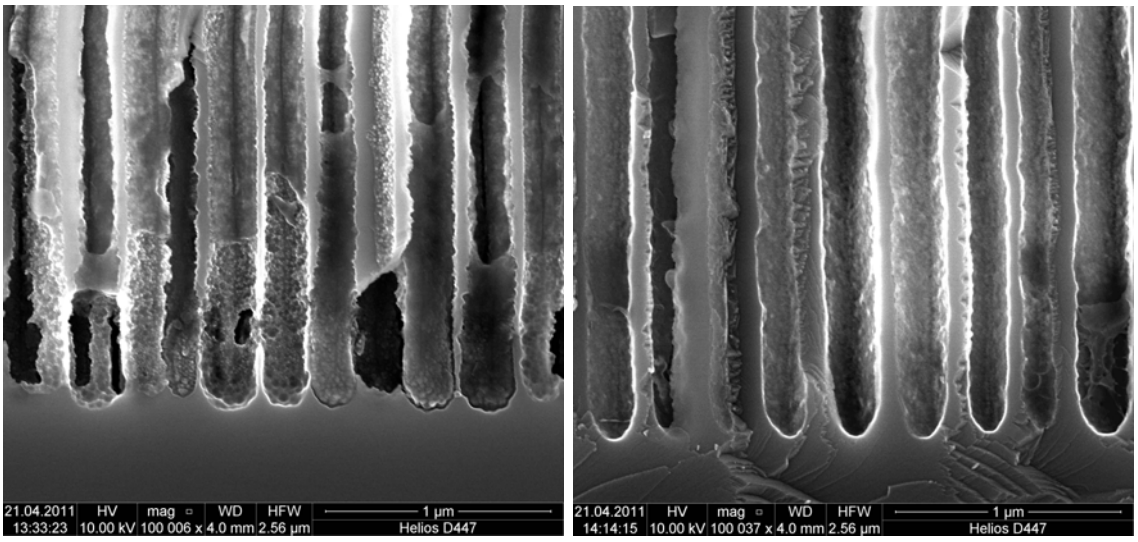

(a) (b)

Figure 4.13: Cross-sectional SEM view on the InP pore array with a SiO_2 interlayer prepared by ALD after a) pulsed current deposition and b) potentiostatic metal deposition.

Ni nanowires embedded in an InP membrane

A cross-sectional view on the Ni nanowires embedded in the InP membrane with an aspect ratio of about 1600:1 are shown in Fig. 4.14 a)–c). The InP membrane has been coated with about 8 nm of Al_2O_3. Single Ni nanowires can be easily identified in the SEM image in Fig. 4.14 a) if they are broken and sticking out of the InP host membrane. These breaks and the partial pull-out of the Ni nanowires as well as partially empty pores are the result of the sample cleavage for the SEM analysis and are not a property of the nanowires themselves. The interwire distance of the Ni nanowires is defined by the width of the InP pore walls. In the presented composite the interwire distance is around 100 nm. The galvanic Ni deposition is stopped before the pores of the InP are overfilled. Thus, these Ni nanowires exhibit an ultra-high aspect ratio of about 1000:1, which is lower than the aspect ratio of the pores of the InP membrane (1600:1).

From the higher magnification image shown in Fig. 4.14 b) it can be seen that the Ni nanowires exhibit a rectangular shape. This is an interesting feature, because the metal nanowires that can be obtained from other templates, such as anodic aluminum oxide membranes, are typically round. The Ni nanowires have a rectangular shape, since the InP membrane used as template consists of rectangular highly ordered pores – as shown in Fig. 4.10 d). The Ni nanowires completely fill out the free space of the pores, so that the Ni nanowires are the positive casts of the pores. This makes it tough to identify single Ni nanowires, as clearly seen in the right part of Fig. 4.14 b) where the bent nanowire is partially pulled out of the pore. At this position it is also visible that the Ni nanowires seem to be well mechanically deformable allowing even a bending angle of about 90° without fracture. The Ni nanowires start growing from the Au plating base deposited on the front side of the membrane. Also due to the sample cleavage single Ni nanowires are broken and partially pulled out of the membrane – as shown in the top part of Fig. 4.14 c). Further SEM images in higher magnifications are depicted in the appendix A.3.

The typical XRD pattern of a Ni / InP composite is presented in Fig. 4.14 d). Four

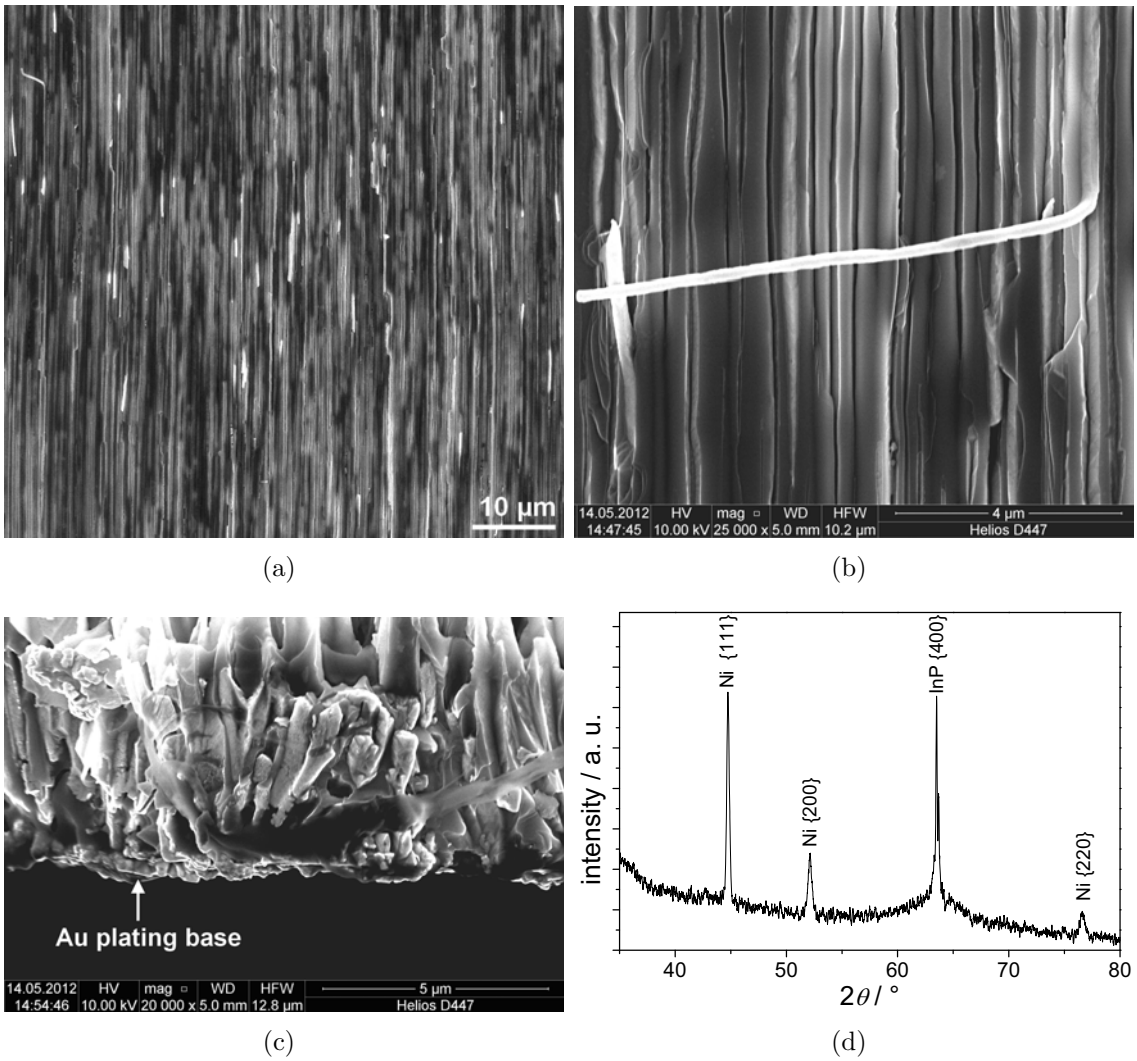

Figure 4.14: Cross-sectional SEM view on a) the Ni nanowires embedded in an InP membrane, b) ditto in high magnification, c) the seed layer and the root of the Ni nanowires and d) XRD pattern of the Ni / InP composite.

peaks are found. One peak can be assigned to InP, namely {400}, and three to Ni, namely {111}, {200}, and {220}. The diffraction pattern shows no additional peaks originating from the Au plating base or the Al_2O_3 interlayer on the pore walls. This means, the Au plating base and the Al_2O_3 are most probably amorphous. As already shown in Fig. 4.4 f) the InP pore walls of the unfilled membrane are single-crystalline. This single-crystallinity of the InP pore walls is still maintained after the deposition of the Al_2O_3 interlayer by ALD and the subsequent galvanic Ni deposition. The Ni nanowires exhibit the typical fcc crystal structure and are crystalline. Compared to the InP {400} peak, the Ni {111} and {200} peak exhibit the same sharpness. This is an indication for rather large areas that scatter the x-rays coherently. In contrast, the Ni {220} peak is far less pronounced. The Ni crystallite size is again estimated from the diffraction peaks by the Scherrer formula. For the Ni {111} peak the associated crystal size is about 60 nm, while it is around 20 nm for the Ni {200} and Ni {220} peak. This difference in the estimated crystal size is a hint for a preferential grain growth in the ⟨111⟩ direction within the Ni nanowires.

Fe-Co based nanowires embedded in an InP membrane

Cross-sectional views on the Fe-Co based nanowires embedded in the InP membrane with an aspect ratio of about 1600:1 are shown in Fig. 4.15 a)–c). Like for the Ni deposition, the InP membrane has been coated with about 8 nm of Al_2O_3. Single Fe-Co based nanowires can be easily identified on the SEM image in Fig. 4.15 a), especially when broken and sticking out of the host membrane. These nanowire fractures respectively pull-out of single nanowires as well as partially empty pores are the result of the sample cleavage for the SEM analysis and are not a property of the nanowires themselves. This situation is depicted in high magnification in Fig. 4.15 b) where the nanowire is missing in the outer right pore and the nanowire is broken in the neighboring pore to the left. The nanowire one further to the left shows partial break losses and the nanowire to the left is completely intact. Like the Ni nanowires, the Fe-Co based nanowires also exhibit a rectangular cross-sectional area as one can see in Fig. 4.15 b). The interwire distance is around 100 nm being identical to the Ni nanowire filled InP membranes. The aspect ratio of the grown

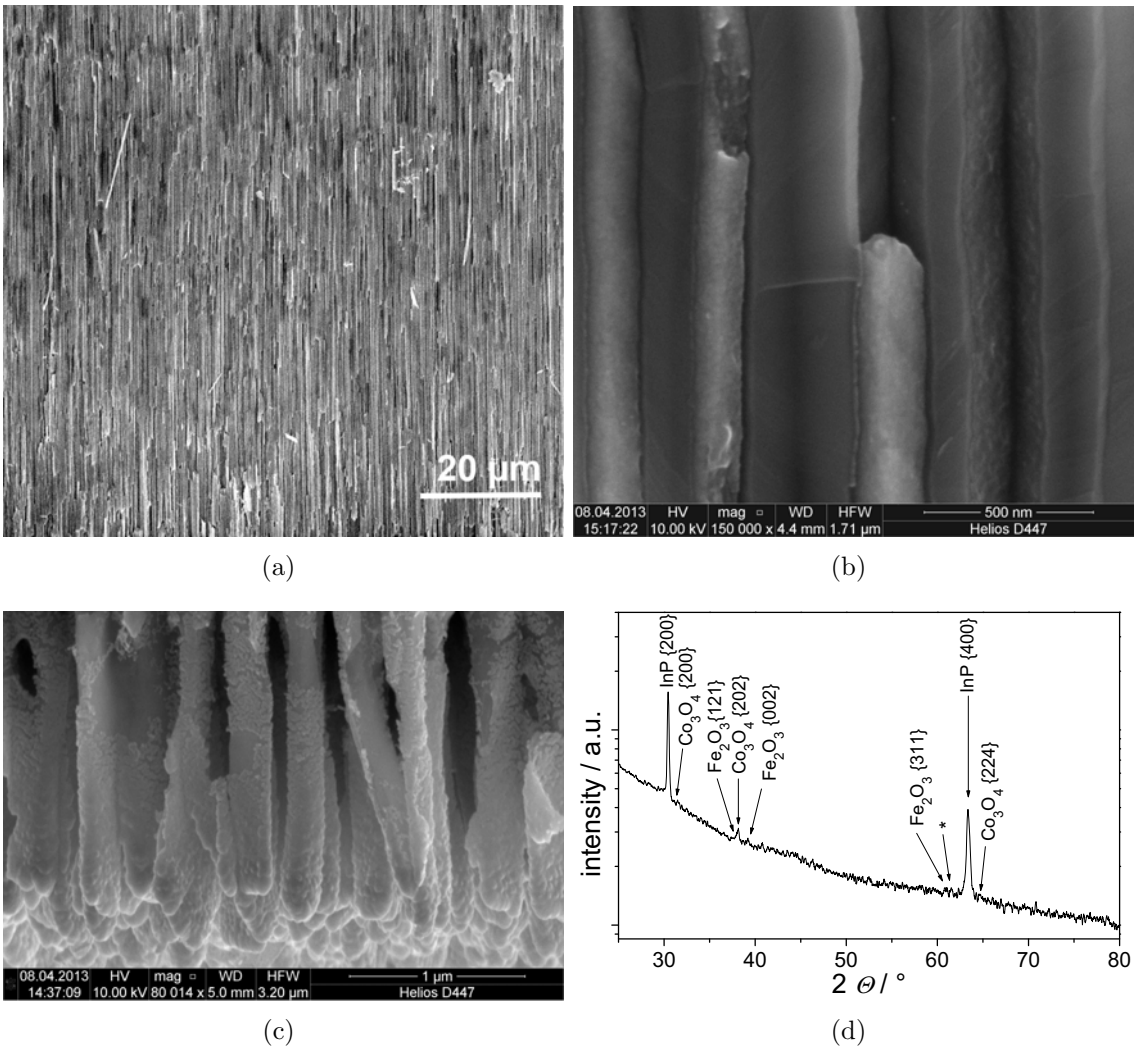

Figure 4.15: Cross-sectional SEM view on a) the Fe-Co based nanowires embedded in an InP membrane, b) ditto in high magnification, c) the seed layer and the root of the Fe-Co oxide nanowires and d) XRD pattern of the Fe-Co based nanowire / InP composite.

Fe-Co based nanowires is approximately 400:1. Figure 4.15 c) provides a magnified view on the roots of the nanowires. Evidently, the first line of nanowires is ripped out of the membrane at their root due to the sample cleavage. The wires seem to be covered with a skin-like layer at the roots that is not found further away from the nanowire roots. This skin layer is most probably part of the Al_2O_3 interlayer that was deposited on the InP membrane by ALD. The Fe-Co based nanowires start growing from the Au plating base which is also ripped off due to the sample cleavage. Further SEM images also in higher magnifications are depicted in the appendix A.4.

The XRD pattern of the Fe-Co / InP composite is depicted in Fig. 4.15 d). It shows a multitude of peaks. The two most pronounced and sharpest peaks belong to the single-crystalline InP matrix. The corresponding peaks are InP {200} and {400}. Two additional phases are identified, Fe_2O_3 and Co_3O_4. The Fe_2O_3 crystallizes in an orthorhombic crystal structure, in Hermann-Mauguin notation *Pnma* [81]. According to [81], the peaks found related to Fe_2O_3 are {121}, {002}, and {311}. The other phase is Co_3O_4 crystallizing in a tetragonal crystal structure, in Hermann-Mauguin notation $I4_1/amd$ [82]. The peaks found related to Co_3O_4 are {200}, {202}, and {224}. The single peak marked with the asterisk could not be related to any Co, Fe, or corresponding oxides. The observed peaks for Fe_2O_3 and Co_3O_4 are very small and hardly distinguishable from the background noise indicating rather small coherently scattering areas. Although no peaks for crystalline Fe or Co could be found in the XRD pattern, they may be still present, but are not detectable by XRD, e.g. due to the small crystallite size.

4.3.2 Magnetic characterization of deposited nanostructures

Ni nanoparticles embedded in an InP pore array

The magnetic properties of the Ni nanoparticles embedded in an InP pore array are analyzed by VSM measurements where the external magnetic field is applied in parallel to the long axis $\boldsymbol{z}$ of the pores ($\boldsymbol{H} \parallel \boldsymbol{z}, \alpha = 0°$) and perpendicular to $\boldsymbol{z}$ ($\boldsymbol{H} \perp \boldsymbol{z}, \alpha = 90°$). The resulting two hysteresis loops are depicted in Fig. 4.16 a). For $\alpha = 90°$ the hysteresis loop is very narrow. The remanence squareness is about 0.12 and the coercivity about 125 Oe. Compared to the $\boldsymbol{H} \perp \boldsymbol{z}$ case, the hysteresis loop in the $\boldsymbol{H} \parallel \boldsymbol{z}$ case is much broader and the slope of the hysteresis loop around the coercivity is much higher. The remanence squareness increases to about 0.33 and the coercivity to about 218 Oe. The saturation field is different for both cases. For $\alpha = 90°$, the saturation field is about 4 kOe, while it is only 2 kOe for $\alpha = 0°$.

Porous Ni nanowires embedded in an InP membrane

The Ni nanostructures embedded in an InP membrane are analyzed in the same way as the Ni nanoparticle / InP pore array composite. The resulting two hysteresis loops are depicted in Fig. 4.16 b). For $\alpha = 90°$ the hysteresis loop is very narrow. The remanence squareness is about 0.24 and the coercivity about 148 Oe. Compared to the $\boldsymbol{H} \perp \boldsymbol{z}$ case, the hysteresis loop in the $\boldsymbol{H} \parallel \boldsymbol{z}$ case is slightly narrower, as well as the remanence squareness (about 0.22) and the coercivity (about 92 Oe). The saturation field is quite different for both cases. For $\alpha = 90°$, the saturation field is about 9 kOe, while it is only 4 kOe for $\alpha = 0°$. Compared to the Ni particles embedded in an InP pore array,

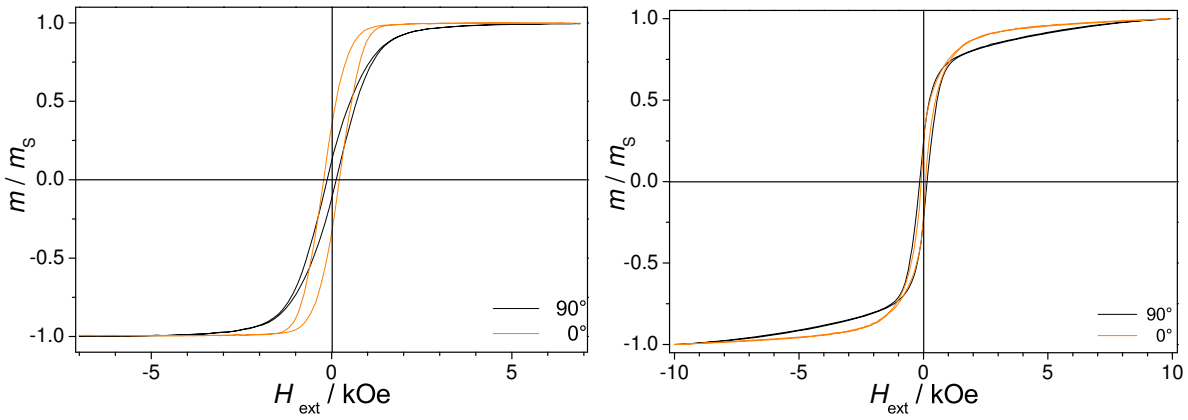

Figure 4.16: VSM measurement of the a) Ni particle / InP pore array composite and b) Ni particle, porous Ni nanowire / InP membrane composite. For both samples the hysteresis loops are measured with an external magnetic field parallel and perpendicular to the long pore axis.

the differences in the shape of the hysteresis loops and the magnetic properties between $\boldsymbol{H} \perp \boldsymbol{z}$ and $\boldsymbol{H} \parallel \boldsymbol{z}$ are less pronounced with only one exception, the saturation field.

Ni nanowires embedded in an InP membrane

The Ni nanowires embedded in the InP membrane are analyzed by angular dependent VSM measurements in two measurement arrangements. In the first arrangement, the hysteresis loops are measured with an external magnetic field applied perpendicular to the long axis $\boldsymbol{z}$ of the Ni nanowires ($\boldsymbol{H} \perp \boldsymbol{z}$) and rotated under various in-plane angles β from 0° to 90°. In the second arrangement, the hysteresis loops are recorded with an external magnetic field applied under various angles α between $\boldsymbol{H} \parallel \boldsymbol{z}$ and $\boldsymbol{H} \perp \boldsymbol{z}$. The resulting angular dependent hysteresis loop sets are depicted in Fig. 4.17 a) and b).

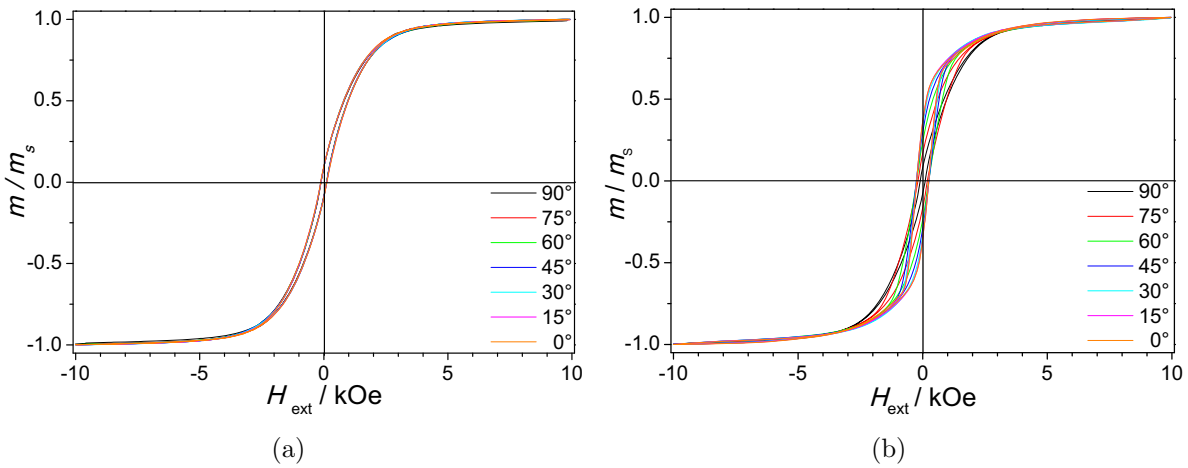

Figure 4.17: Angular dependent VSM measurement a) around $\boldsymbol{H} \perp \boldsymbol{z}$, and b) from $\boldsymbol{H} \parallel \boldsymbol{z}$ to $\boldsymbol{H} \perp \boldsymbol{z}$.

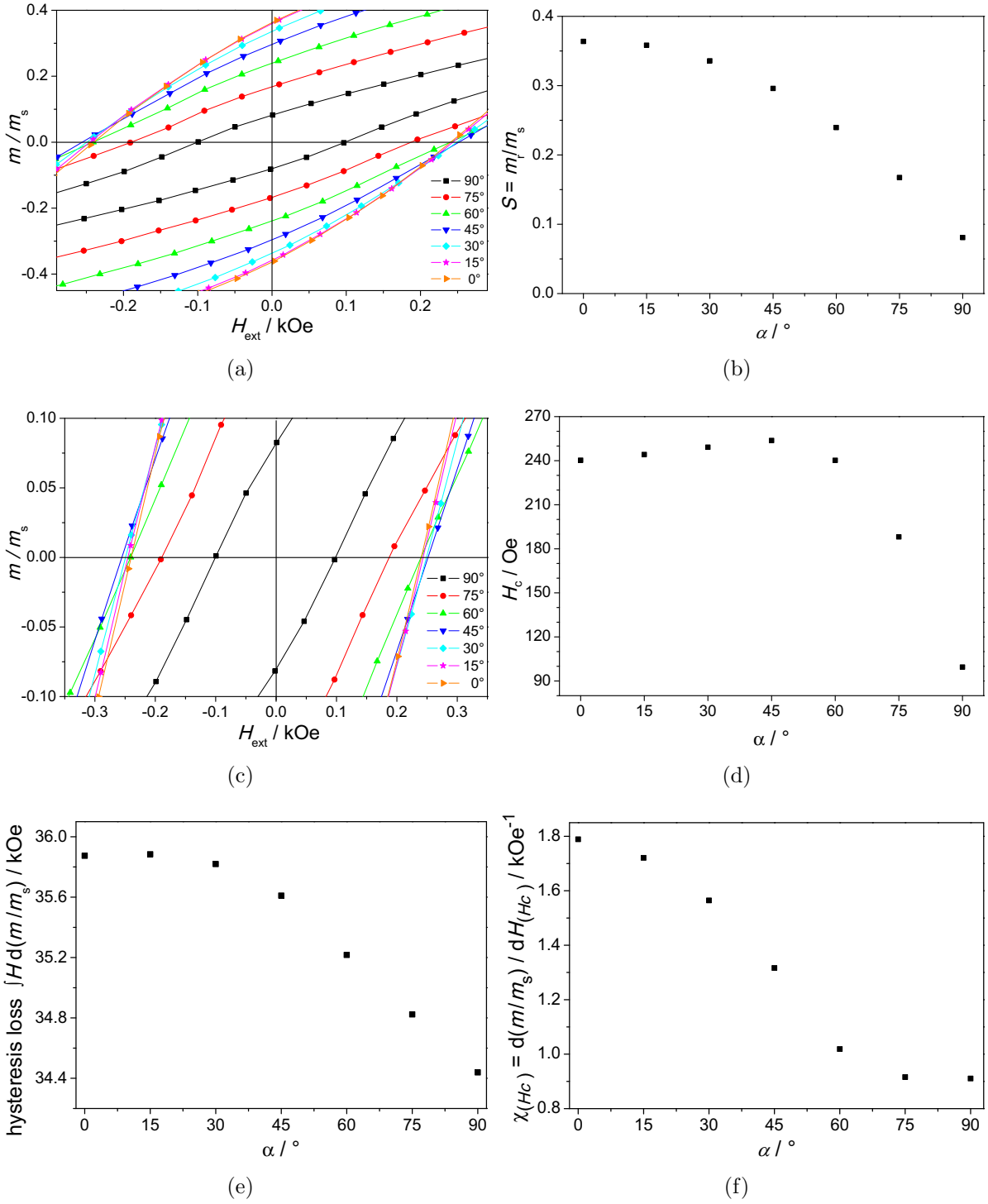

Figure 4.18: Magnetic properties of Ni nanowires embedded in InP membranes measured from $\boldsymbol{H} \parallel \boldsymbol{z}$ to $\boldsymbol{H} \perp \boldsymbol{z}$. a) High magnification of the normalized hysteresis loop near $H_{ext} = 0$ Oe, b) angular dependence of the remanence squareness S, c) high magnification of the normalized hysteresis loop near $m/m_S = 0$, d) angular dependence of the coercivity H_C, e) angular dependence of the hysteresis loss, and f) angular dependence of the slope $\mathrm{d}(m/m_S)/\mathrm{d}H$ at H_C.

Figure 4.17 a) shows distinctly that all hysteresis loops lay on top of each other when the external magnetic field is applied perpendicular to $\boldsymbol{z}$ and rotated around $\boldsymbol{z}$. Thus, no angular dependence of the hysteresis loops is found for various in-plane angles β. On the other hand a clear angular dependence of the hysteresis loops is found when the external magnetic field is varied from $\boldsymbol{H} \parallel \boldsymbol{z}$ to $\boldsymbol{H} \perp \boldsymbol{z}$, as depicted in Fig. 4.17 b). With increasing α a narrowing and a simultaneous tilting of the hysteresis loops is observed.

Figure 4.18 a) is the high magnification of the normalized hysteresis loops measured from $\boldsymbol{H} \parallel \boldsymbol{z}$ to $\boldsymbol{H} \perp \boldsymbol{z}$ near $H_{ext} = 0$ Oe. From these hysteresis loops the remanence squareness S is extracted, of which the angular dependence is depicted in Fig. 4.18 b). Looking first at the maximum and minimum value of the remanence squareness reveals the maximum value at $\alpha = 0°$ ($\boldsymbol{H} \parallel \boldsymbol{z}$) with about 0.36 and the minimum value at $\alpha = 90°$ ($\boldsymbol{H} \perp \boldsymbol{z}$) with 0.08. In between these two points, the remanence squareness curve slightly decreases from about 0.36 for $\alpha = 0°$ to 0.30 for $\alpha = 45°$. After $\alpha = 45°$, the remanence squareness drastically decreases down to 0.08 for $\alpha = 90°$. The derivative $\mathrm{d}S/\mathrm{d}\alpha$ giving the slope of the S *vs.* α curve shows an almost perfect straight line indicating that the remanence squareness shows a quadratic behavior with respect to the angle α between the external magnetic field $\boldsymbol{H}$and $\boldsymbol{z}$.

In Fig. 4.18 c) the high magnification of the normalized hysteresis loop near $m/m_{\mathrm{S}} = 0$ measured from $\boldsymbol{H} \parallel \boldsymbol{z}$ to $\boldsymbol{H} \perp \boldsymbol{z}$ is depicted. From these hysteresis loops the coercivity H_{C} is extracted, of which the angular dependence is shown in Fig. 4.18 d). The coercivity increases slightly from around 240 Oe for $\alpha = 0°$ ($\boldsymbol{H} \parallel \boldsymbol{z}$) and reaches its maximum value of around 254 Oe at $\alpha = 45°$. After $\alpha = 45°$ the coercivity curve strongly decays down to around 100 Oe for $\alpha = 90°$ ($\boldsymbol{H} \perp \boldsymbol{z}$).

The angular dependent hysteresis loss curve is depicted in Fig. 4.18 e). One can see that the angular behavior of the hysteresis losses shows a very similar behavior as found for the angular dependence of the remanence squareness. The maximum hysteresis loss is obtained along the long wire axis $\boldsymbol{z}$.

Figure 4.18 f) illustrates the angular dependence of the slope of the hysteresis loop at the coercivity. It is a quantitative measure for the tilting of the hysteresis loop. The maximum slope is 1.8 kOe^{-1} found at $\alpha = 0°$, the minimum slope 0.9 kOe^{-1}. Unlike for the remanence squareness and the hysteresis loss curves one observes here a change in the

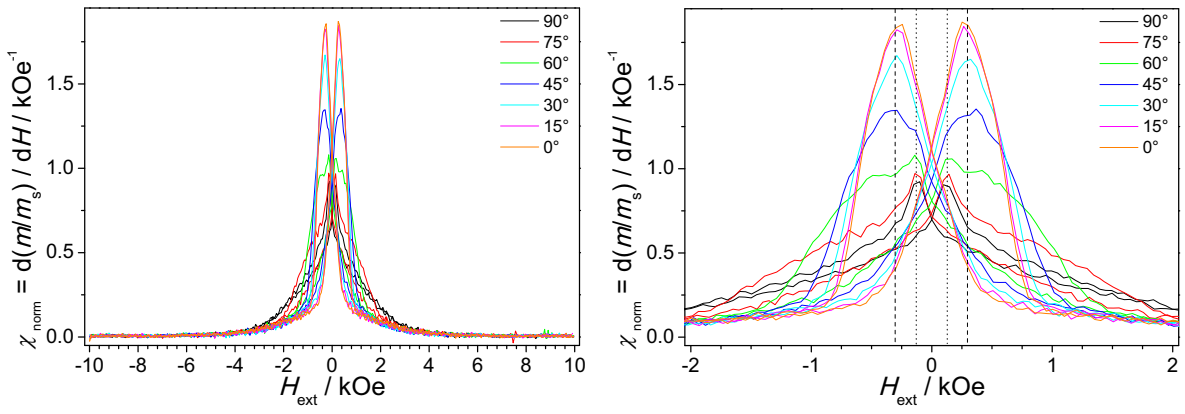

Figure 4.19: a) magnetic susceptibility of Ni nanowires embedded in InP membrane and b) in high magnification around $H_{\mathrm{ext}} = 0$.

slope of the curve at $\alpha = 45°$ as it is found for the angular behavior of the coercivity.

The magnetic susceptibility of the embedded Ni nanowires is depicted in Fig. 4.19. Figure 4.19 a) shows that the susceptibility calculated from the hysteresis loops for all hysteresis loops from $\alpha = 0°$ to $\alpha = 90°$ reaches zero at an external magnetic field of about 4.5 to 5 kOe. This means, hardly any angular dependence is found for the saturation field. As a tendency, the Ni nanowires reach saturation already at lower external magnetic fields for $\alpha = 0°$, while the saturation field slightly increases with increasing angle α. The magnified view on the susceptibility around $H = 0$ Oe given in Fig. 4.19 b) shows that there are two characteristic peak positions in the susceptibility represented by the vertical dotted and the dashed lines. The first peak is found around ±127 Oe (dotted line) and the second peak around ±300 Oe. In the susceptibility curve for $\alpha = 0°$ to $\alpha = 30°$ only one peak is present at ±300 Oe, while for $\alpha = 75°$ and $\alpha = 90°$ the single peak is positioned at ±127 Oe. The transition regime is found for $\alpha = 45°$ and $\alpha = 60°$ where contribution from both peaks are visible.

Fe-Co based nanowires embedded in an InP membrane

The Fe-Co based nanowires embedded in the single-crystalline InP membrane are analyzed by angular dependent VSM measurements as well. Since no angular dependence was found for the Ni nanowires with the external magnetic field applied around the long nanowire axis $\boldsymbol{z}$, the same behavior is expected for the Fe-Co based nanowires. Thus, the hysteresis loops for the Fe-Co based nanowires are recorded only with an external magnetic field applied under various angles α between $\boldsymbol{H} \parallel \boldsymbol{z}$ and $\boldsymbol{H} \perp \boldsymbol{z}$. The resulting angular dependent hysteresis loop set is depicted in Fig. 4.20.

One observes a very pronounced angular dependence of the hysteresis loops for the Fe-Co based nanowires, when the external magnetic field is varied from $\boldsymbol{H} \parallel \boldsymbol{z}$ to $\boldsymbol{H} \perp \boldsymbol{z}$. With increasing α a broadening and a simultaneous straightening of the hysteresis loops is observed.

Figure 4.21 a) is the high magnification of the normalized hysteresis loops measured from $\boldsymbol{H} \parallel \boldsymbol{z}$ to $\boldsymbol{H} \perp \boldsymbol{z}$ near $H_{\text{ext}} = 0$ Oe. From these hysteresis loops the remanence squareness S is extracted, of which the angular dependence is depicted in Fig. 4.21 b).

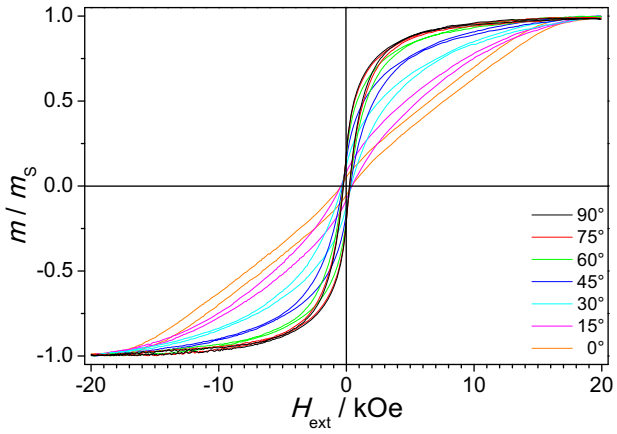

Figure 4.20: Angular dependent VSM measurement of the Fe-Co based nanowire / InP composite from $\boldsymbol{H} \parallel \boldsymbol{z}$ to $\boldsymbol{H} \perp \boldsymbol{z}$.

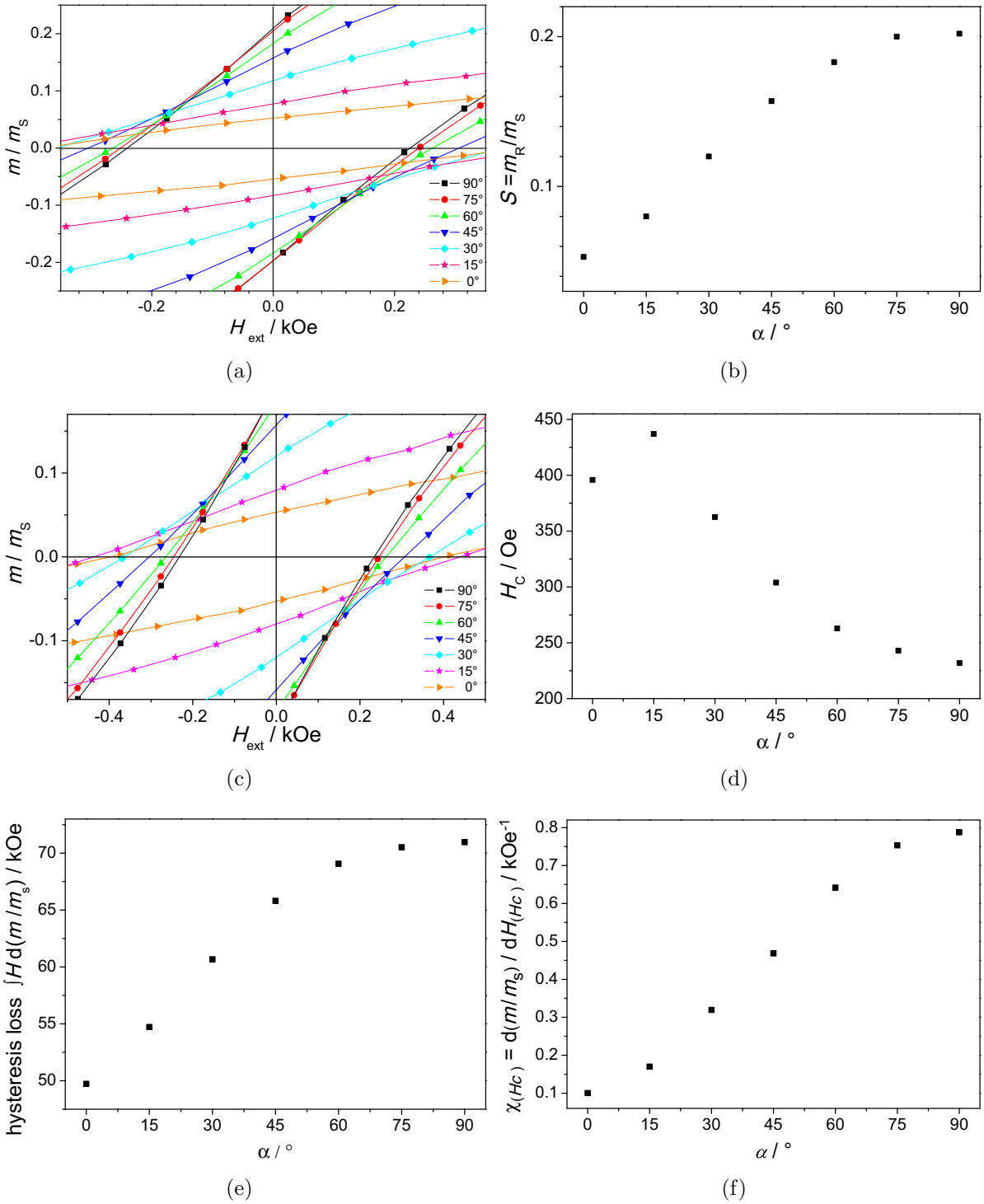

Figure 4.21: Magnetic properties of Fe-Co based nanowires embedded in InP membranes measured from $\boldsymbol{H} \parallel \boldsymbol{z}$ to $\boldsymbol{H} \perp \boldsymbol{z}$. a) High magnification of the normalized hysteresis loop near $H_{\mathrm{ext}} = 0$ Oe, b) angular dependence of the remanence squareness S, c) high magnification of the normalized hysteresis loop near $m/m_{\mathrm{S}} = 0$, d) angular dependence of the coercivity H_{C}, e) angular dependence of the hysteresis loss, and f) angular dependence of the slope $\mathrm{d}(m/m_{\mathrm{S}})/\mathrm{d}H$ at H_{C}.

Looking first at the maximum and minimum value of the remanence squareness reveals a maximum value of about 0.2 at $\alpha = 90°$ ($\boldsymbol{H} \perp \boldsymbol{z}$). The minimum value of the remanence squareness is found at $\alpha = 0°$ ($\boldsymbol{H} \parallel \boldsymbol{z}$) with about 0.05. In between these two points, the remanence squareness almost linearly increases from about 0.05 for $\alpha = 0°$ to about 0.18 for $\alpha = 60°$ with increasing angle α before it reaches a saturation starting from $\alpha = 60°$. After $\alpha = 60°$, the remanence squareness slightly increases to 0.20 for $\alpha = 90°$. The derivative $\mathrm{d}S/\mathrm{d}\alpha$ giving the slope of the S over α curve shows no straight line indicating that the remanence squareness shows a more complex relation with respect to the angle α between the external magnetic field $\boldsymbol{H}$and $\boldsymbol{z}$ compared to the Ni nanowires.

Figure 4.21 c) depicts the high magnification of the normalized hysteresis loop near $m/m_\mathrm{S} = 0$ measured from $\boldsymbol{H} \parallel \boldsymbol{z}$ to $\boldsymbol{H} \perp \boldsymbol{z}$. From these hysteresis loops the coercivity H_C is extracted. The angular dependence of the coercivity is presented in Fig. 4.21 d). All the measured coercivities are higher compared to the Ni nanowires without exception. The coercivity increases from about 396 Oe for $\alpha = 0°$ ($\boldsymbol{H} \perp \boldsymbol{z}$) to the maximum of around 437 Oe at $\alpha = 15°$. With further increasing angle α the coercivity curve strongly decays down to a saturation value of around 232 Oe for $\alpha = 90°$ ($\boldsymbol{H} \perp \boldsymbol{z}$).

The angular dependence of the hysteresis loss curve is presented in Fig. 4.21 e). The

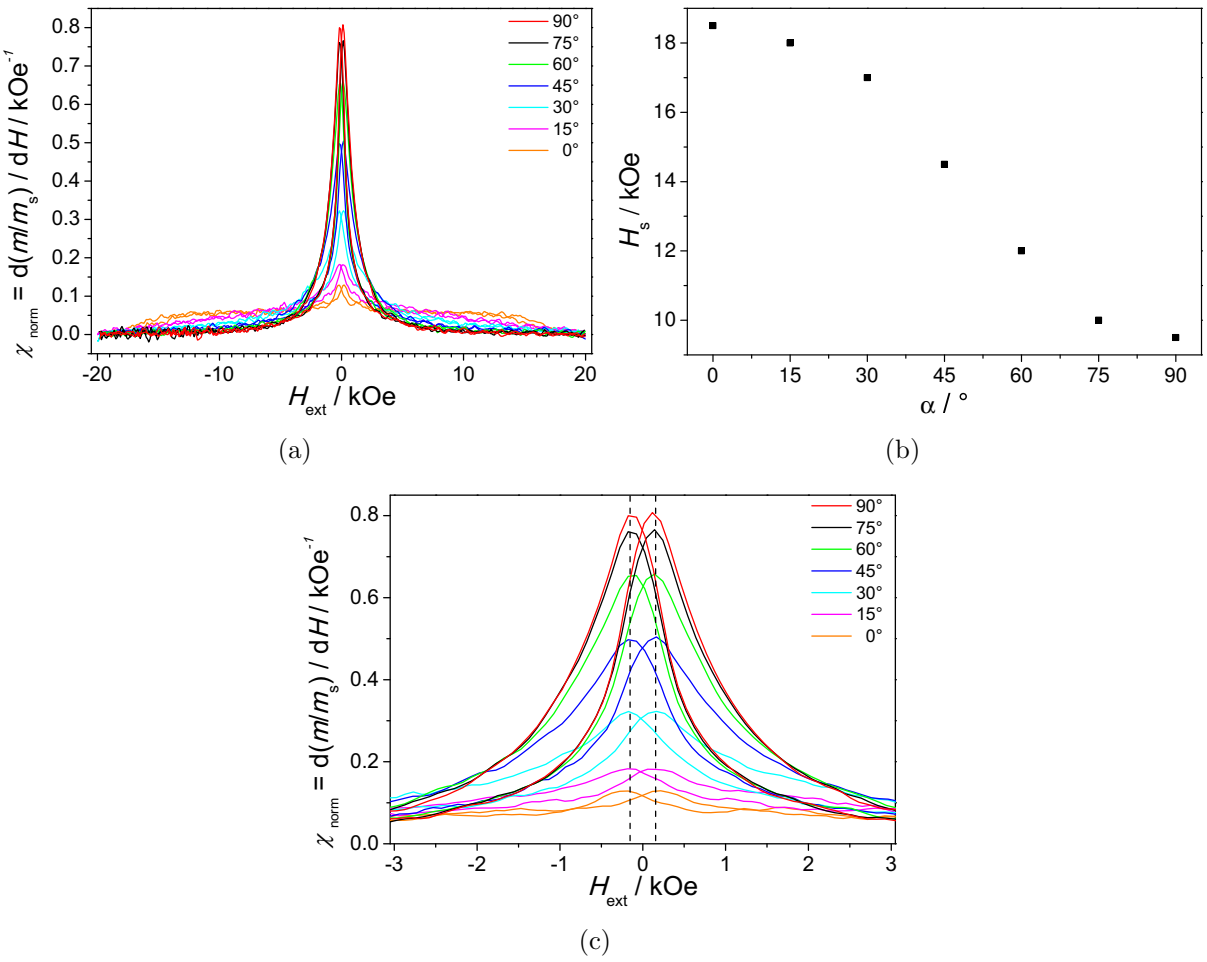

Figure 4.22: a) Magnetic susceptibility of Fe-Co based nanowires embedded in InP membrane, b) angular dependence of the saturation magnetization H_S, and c) high magnification of a) around $H_\mathrm{ext} = 0$.

hysteresis losses basically follow the trend of the remanence squareness. The maximum hysteresis loss is found along the easy magnetization direction, perpendicular to the long wire axis $\boldsymbol{z}$. Compared to the Ni nanowires, the Fe-Co based nanowires exhibit a much broader hysteresis loop and thus, higher hysteresis losses. Also the difference in the hysteresis losses for different angles α is far more pronounced.

Figure 4.21 f) depicts the angular dependence of the slope of the hysteresis loop at the coercivity. The maximum slope is about 0.8 kOe^{-1} found at $\alpha = 90°$ and the minimum slope with about 0.1 kOe^{-1}. The shape of the slope is similar to a stretched S with only small changes around $\alpha = 0°$ and $\alpha = 90°$. Compared to the slope of the hysteresis loops of the Ni nanowires, the Fe-Co based nanowires exhibit significantly smaller slopes at the coercivity. On the other hand, the dynamics in the slopes from $\alpha = 0°$ to $\alpha = 90°$ are far more pronounced for the Fe-Co based nanowires.

The magnetic susceptibility of the embedded Fe-Co based nanowires calculated for all hysteresis loops from $\alpha = 0°$ to $\alpha = 90°$ is depicted in Fig. 4.22 a). The maximum susceptibilities of the Fe-Co based nanowires are always lower compared to the maximum susceptibility values of the Ni nanowires, which is also found for the slope of the hysteresis loop at H_C.

The angular dependence of the saturation field of the Fe-Co based nanowires is presented in Fig. 4.22 b). The shape of the curve is like a mirrored S, nearly identical in shape to the angular dependence of the hysteresis loop slope at H_C. The saturation field changes only slightly around $\alpha = 0°$ and $\alpha = 90°$ and much stronger for angles between 0° and 90°. The minimum saturation field is about 9.5 kOe for $\alpha = 90°$, the maximum is about 18.5 kOe for $\alpha = 0°$. These saturation fields are at least a factor of two higher (maximum: factor of 4, depending on the angle of the applied magnetic field) compared to the Ni nanowires. Unlike for the Ni nanowires, the magnified view on the susceptibility around $H = 0$ Oe given in Fig. 4.22 c) only shows a single characteristic peak position at about 130 Oe represented by the vertical dashed line.

4.3.3 FFT-IS of the galvanic growth of Ni nanowires

The impedance data were recorded for the galvanic growth of Ni nanowires in an Al_2O_3 coated membrane as stated in the experimental chapter in section 3.5.4. All impedance data could be very well fitted by using an elevated fit model consisting of a resistor R_s which is connected in series with an RC element (parallel arrangement of the resistor R_p and the capacitor C_p). The capacitor C_p itself does not appear as a single fit parameter, but is incorporated in the time constant $\tau_\mathrm{p} = R_\mathrm{p}C_\mathrm{p}$. A maxwell element consisting of the parallel arrangement of the resistor R_a, the capacitor C_a, and the series connection of R_b and C_b is completing the electric equivalent circuit that is depicted in Fig. 4.23 b). This fit model allowed for the most consistent explanation of the results as discussed in section 5.2.2.

Figure 4.23 a) presents the typical Nyquist plot of the impedance data of the galvanic Ni deposition process. The small boxes are the measured data, while the black line is the result of the fitting with the model described above. Figure 4.23 a) illustrates clearly the high quality and stability of the used fitting model. The impedance is recorded for 26 different frequencies from 75 Hz up to about 18 kHz.

The time dependence of the measured deposition potential U and the seven fit parameters, the series resistance R_s, the transfer resistance R_p, the time constant τ_p, and the

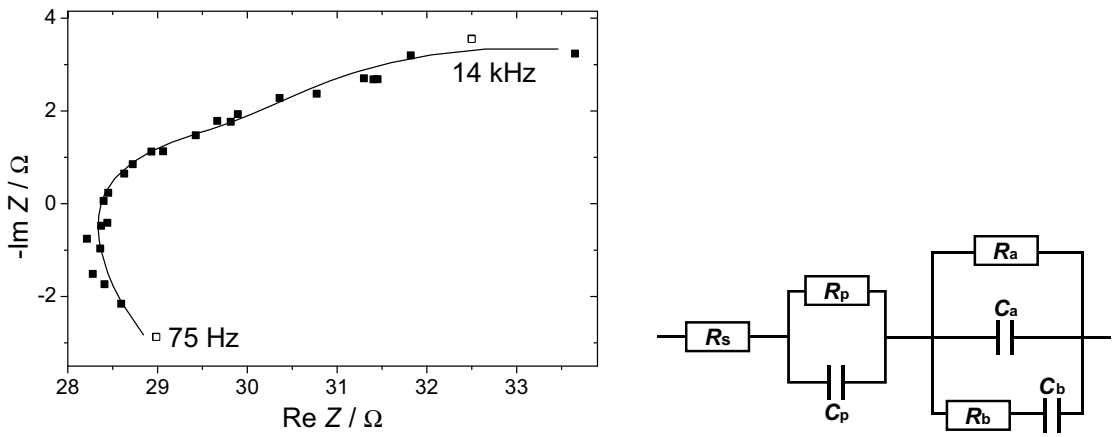

(a) (b)

Figure 4.23: a) Typical Nyquist plot of the FFT-IS measurement during the galvanic growth of Ni nanowires in InP membranes. The small boxes are the measured data. The black line is the fit. The corresponding frequencies are given next to the boxes. b) Corresponding electric equivalent circuit.

resistances of the Maxwell element R_a, R_b and the corresponding capacities C_a, C_b during the galvanic growth of Ni nanowires inside the Al_2O_3 coated InP membrane are shown in Fig. 4.24. Within the first seconds of the deposition, strong changes are observed in most of the fitting parameters and the deposition voltage. The deposition voltage U, τ_p, C_a, and R_b increase, while R_s and C_b decrease, R_p and R_a are unaffected.

The deposition potential U increases in the first seconds from about -0.6 V to about -0.8 V. In the following it varies about -0.75 V. After about 10 min, 30 min, and around 55 min the deposition voltage shows minor peaks.

The series resistance shows a constant base level of about 30 Ω with three characteristic peaks at about 10 min, 30 min, and around 55 min. At these three positions the series resistance is increasing almost linearly from about 30 Ω to about 60 Ω before decreasing abruptly down to the base level again. In the part between two major peaks, one to two minor peaks can be detected. All these peaks coincide with slight changes in the deposition voltage U.

The transfer resistance R_p stays negative over the entire deposition time. It constantly increases starting from about -10 Ω up to about -25 Ω. Towards the end of deposition time, the oscillations in R_p become more pronounced compared to the behavior before.

The associated time constant τ_p is positive over the entire deposition time unlike the transfer resistance R_p. After an initial decay from about 3 μs down to 2.3 μs within the first two minutes, τ_p decreases linearly to about 1 μs. In contrast to R_p the oscillations in τ_p stay rather constant over the complete deposition time.

The time dependence of the Maxwell elements C_a, R_b, and C_b can be subdivided into three sections. Section I comprises the first six minutes, section II ranges from 6 min to about 36 min, and section III starts from about 36 min till the end of deposition. The time dependence of each of the four parameters is described in more detail in the following. These three characteristic sections are not observed in the deposition voltage U, series resistance R_s, and transfer resistance R_p, only to some extent in the Maxwell R_a and the time constant τ_p.

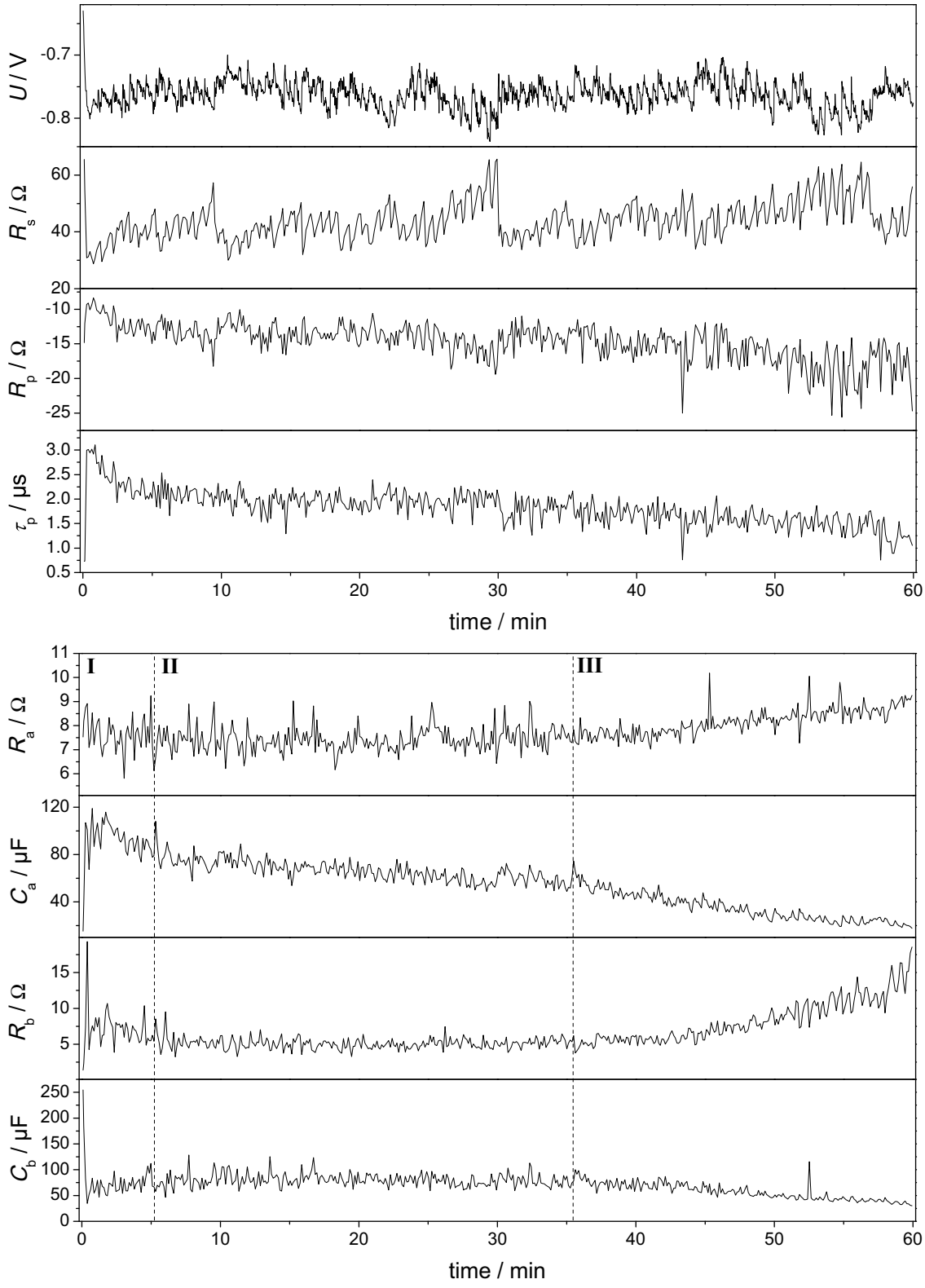

Figure 4.24: Deposition voltage U and the fit parameters: the series resistance R_s, transfer resistance R_p, the corresponding time constant τ_p and the Maxwell element with R_a, C_a, R_b and C_b as a function of the deposition time at a constant current density of 17 mA/cm^2.

The Maxwell resistance R_a is nearly constant over the deposition time alternating around 8 Ω. After about 36 min R_a shows the tendency to slightly increase linearly till the end of deposition up to a resistance of about 9 Ω.

The associated Maxwell capacity C_a decreases linearly with different slopes from about 120 μF down to approximately 20 μF over the deposition time. In section I, C_a decreases stronger compared to section II. In section III the slope increases slightly again. Looking at the oscillations of C_a, one observes that the amplitudes of the oscillations are strong in section I, but drastically abate in section II and III.

The Maxwell resistance R_b is rather constant for about 36 min. After 36 min till the end of deposition, R_b keeps increasing up to a resistance of about 15 Ω. In the first and last seven minutes of the deposition, the amplitudes of the oscillations are more pronounced compared to the time in between.

After a strong decline in the associated capacity C_b from about 250 μF to about 60 μF in the first seconds, C_b shows an increasing trend up to about 90 μF in section I, a rather constant behavior in section II, and continuous decrease to about 30 μF in section III. The oscillations are more pronounced in the beginning and decline with time. At about 53 min a sharp and high peak in C_b is observed.

4.4 Porous InP membranes as anode in Li-ion batteries

4.4.1 Anode fabrication

The porous InP anode is fabricated in the same way as described in section 4.1 including the post-etching process under cathodic bias. The final pore structure of the porous InP anode is depicted in Fig. 4.25.

Figure 4.25 a) gives a cross sectional view on the porous membrane. The curro-pores were grown perfectly straight over the entire pore length of about 390 µm. Due to the membrane fabrication the thickness of the membrane is reduced to approximately 340 µm resulting in an aspect ratio of about 2100:1 for the anode.

The curro-pores have a highly rectangular cross-sectional shape as shown in Fig. 4.25 b) and an almost equi-distant arrangement in a nearly perfect hexagonally close-packed structure. After the cathodic post-etching at −0.5 V for 48 h the mean pore wall width is reduced from 220 nm to about 160 nm to account for the volume expansion during lithiation, but leaving enough InP for the Li uptake.

The figures 4.25 c) and d) present the porous InP anode after the final process step. The front side of the circular anode is completely covered by an Au layer with a thickness of approximately 450 nm. This Au layer serves as current collector for the external electric contacting of the anode. Afterwards, the porous anode is freed from the surrounding bulk InP, [see Fig. 4.25 c)].

The back side of the anode – depicted in Fig. 4.25 d) – is the active part of the anode. Although being completely porous and free-standing, the anode shows a high mechanical stability, which makes the handling easy. The previously surrounding bulk InP was completely removed, because bulk InP would induce mechanical stress during cycling and would pulverize due to the volume expansion and thus, destroy the entire anode.

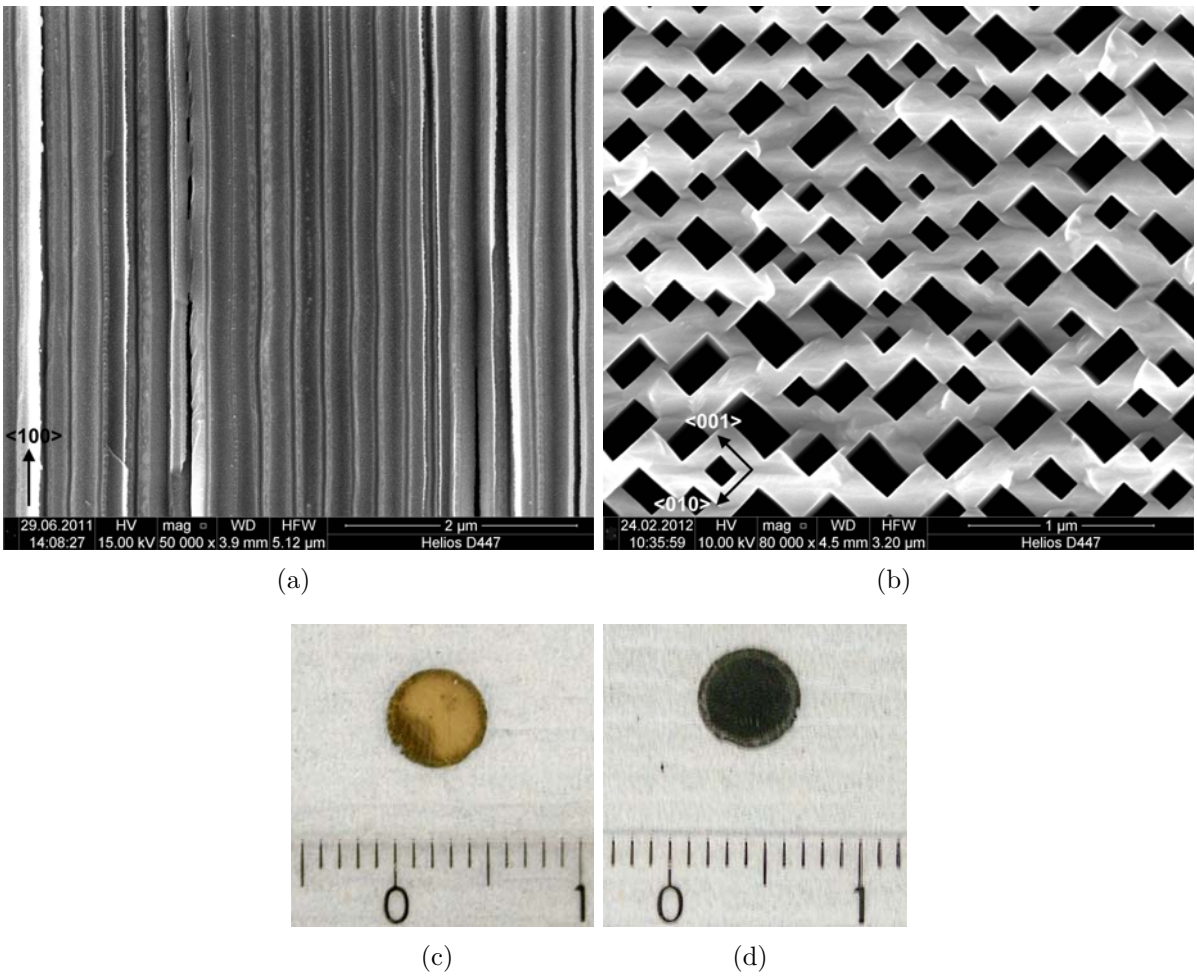

(a) (b)

(c) (d)

Figure 4.25: Porous InP membrane anode before first lithiation: a) magnified cross-sectional SEM view on the (110) plane of the InP pore array and b) top view on the membrane back side after cathodic post-etching. The vectors indicate the pore orientation. Optical microscopy images of c) the Au contacted front side and d) the open back side of the finally processed anode. The visible scale is 1 cm.

4.4.2 Structural analysis of the InP anode

The InP anode in the lithiated state

Figure 4.26 presents SEM images of the porous InP anode after being charged to 1.85 V. Prior to the SEM investigation, the anode was dismantled from the half-cell in a glove box under an Ar atmosphere to prevent the oxidation of the anode. Figure 4.26 a) gives a top view on the surface of the anode showing mostly geometric cracks preferentially in $\langle 110 \rangle$ direction being the natural fracture direction for InP. The origin of these cracks is most probably the sample handling during the disassembling of the anode from the half-cell or the mounting of the anode on the sample holder for the SEM investigation. The randomly distributed white fibers on top of the anode stem from the glass fiber microfilter that was used as separator material and are not detached InP pore walls.

The microstructure of the anode surface in the lithiated state is presented in Fig. 4.26 b). The hexagonally, almost perfectly close-packed pore structure of the unlithiated

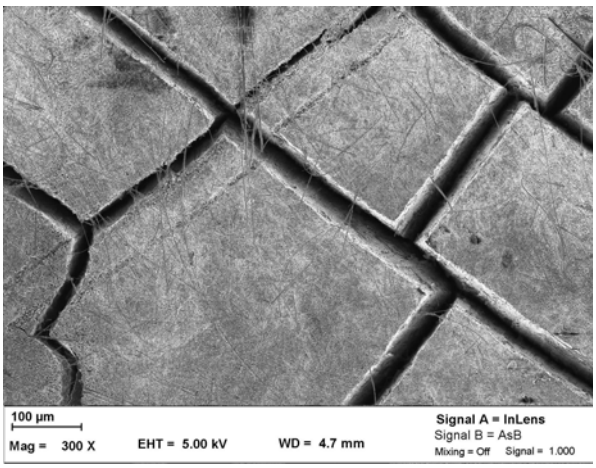

(a)

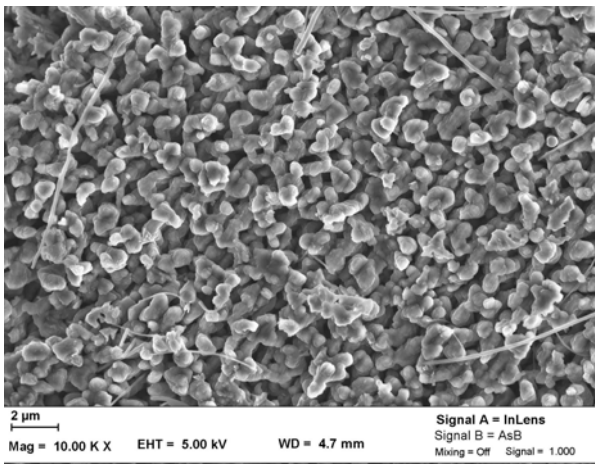

(b)

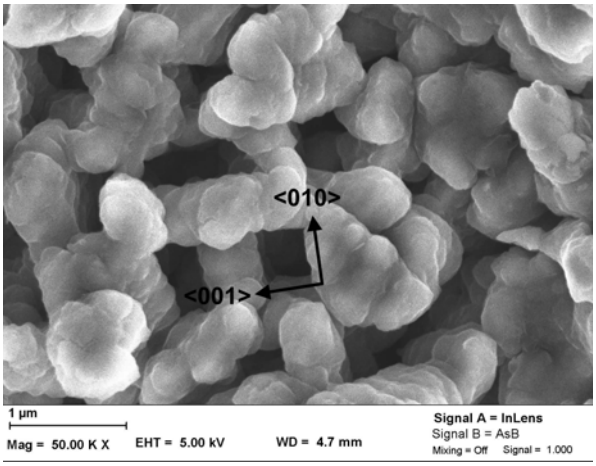

(c)

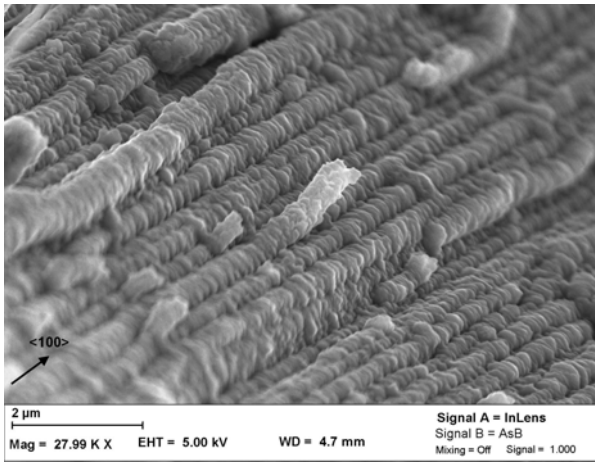

(d)

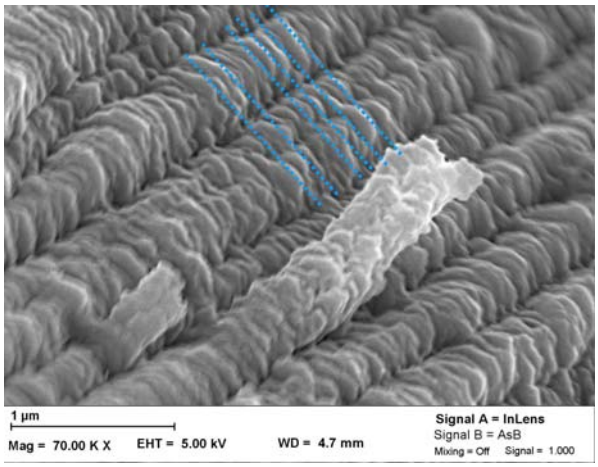

(e)

Figure 4.26: Top view on the (100) plane of the porous InP anode after complete lithiation showing a) the macroscopic surface, b) the microscopic surface texture, and c) the sub-micron surface texture; d) cross-sectional view on the (110) plane of the InP anode near to the surface, e) high magnification image at the same position. The dotted lines (blue) indicate the anti-phase faceting of the pore walls. The vectors indicate the pore orientation.

anode – as depicted in Fig. 4.25 b) – is barely maintained. Due to the lithiation the InP pore walls enlarged drastically in width, so that hardly any free space is left. Nevertheless, small areas on the surface can be identified where the pore structure of the unlithiated anode is maintained. Figure 4.26 c) gives a highly magnified view on such an area also depicting the sub-micron texture of the lithiated pore walls. In the left half of the image, one can still clearly identify the pore arrangement before lithiation, while the pore arrangement is basically lost in the surrounding, as seen on the right half of the image. This behavior could be explained e.g. by slight local variations in the pore wall width. This means, the volume increase of the InP due to the incorporation of Li into the InP crystal structure can be compensated and the porous structure can be maintained if the pore wall width in the unlithiated state is small enough. If this pore wall width exceeds a critical width, the pore walls can preferentially fracture at the corners of the pores due to the strong volume expansion on lithiation, especially at positions where two corners of neighboring pores meet.

The observed faceting of the lithiated pore walls being not an exclusive feature of the areas without maintained pore structure, but also occuring in areas with maintained pore structure. A closer look on these facets, as illustrated in Fig. 4.26 d), reveals the faceting is not limited to the surface, but also occurs over the entire length of the pore walls.

In addition, the facets can be identified as a repeating, regular sequence of bulging and necking of the pore walls. This oscillation in the pore wall width is self-induced and in anti-phase to the neighboring pore walls, as shown in Fig. 4.26 e). The area with the dotted blue lines is randomly chosen as example for the anti-phase bulging and necking of neighboring pore walls.

The InP anode in the delithiated state

Figure 4.27 shows the porous InP anode after charging to 1.85 V and subsequent discharge to 0.15 V. The anode was dismantled from the half-cell under an Ar atmosphere. The top view on the surface of the discharged anode given in Fig. 4.27 a) reveals an almost complete covering of the pore walls with the already formed solid–electrolyte interface (SEI) layer. The black dimples visible on the surface, especially in the middle of Fig. 4.27 a), are pore openings. Also the top parts of pore walls can be easily identified.

In general, the surface is in good mechanical condition after lithiation and delithiation, since no blow-out or big craters are detectable on the surface.

Figure 4.27 b) illustrates the surface-near part of the anode in cross-section. No delaminations or pulverizations of the pore walls can be identified, i.e. according to the SEM images the pore structure is maintained. The pore walls in cross-section are also partially covered by the SEI layer similar to the surface of the discharged anode. The highly magnified view on the anode in cross-section in Fig. 4.27 c) exhibits the sustain of the anti-phase oscillations in the pore wall width as exemplarily represented by the dotted blue lines, but the oscillations of the pore wall width are far less pronounced compared to the lithiated anode from Fig. 4.26 e). This reduction is the direct consequence of discharging the anode and thus, removing Li-ions from the InP pore walls. Nevertheless, the pore wall width of the discharged anode remains highly increased compared to the mean pore wall width of about 160 nm of the unlithiated InP pore structure. This is a clear sign for an irreversible structure change in the InP pore walls, which is most probably induced by the permanent incorporation of Li into amorphous InP structure.

The dotted orange lines represent the original curro-pores. The pore walls in the middle of the anode shown in Fig 4.27 d) also show oscillations in the pore wall width, but again strongly reduced compared to the lithiated state. In contrast to the surface-near part of the discharged anode bright particles in the lower nanometer range are found lying on the pore walls. Most probably these particles are LiF and originate from the reaction of Li-ions that were extracted from the anode and F^- ions from a reduction of the battery electrolyte during the delithiation process of the anode. A detachment of InP from the pore walls cannot be completely excluded, but this is unlikely since no break-out could be found in the pore walls. The detachment of InP from the anode would be directly associated to a loss in the anode capacity, because the detached InP would not be in electric contact to the anode and thus, not charged and discharged during further cycling.

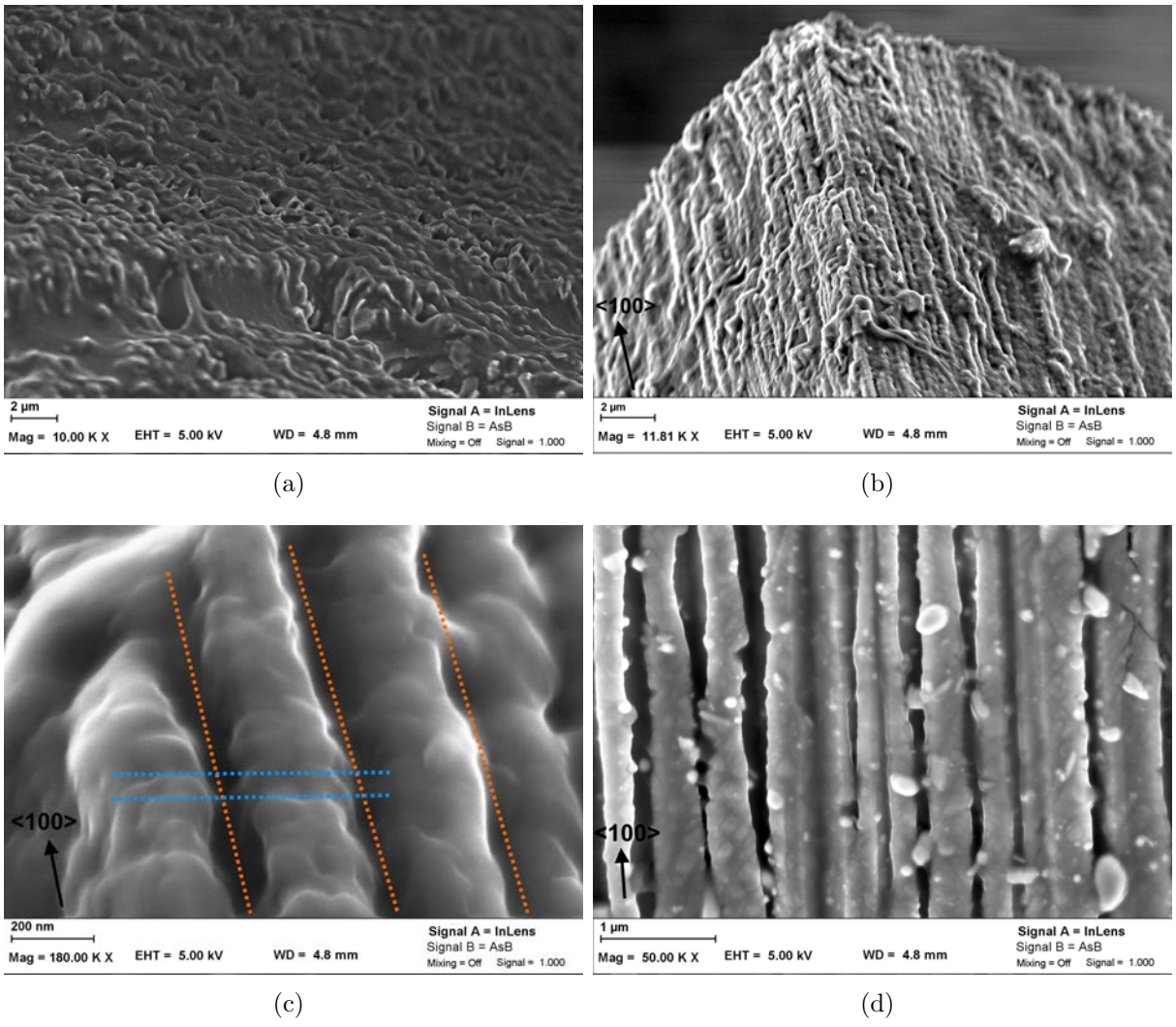

Figure 4.27: a) Top view on the (100) plane of the porous InP anode after complete delithiation, b) cross-sectional view on the (110) plane of the anode near the surface, c) high magnification of the same area, and d) in the middle of the anode. The dotted horizontal lines (blue) indicate the maintained anti-phase faceting of the pore walls. The dotted lines (orange) show the curro-pores. The vectors indicate the pore orientation.

XRD analysis of the lithiated and delithiated anode

For the XRD characterization three porous InP anodes are chosen, one unlithiated, one being charged to 1.85 V, and one being charged to 1.85 V and subsequently discharged to 0.15 V. The unlithiated InP anode is used as reference sample exhibiting only a very sharp (200) InP peak as presented in Fig. 4.4 f).

The diffraction pattern of the lithiated anode is depicted in Fig. 4.28 a). It shows three distinct broad peaks and one blurry peak with low intensity. None of them can be assigned to crystalline InP, In, or P. This indicates that the mean pore wall width of the anode is small enough to allow Li ions to diffuse into the entire pore wall and to convert the InP completely into Li alloys.

According to the XRD data on Li-In alloys published by Stöhr [83], two of the peaks can be consistently assigned to In_3Li_{13}, namely In_3Li_{13} {422} and In_3Li_{13} {531}. The other two peaks are identified as LiP [84], namely LiP {200} and LiP $\{22\bar{3}\}$. Besides the above mentioned Li alloys other Li phases might be present in the lithiated state, but could not be identified by XRD measurements.

The XRD pattern of the lithiated and subsequently delithiated InP anode is presented in Fig. 4.28 b). A single distinct and broad peak and three small, blurred peaks are visible. None of these peaks matches with the peaks found in the previously shown XRD pattern of the lithiated anode. All four peaks can be assigned to InP including the distinct peak, namely InP {111}, InP {200}, InP {220}, and InP {311}.

This result clearly shows the reversibility of the lithiation process in InP in contrast to other metal phosphides, such as CoP_3 [85] or Sn_4P_3 [86] where the lithiation process is not completely reversible. Besides the four InP peaks also two blurry peaks with low intensity are observed, marked with an asterisk. These two peaks cannot be assigned unambiguously to crystalline phases of the elements present in the anode, however it cannot be excluded that they originate from remaining Li-In or Li-P phases, or mixtures of these.

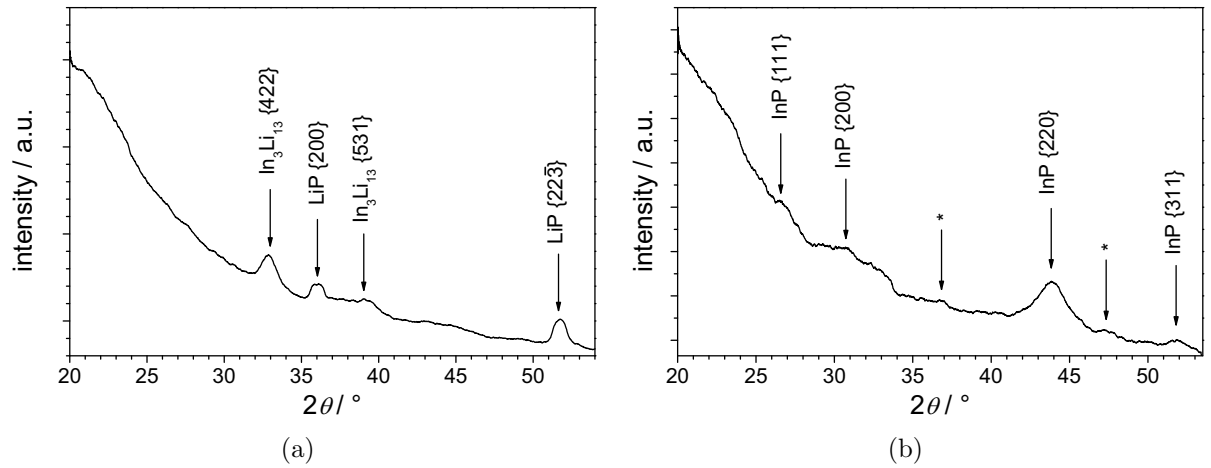

Figure 4.28: XRD pattern of the porous InP anode being a) lithiated to 1.85 V and b) lithiated to 1.85 V and subsequently delithiated to 0.15 V.

4.4.3 Electrochemical analysis of the porous InP anode

Voltammetry

The results of the cyclic voltammetry and the constant current charging are presented in Fig. 4.29. For the cyclic voltammograms the current is plotted over the potential *vs.* Li^+/Li and not over the cell potential. The negative voltage sweep is the bottom half of the curve. It is related to the lithation of the anode. The positive voltage sweep is the top part of the curve and represents the delithiation of the anode.

The first lithiation and delithiation cycle of the porous InP anode is depicted in Fig. 4.29 a). During the first lithiation of the anode two peaks are observed at 0.54 V and 0.36 V – from higher to lower potentials. For the first delithiation three peaks are observed at 0.76 V, 0.92 V, and 1.3 V. As shown in Fig. 4.29 b), most of the observed peaks are slightly shifted in subsequent cycles. Besides these minor shifts also the peak at 1.3 V is widely shifted to about 1.7 V. During the negative voltage sweep a new peak evolves in the second cycle at about 0.9 V and disappears again in the fifth cycle. From these cyclic voltammograms the operation range of the anode can be obtained. Below 0.15 V and above 1.85 V no peaks or other events are found in the cyclic voltammograms. Thus, the operation range of the anode is between 0.15 V and 1.85 V.

Since the XRD analysis of the porous InP anode is only performed for fully charged and fully charged and subsequently fully discharged anodes, but not at different stages in between, the peaks in the voltammograms are compared to literature values of InP cyclic voltammograms where additional XRD measurements were performed.

Especially in the first cycle, but to some extent also in the second cycle the current decreases quickly during the negative voltage sweep in the voltage regime below 0.25 V – see Fig. 4.29 a) and b). This feature is commonly found mostly in the first cycles of anodes that contain Au to some extent [87, 88]. As possible explanation the authors in [88] suggested that at low voltages and low sweep rates a formation a Li-Au alloy ($LiAu_3$) occurs. This process is irreversible and kinetically limited which would also explain, why the fast current decrease is observed only for the first two cycles for the porous InP anode.

In the diffraction pattern of an InP anode that was charged up to 0.5 V in the first negative voltage sweep peaks assigned to a crystalline In-Li alloy have been found [89]. The XRD analysis of an anode previously charged to 0.5 V and subsequently discharged to 0.67 V reveals the formation of In. Additionally in [32] the charge-discharge curves of an InP thin film anode exhibit a vast plateau at 0.3 V during lithiation and a huge plateau at around 0.75 V during delithiation. Based on the XRD results of the porous anode presented in Fig. 4.28 a) and these two publications [32, 89], the peaks in the cyclic voltammograms of the porous InP anode occurring around 0.35V and around 0.8 V can be attributed to the redox-couple of In_3Li_{13} / In at ∼0.35 V / ∼0.8 V.

In publications on InP anodes [32, 33, 89], a crystalline Li-P phase could not be found in the performed XRD data. By x-ray photoelectron spectroscopy the existance of Li_3P could be detected for completely lithiated InP anodes [33]. Moving to the lithiation of orthorhombic black phosphor reveals the formation of LiP in the voltage regime between 0.6 V and 0.8 V [90] identified by electron diffraction. In cyclic voltammograms of Ni_2P a pronounced peak at around 0.5 V was found during lithiation [31]. In this metal phosphide, Ni is not lithiated. It acts as a spectator atom not taking part in the reaction. For the delithiation of Ni_2P a peak in the cyclic voltammograms is observed at about 1 V. Based on the XRD results of the porous anode [Fig. 4.28 a)] and these publications, the

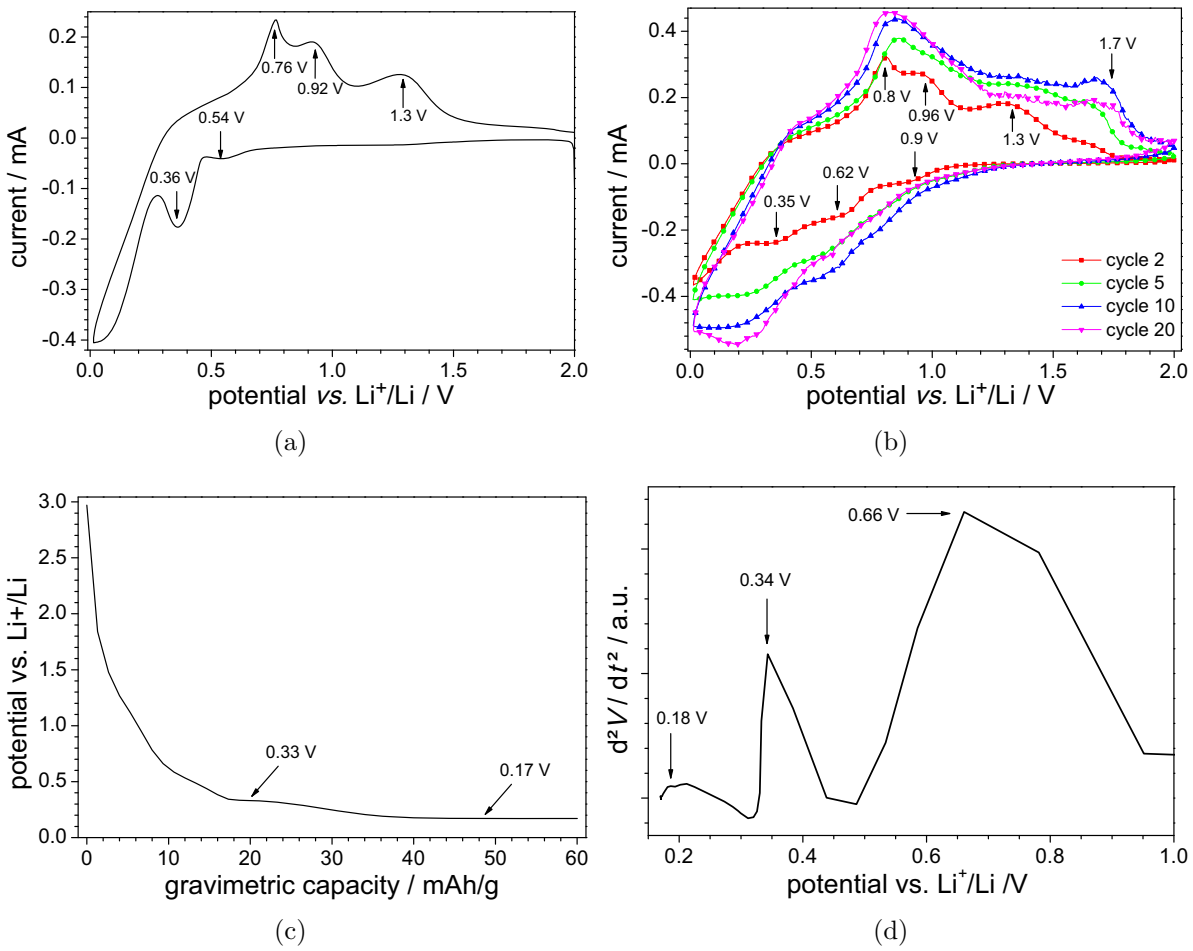

Figure 4.29: Cyclic voltammogram of the porous InP anode of the a) first cycle and b) selected cycles starting from cycle 2 till cycle 20, cycled between 0 V and 2 V with a scan rate of 0.1 mV/s. c) voltage *vs.* gravimetric capacity, lithiated at $C/10$ till 10 mV is reached, d) 2nd derivative of the voltage *vs.* time curve.

peaks in the cyclic voltammograms of the porous InP anode occurring around 0.62 V and around 0.96 V can probably be attributed to the redox-couple of LiP / P at ∼0.62 V / ∼0.96 V.

At about 1.5 V a plateau region in cyclic voltammograms was observed in the existing publications on InP anodes [32, 33, 89]. The XRD pattern of an InP anode previously charged to 0.5 V and directly discharged to around 1.36 V in the first negative voltage sweep shows certain peaks that are associated to crystalline InP. The results of these publications combined with the XRD analysis of the delithiated porous InP anode allows to assign the peak at 1.3 V to the formation of polycrystalline InP. The shift of the peak associated to the formation of InP at 1.3 V to 1.7 V has not been reported for any InP anode before. The shift could be the result of an alternative reaction pathway for the formation of InP by a single substitution of remaining LiP with In to form InP. Mechanical stresses in the anode could impede the full delithiation process – see the increase of the peak with increasing number of cycles in Fig. 4.29 b) – and thus, enable the alternative reaction pathway to form InP.

The peak at about 0.8 V in the cyclic voltammograms in [32] was attributed to the

formation of an SEI layer covering the InP anode. Based on this and the observation of an SEI layer covering the pore walls of the porous InP anode – as presented in Fig. 4.27 a) and b) – the peak present at 0.9 V till the fifth cycle can probably be related to the formation of an SEI layer for porous InP anodes. The cyclic voltammograms in Fig. 4.29 b) also show that this process is irreversible, since no corresponding peak is evolving during the delithiation.

To confirm the findings of the cyclic voltammograms constant charging experiments of the anode are performed. The porous InP anode is lithiated with a constant current of $C/10$ until a potential *vs.* Li/Li^+ of 10 mV is reached. The resulting potential *vs.* capacity curve is presented in Fig. 4.29 c). Two plateau regions are identified – a small plateau at 0.33 V and a vast platau at 0.17 V. In Fig. 4.29 d) the second derivative of the potential *vs.* time is depicted exhibiting three peaks at about 0.18 V, 0.34 V, and 0.66 V. The first two peaks in the second derivative of the potential *vs.* time are consistent with the plateau regions in the potential *vs.* capacity shown in Fig. 4.29 c). The peak at 0.18 V, respectively the plateau at 0.17 V can be associated to the formation of the Li-Au alloy. The other two peaks in the second derivative of the potential *vs.* time curve are in very good agreement with the peak positions obtained from the cyclic voltammograms 4.29 b) being associated to the lithiation of In and P, respectively. These results show that the cyclic voltammograms are performed at a quasi-static condition.

Standard battery cycling tests

The maximum gravimetric capacity of InP as anode in Li-ion batteries is widely spread. In the literature, gravimetric capacities range from 780 mAh/g [33] up to around 1100 mAh/g [32, 89]. The maximum capacity of the porous InP anode is determined by potentiostatic charging at 0.15 V. The resulting gravimetric capacity *vs.* charging time curve is presented in Fig. 4.30. The gravimetric capacity of the porous InP anode is estimated to be about 800 mAh/g, the maximum gravimetric energy density is 1.36 Wh/g, and the capacity per area related to this is about 63.5 mAh/cm^2. The half cell potential is 1.7 V with a lower voltage limit of 0.15 V and an upper voltage limit of 1.85 V.

As described in section 3.6, the battery is charged to the maximum gravimetric capacity of 800 mAh/g in the first cycle and discharged to 20 % of the maximum gravimetric capacity. In the following charging cycles the anode is charged to 80 % of its maximum gravimetric capacity (640 mAh/g) and discharged till the voltage limit of 0.15 V is reached. The gravimetric capacity is reduced to 80 % of its maximum value after the first cycle to retain always a certain amount of Li in the InP structure in order to minimize mechanical stress in the anode structure caused by phase transitions. This charging strategy shows very promising results for Si microwire anodes [91].

Figure 4.30 b) shows the maximum gravimetric capacity is reached in the first cycle and 640 mAh/g is reached in the following six cycles, which was set as maximum capacity in the charging program. After the seventh cycle a strong fading decreasing almost linearly from 640 mAh/g down to 275 mAh/g in the 13^{th} is observed. The delithiation curve is always well below the lithiation curve, except for the second cycle. This indicates a rather bad Coulomb efficiency, which is depicted in Fig. 4.30 c). The Coulomb efficiency of the first cycle is only at 80 % because during the first delithation the anode was discharged to only 20 % of maximum gravimetric capacity. The second cycle shows a Coulomb efficiency of about 99 %. For the following cycles the Coulomb efficiency is rather constant, slightly

alternating around an average value of about 85 %.

The trend of irreversible losses and the fading with increasing cycle number is presented in Fig. 4.30 d). In the first cycle, irreversible losses of 160 mAh/g are observed dropping down to 0 mAh/g in the second cycle. The irreversible losses increase continuously to about 112 mAh/g. After cycle 5 no clear trend is detectable. The irreversible losses seem to increase or decrease randomly. The fading is almost zero in the range from cycle 1 to cycle 6. From the seventh cycle on, the fading of the gravimetric capacity is present and increases. Starting from cycle 8, the fading curve follows the behavior of the irreversible losses. In the first 6 cycles, the difference between irreversible losses and the fading are identical to the trend of the irreversible losses. Cycle 7 is the transition point and from cycle 8 on, the difference between irreversible losses and fading approaches a constant value of around 15 mAh/g.

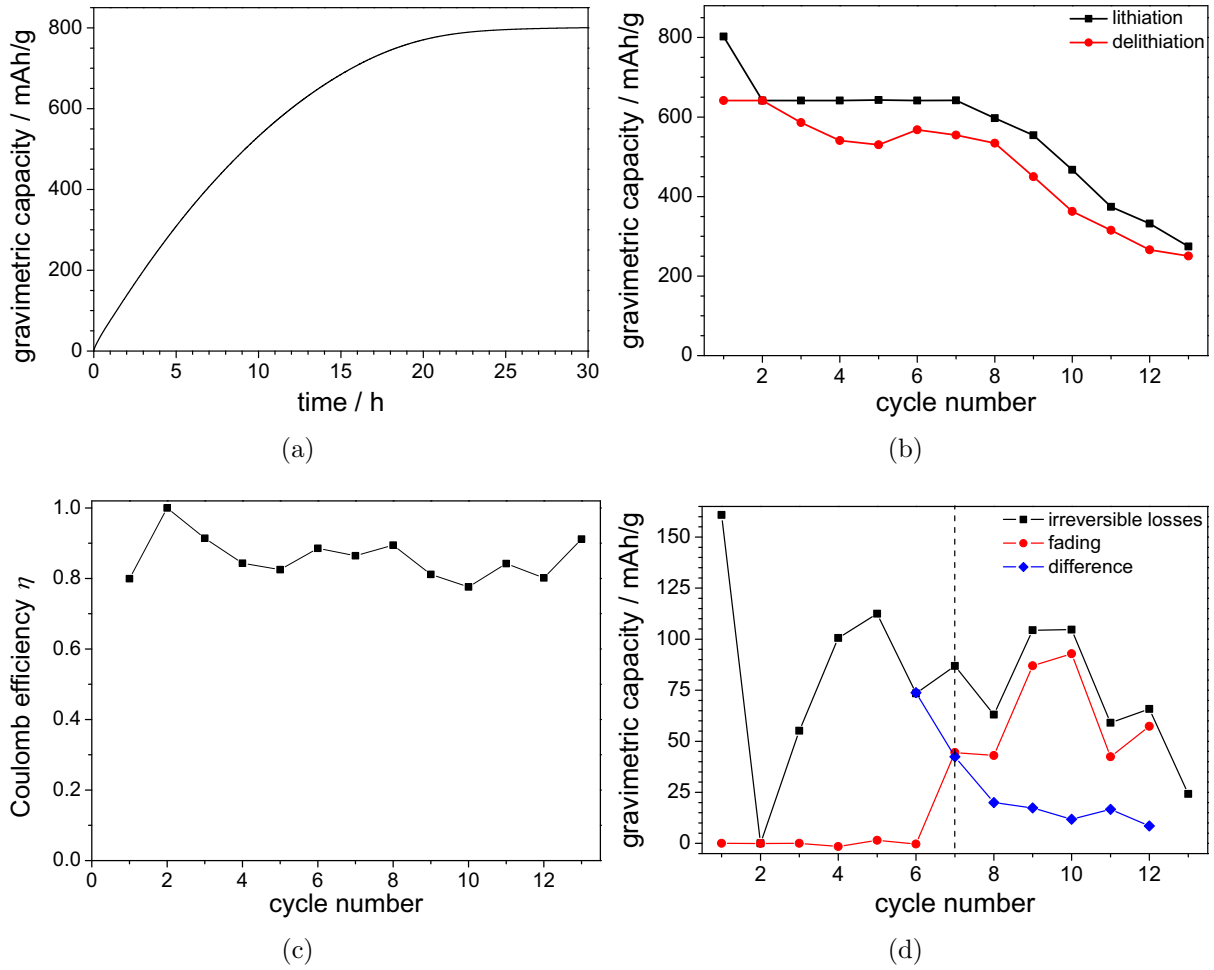

Figure 4.30: a) Gravimetric capacity *vs.* charging time curve of a porous InP anode being potentiostatically charged at 0.15 V, b) battery cycling test of the porous InP anode. The first lithiation was performed to 100 % and afterwards only to 80 % of the maximum gravimetric capacity. c) Coulomb efficiency of the InP anode, and d) plot of the irreversible loss, the fading and their difference.

4.4.4 Impact of Al_2O_3 coating on the battery performance

The aim of the Al_2O_3 coating on the InP pore walls is to produce a stable SEI layer and thus, to stabilize the surface of the InP pore walls. This coating needs to be thin enough to allow for the in-diffusion and out-diffusion of Li-ions.

The anode was prepared as stated in section 4.1 with a membrane thickness of about 240 µm. After the cathodic post-etching the mean pore wall width is about 160 nm. The entire membrane structure is covered with an 8 nm thick layer of Al_2O_3 before a Cu current collector with a thickness of 2 µm is sputter-deposited on the front side of the anode. The appearance of the completely processed anode is very similar to the uncoated porous anode presented in Fig. 4.25.

Electrochemical analysis of the Al_2O_3 coated porous InP anode

Cyclic voltammetry The cyclic voltammmograms are performed instead of the XRD analysis, to investigate the effect of the Al_2O_3 coating on the lithiation and delithiation behavior of the anode. As also done in the previously shown cyclic voltammorgrams, the current is plotted over the potential *vs.* Li^+/Li. The negative voltage sweep is the bottom half of the curve being related to the lithation, while the positive voltage sweep represents the delithiation of the anode.

Figure 4.31 presents the first and second lithiation and delithiation cycle of the coated porous InP anode. During the first lithiation of the anode three peaks are observed at 1.08 V, 0.65 V, and 0.39 V – from higher to lower potentials. For the first delithiation three peaks are observed at 0.75 V, 0.92 V, and 1.25 V. As shown in Fig. 4.31, the most of the observed peaks in the second cycle are only slightly shifted. The peak observed at 1.08 V in the first cycle disappeared.

Compared to the peak positions of the first cycle of the uncoated porous InP anode, the peaks of the Al_2O_3 coated porous InP anode are found to be almost at the same position, except for the peak at 0.64 V which is shifted by 0.1 V. A peak at 1.08 V was not observed for the uncoated porous InP anode. For the second cycle, the situation is very similar. The peak positions of the second cycle are also nearly completely identical to the ones observed for the uncoated porous InP anode. The only exception is the peak at 0.35 V which is shifted by 0.07 V compared to the uncoated porous InP anode.

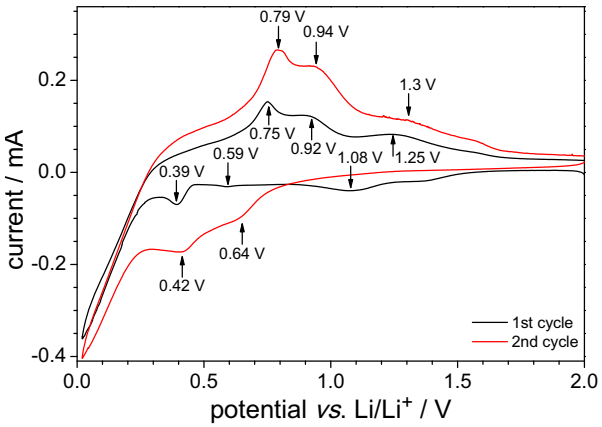

Figure 4.31: Cyclic voltammograms of the Al_2O_3 coated porous InP anode of the first and second cycle, cycled between 0 V and 2 V with a scan rate of 0.1 mV/s.

The coincidence in the peak positions with the uncoated porous anode and the literature [32, 89] allows to assign the peaks formed around 0.35 V and 0.79 V to the redox couple of In_3Li_{13} / In at ∼0.35 V / ∼0.8 V. Correspondingly, the peaks found at 0.64 V and 0.94 V are assigned to the redox-couple of LiP / P at ∼0.62 V / ∼0.96 V. This means that the lithiation and delithiation of the porous InP anode through the 8 nm thick layer of Al_2O_3 is possible and seems to be chemically not affected by the Al_2O_3 coating. The peak observed at 1.08 V may be attributed to the formation of the SEI layer analogously to the uncoated porous InP anode, but due to the high chemical stability of Al_2O_3 the SEI layer forms already at lower potentials compared to the uncoated InP anode.

Standard battery cycling tests The maximum gravimetric capacity of InP was already determined for the uncoated porous InP anode described in section 4.4.3. Thus, the same charging and discharging concept is used for the standard battery cycling tests, but with different voltage and current limits. The voltage limit where the charging mode is switched from galvanostatic to potentiostatic charging is 0.3 V. This limit is chosen to reduce chemical side reactions occurring after the lithiation of In is completed. The voltage limit for the anode discharge is at 0.9 V. This comparatively high voltage limit should prevent the formation of crystalline InP during delithiation and thus, mechanical stresses in the pore walls due to the reorganization.

In the first two cycles the gravimetric capacity stored in the anode is only around 40 mAh/g unlike the uncoated InP anode where the maximum gravimetric capacity is reached in the first cycle. In the third cycle the gravimetric capacity drastically increases to about 250 mAh/g before it slightly decays to about 230 mAh/g. The maximum gravimetric capacity of about 280 mAh/g is found in the eighth cycle. Starting from cycle eight the capacity begins to decrease again, at first moderately till the 18^{th} cycle and then drastically till a gravimetric capacity close to zero is reached in the 30^{th} cycle. The maximum possible gravimetric capacity of the uncoated InP anode (800 mAh/g) is not reached for the Al_2O_3 coated anode.

The delithiation curve is always well below the lithiation curve, except for the last cycles. This indicates a rather bad Coulomb efficiency, which is depicted in Fig. 4.32 b). The Coulomb efficiency of the anode increases from about 0.4 in the first cycle up to around 0.85 in the 4^{th} cycle after a drop in the third cycle. A plateau region with a Coulomb efficiency of about 0.85 ranges from cycle 4 till cycle 17. In the 18^{th} cycle the Coulomb efficiency drops abruptly and reaches a minimum in cycle 22 before it increases close to unity in the last two cycles.

The trend of the irreversible losses and the fading with increasing cycle number is presented in Fig. 4.32 c). Starting from around 22 mAh/g the irreversible losses tend to decrease before the maximum value of about 87 mAh/g is reached in cycle 3. The irreversible losses form a plateau region at about 30 mAh/g ranging from cycle 4 to 17 with the tendency to slightly decrease with increasing cycle number. A small dip in the irreversible losses in this plateau region is found for cycle 5 and 6. In cycle 18 the irreversible losses abruptly increase to about 45 mAh/g. In the following the irreversible losses are steadily decreasing down to 0 at cycle 30.

In the first two cycles only a negative fading is observed. In this case a negative fading describes a gain in the gravimetric capacity of the anode compared to the previous cycle [see Fig. 4.32 a)]. In cycle 3 and 4 the fading is positive again and increases up to almost 21 mAh/g before the fading is negative again in cycle 5 to 7 (gain in the gravimetric

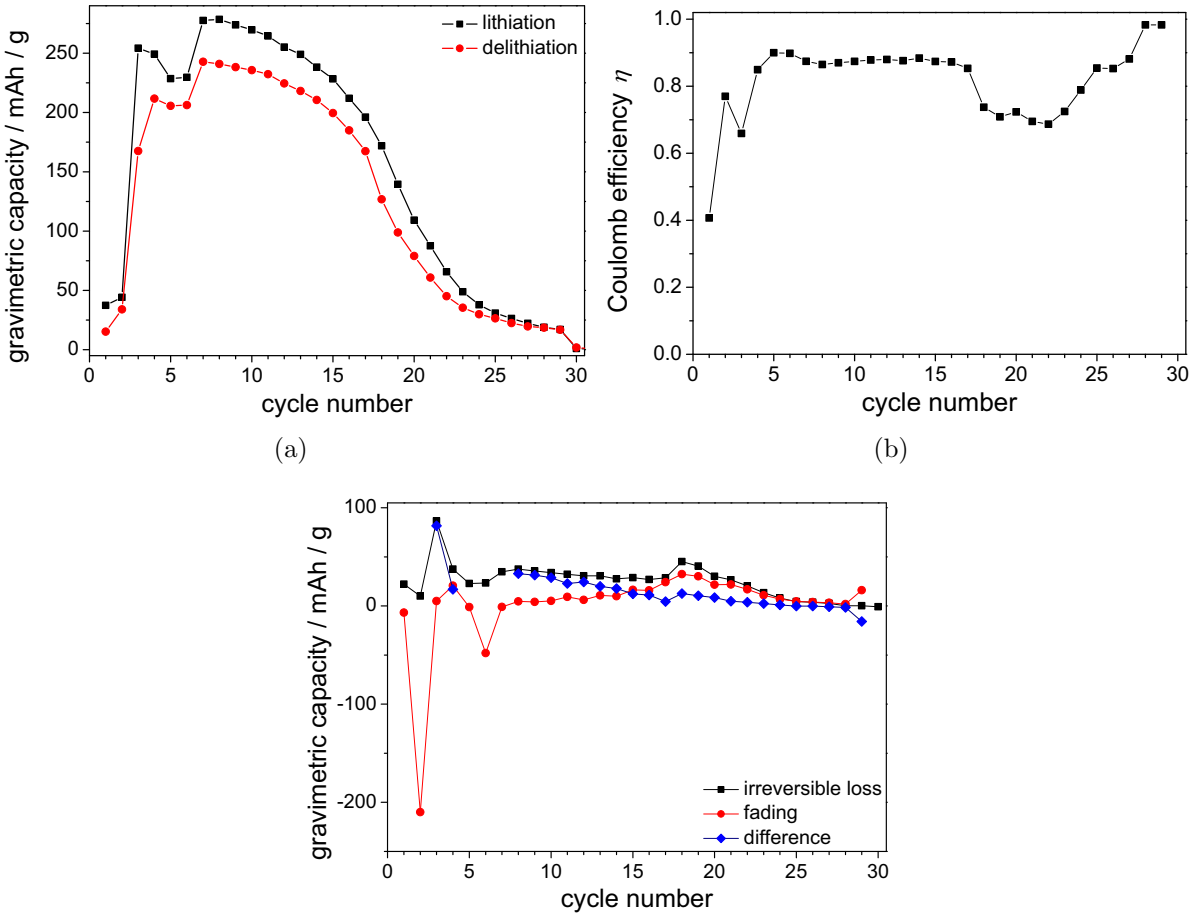

Figure 4.32: a) Battery cycling test of the porous Al_2O_3 coated InP anode. The first lithiation was performed to 100 % and afterwards only to 80 % of the maximum gravimetric capacity. b) Coulomb efficiency of the same InP anode, and c) plot of the irreversible loss, the fading and their difference.

capacity of the anode). Starting from cycle 7 the fading constantly increases and reaches the maximum of about 32 mAh/g in cycle 18. From cycle 18 the fading decays down to almost zero before it jumps up to about 16 mAh/g in cycle 29.

Where the fading is negative, the difference between irreversible losses and fading is not a useful quantity to detect if the irreversible losses are due to fading. Therefore, the data points for these cycles are not included. In the range between cycle 7 and 20, the difference between the irreversible losses and the fading is steadily decreasing, except for cycle 18. Starting from cycle 20 the difference between the irreversible losses and the fading is alternating around 0 and almost constant except for the 30^{th} cycle.

Structural analysis in the delithiated state

In Fig. 4.33 the Al_2O_3 coated porous InP anode is depicted after 50 cycles of lithiation and delithiation. As for the uncoated InP anode, the Al_2O_3 coated anode was dismantled from the half-cell in a glove box under an Ar atmosphere before performing the SEM analysis. Figure 4.33 a) gives a top view of the surface of the anode. The randomly distributed dark

fibers on top of the anode are not detached InP pore walls, but originate from the glass fiber microfilter being used as separator material. The crack in the bottom right corner is not necessarily a result of the lithiation and delithiation, but is most probably due to the sample handling prior to the SEM investigation. One observes that the anode is in rather good shape. This means, the pore structure does not collapse or even pulverize. Although dead in terms of retaining and delivering charge, the anode still shows a pore structure at least to a certain degree. Compared to the delithiated uncoated InP anode, hardly any remains of the SEI layer are found on the surface of the anode after 50 cycles.

A magnified image of the anode surface resolving the pore structure in more detail is depicted in Fig. 4.33 b). One can still identify the pore structure of the unlithiated anode with the rectangular pore shape, although the pore structure observed in Fig. 4.33 b) is not as perfect as it was in the unlithiated state. Instead, most pore walls appear not perfectly flat anymore and the surface exhibits either loosely connected or even disconnected particles. A faceting of the pore walls similar to the one observed in the lithiated and delithiated state of the uncoated anode (Fig. 4.25) is not found.

Figure 4.33 c) presents a top view of the same anode at a different position. In contrast to the previous image, hardly any pores can be detected. The anode surface at this position looks more like the lithiated surface of the uncoated InP anode shown in Fig. 4.26 than the delithiated surface shown in Fig. 4.33 a) and b). The previous hexagonal pore structure is completely lost. It seems as if the Al_2O_3 coating is not present anymore, because the pore walls enlarged so drastically. A faceting of the pore walls is also found, but to a less ordered degree compared to the uncoated anode in Fig. 4.25. It is not possible to identify a regular bulging and necking sequence of the pore walls. Instead a rather crumb-like morphology of the pore walls is found.

Figure 4.33 d)–f) give cross-sectional views of the anode. The orange dotted line shows the single curro-pores. In Fig. 4.33 d) the pores and the corresponding pore walls are easily identified. As for the uncoated InP, the pore wall width of the Al_2O_3 coated InP anode is around 370 nm, being far higher compared to the pore wall width (about 160 nm) of the unlithiated InP anode. The pore walls do not show any break-offs and are rather flat. The Al_2O_3 coating – bright layer at the edges of the pore walls – is still attached to the pore walls, as exemplarily shown at some positions by the orange arrows in Fig. 4.33 d). Small bright shining particles in the nanometer range are found on the pore walls. Similar to the discharged uncoated InP anode, these bright particles are most probably LiF as a result of electrolyte decomposition and further side reactions.

Compared to Fig. 4.33 d), the pores in Fig. 4.33 e) are hardly visible and the pore wall width is about 580 nm which is significantly larger compared to the pore wall width observed in Fig. 4.33 d), thus, even more Li is still incorporated in the InP pore walls. The Al_2O_3 coating is burst open and delaminated from the pore walls. These positions are marked by the orange arrows. Besides the Al_2O_3 delaminates, one also observes a high number of particles lying on the pore walls. These particles show a large size variation. The bright nanometer-sized particles are again most probably LiF. The large particles on the other hand may have detached from the pore walls, since the few visible pore walls are not flat as shown in Fig. 4.33 d), but exhibit small partial break-offs. These detached particles can be directly related to the capacity loss of the anode, because detached particles will not contribute to the battery capacity in further cycles anymore.

Figure 4.33 f) is the prolongation of e) down to the current collector. The pore walls are frazzled and seem to be discontiguous. An Al_2O_3 coating cannot be detected anymore.

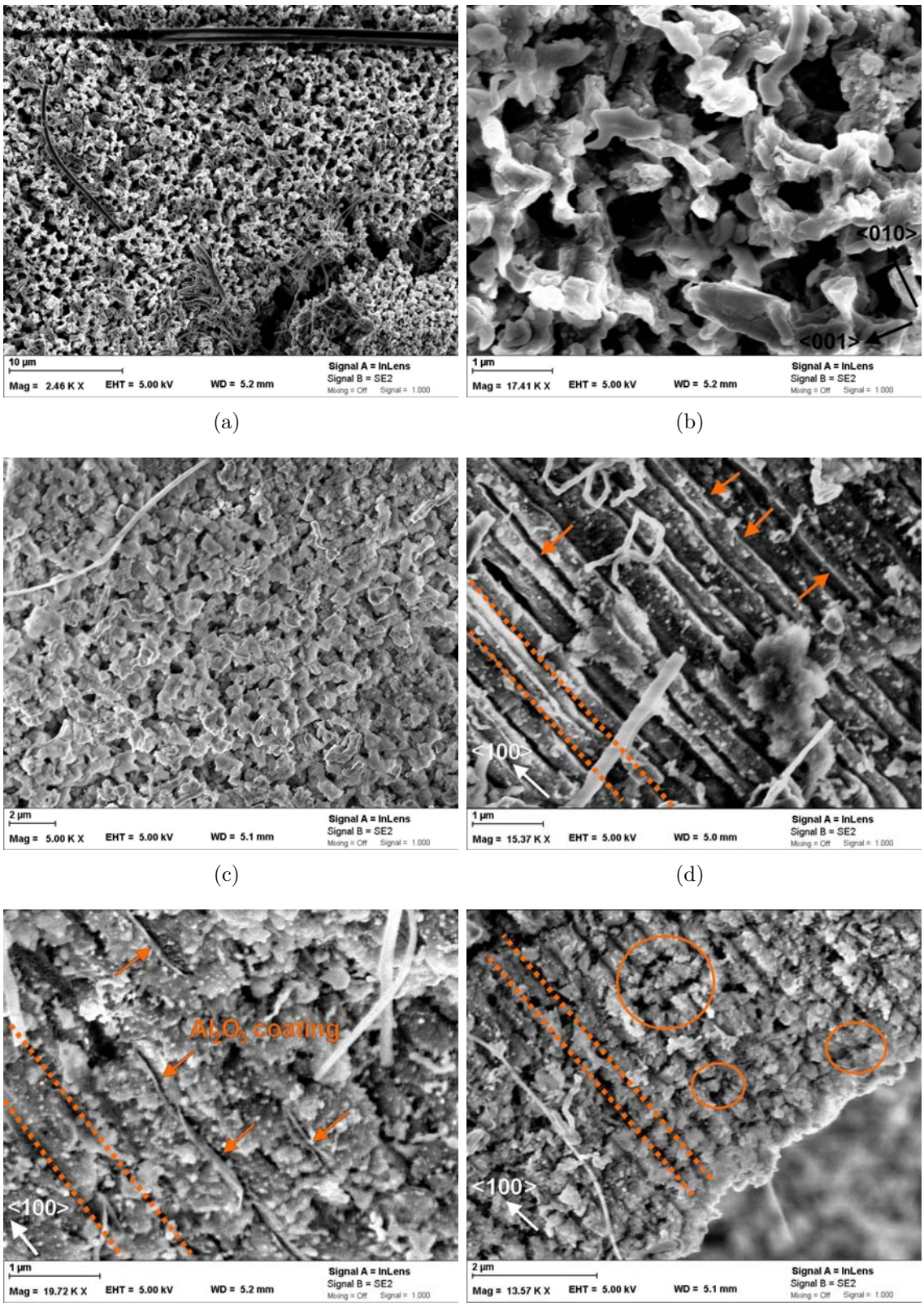

Figure 4.33: a) Top view on the (100) plane of the delithiated Al_2O_3 coated porous InP anode after 50 cycles, b) in high magnification, and c) at a different position on the surface. Cross-sectional view on the (110) plane of the anode d) at a middle pore depth, e) similar pore depth, but at a different position, and f) near the Cu current collector. The dotted orange lines show the curro-pores. The vectors indicate the pore orientation.

One also observes laterally fractured pore walls in some spots (orange circles). These fractures are also found directly at the current collector (right orange circle). This might be one of the reasons for the failure of the anode after 30 cycles.

Chapter 5

Discussion

5.1 InP membrane fabrication

5.1.1 Two-stepped membrane fabrication process

The membrane fabrication process is a two-step process. The first step is the photo-electrochemical porosification of the bulk wafer back side with crysto-pores and the second step is the subsequent photochemical dissolution of the crysto-porous layer grown in the first step.

In this first step it is essential that the crysto-pores grow into the depth with a straight pore front parallel to the surface in order to achieve a homogeneous opening of the underlying curro-pore array over the entire sample area. Leisner showed in his work [78] that this can be achieved in InP with a carrier concentration of 1×10^{17} cm^{-3} only for a very low etching current density around 1 mA/cm^2. The drawback of this very low etching current density is the long etching time. Increasing the etching current density results in the transition from crysto-pores with a straight pore front to curristo-pores with a wavy pore front [78]. With increasing current density, also the depth decreases in which this transition occurs.

This problem is circumvented by simultaneously illuminating during the electrochemical crysto-pore growth. This illumination with blue light during the electrochemical etching of crysto-pores generates an additional etching current. This photo–etching current already dissolves the growing crysto-porous layer starting from the surface, while the crysto-pores grow further into the depth. This technique allows to use a higher etching current density even close to the transition to curristo pore growth without loosing the homogeneous growth of the crysto-pores. As soon as the crysto-porous layer has reached the pore tips of the underlying curro-pore array no further external etching current supply is needed.

In the second step the dissolution is done purely photochemically. The purely photochemical dissolution is chosen, because it achieves a highly selective etching of the crysto-porous layer with respect to the underlying curro-pore array. A possible reason for this behavior is the high surface roughness of the crysto-porous layer that results in a higher photo current and thus, in a higher etching rate of the crysto-porous layer compared to the dissolution of the curro-pore walls. The selectivity of the photochemical dissolution would benefit most probably from a change to UV illumination instead of blue illumination due to the lower absorption depth.

5.1.2 Tailoring the membrane back side

The differences in the shape of the pore opening from flat to cone-like, as shown in in Fig. 4.5, can be understood by different etching rates for the top surface of the pore walls and the side of the pore walls depending on the illumination intensity.

A flat pore wall top surface indicates a much higher etching at the top compared to the sides of the pore wall. The illumination generates electron-hole pairs at the surface resulting in a local excess of holes in the surface-near region, as depicted in Fig. 5.1 a). This hole excess will build up a local photo-voltage driving most probably the electrochemical dissolution by a current flow from the illuminated part of the InP pore walls into the electrolyte, then through the electrolyte, and finally back into the non-illuminated part deeper into the pores, as schematically depicted by the electric circuit in Fig. 5.1 a).

The resistances R_e and R_w depicted in Fig. 4.2 are schematic representations of the voltage losses induced by the current flow including e.g. the strong non-linear losses due to, diffusion, and nearly ohmic losses in the InP pore walls. An increase in the photo-current density due to an increased illumination of the InP membrane would lead to higher ohmic losses in R_e, and thus, to shorter distances l in which the photo-induced anodic potential ΔU transforms into the cathodic potential of the non-illuminated InP pore wall / electrolyte interface. This is depicted in the small l *vs.* U graph in the upper right part of Fig. 5.1 a).

The occurrence of highly wedged, cone-like pore walls – depicted in Fig. 4.5 d) – can therefore be explained by means of an (ohmic) voltage drop over several hundreds of nanometers as a result of a low local etching-current density. The extended distance l can be understood as a consequence of the reduced ohmic losses due to the lower photo-current. This is schematically depicted in Fig. 5.1 b). The same explanation may hold also for the distance from the illuminated wafer back side surface in Fig. 4.2 a) where a

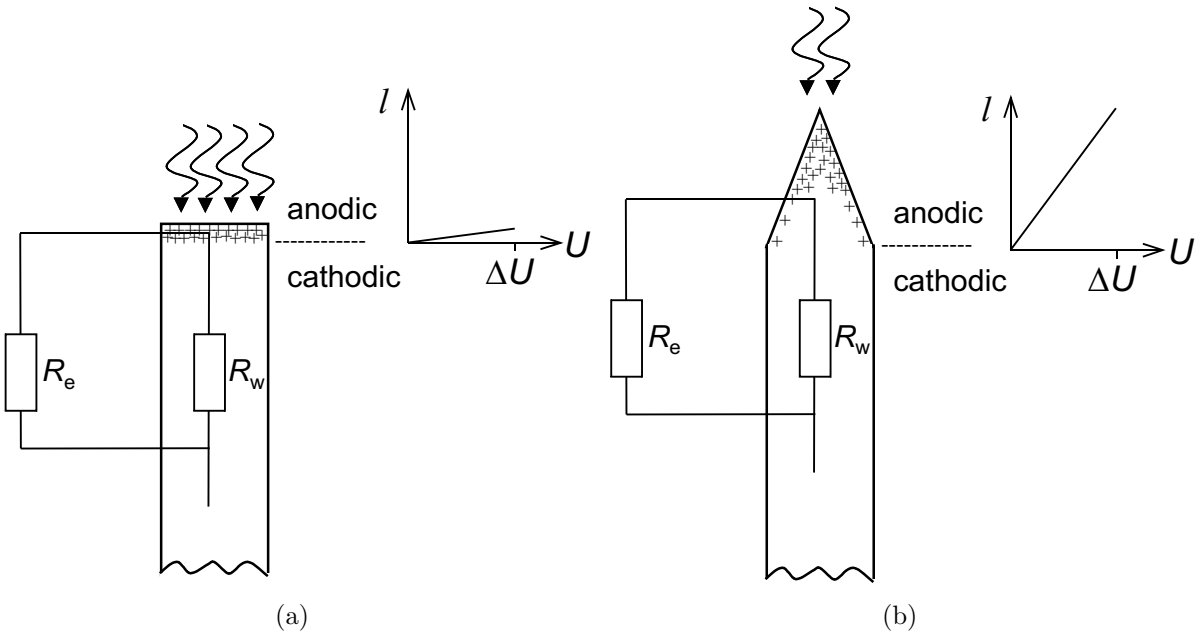

Figure 5.1: Schematic representation of the etching mechanism for tailoring the membrane back side for a) flat pore openings and b) cone-like pore opening.

widening of the crysto-pore diameter is observed.

The uphill and down dale structure of the crysto-porous layer on top of the curro-pore array depicted in Fig. 4.6 can be understood as the result of the transition between the growth of crysto-pores and curristo-pores and preferential dissolution. The transition from crysto-pores to curristo-pores occurs in a certain depth when the applied etching current density is too high for ideal crysto-pore growth. Leisner found that curristo-pores often grow radially symmetric with a wavy pore front [78]. A higher etch rate of the curristo-pore walls compared to the pore walls of the crysto-pores results in the preferential dissolution of the curristo-pore structure and thus, in the uphill and down dale surface shown in Fig. 4.6 d).

5.1.3 FFT-impedance spectroscopy of the membrane fabrication process

The membrane fabrication process is divided into two major steps, the photo-electrochemical crysto-pore formation and the photochemical dissolution. The first step can be further subdivided into four regions, as shown in Fig. 4.8. The regions I and II can be assigned to the nucleation and growth of the crysto-porous layer into the bulk wafer back side. This is schematically illustrated in Fig. 5.2 a). The beginning of region III could be identified as the moment in which the first crysto-pores reach the tips of the underlying curro-pore array. With further increasing time, more and more crysto-pores reach the pore tips of the curro-pore array. This is accompanied by an exponential decrease of R_s. In region IV, all curro-pore tips have been reached by crysto-pores resulting in a constant R_s and R_p. The reason for the slight decrease in C_p could be the further increase in the porosity of the crysto-porous layer till the end of this process step, which is shown in Fig. 5.2 b).

The purely photochemical dissolution step can be subdivided into two regions, as shown in the FFT-IS fits in Fig. 4.9 a). The corresponding schematic pore structure is depicted in Fig. 5.2 c). After a certain photochemical etching time a dip occurs in the resistance R_s. At this moment the crysto-porous layer being on top of the curro-pore array is completely dissolved in the first areas. The curro-pore array is now opened and R_s remains constant. The capacity C_p declines exponentially from the beginning of the photochemical etching, because more and more of the crysto-porous layer is dissolved. The dissolution of the crysto-porous layer is completed as soon as C_p reaches a constant value. This situation is schematically illustrated in Fig. 5.2 d). This means, the terminal point of the photochemical part of the membrane fabrication process is easily detectable *in situ* by FFT-IS. This also allows to rapidly adjust the membrane fabrication process to different wafer thicknesses or pore lengths.

In addition to the identification of separate phases in the membrane fabrication processes for the process characterization, the *in situ* FFT-impedance spectroscopy analysis allows also to detect malfunctions during the etching process, which was shown in Fig. 4.9 b). In the middle of the photochemical etching step high oscillations in R_s are found. These oscillations can be assigned to gas bubbles that adsorbed on and desorbed from the back side surface of the membrane. The gas bubble adsorption and growth of the gas bubble is translated into an increase of the series resistance R_s, the desorption from the surface into a decrease of R_s. This adsorption and desorption result in oscillations in R_s. By looking only at the voltage-time curve, it is not possible to detect these oscillations.

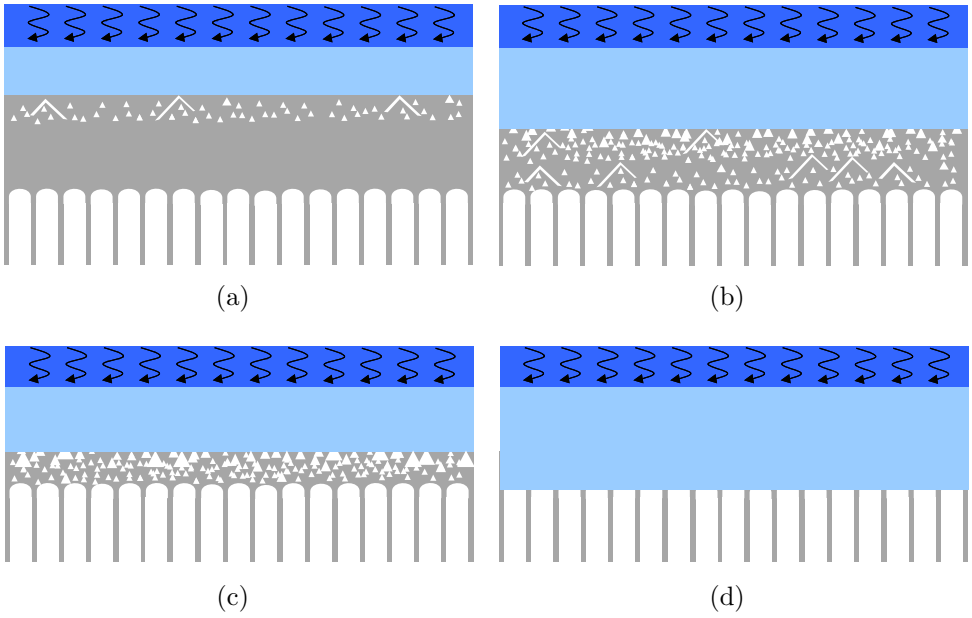

Figure 5.2: Schematic pore structure in certain process phases of the photo-electrochemical / photochemical membrane formation a) 1st step, region II: photo-electrochemical porosification of the bulk back side, b) 1st step, region IV: intermediate state of the photo-electrochemical porosification, c) 2nd step: purely photochemical dissolution of the crysto-porous layer, and d) final state: completely open membrane structure.

5.1.4 Post-etching of porous structures under cathodic bias

Figure 5.3 illustrates the change of the SCR width depending on the electric conditions during the processing steps. For the sake of simplicity the pores are assumed to be perfectly round allowing to neglect the influence at corners.

During the anodic etching of the curro-pore array the SCR of neighboring pores overlap leaving areas between neighboring pores where no SCR is present, in the following called spandrels. This situation is schematically shown in Fig. 5.3 a). After switching off the anodic etching potential, the SCR surrounding each pore diminishes simply because of the potential difference between the anodic etching potential and the open circuit potential (built-in potential). The pore size and the pore wall width are unaffected by this change, but the area without SCR is significantly increased – see Fig. 5.3 b). The area of these spandrels cannot be decreased by further anodic etching, because the pore diameter and the width of the pore walls directly depend on the anodic etching voltage and on the doping carrier concentration. The post-etching under open circuit conditions allows to decrease the spandrels till the SCR of neighboring pores overlap again. Nevertheless, the area of the spandrels can only be slightly reduced.

By applying a cathodic potential to the pore array results in a further decrease of width of the SCR around each pore. This artificial shrinkage of the SCR – shown in Fig. 5.3 a) – allows to further increase the pore diameter by chemical post etching and thus, decrease the pore wall width. Due to the composition of the chemical constituents of the post-etching electrolyte with the strong oxidant HNO_3 and the passivating properties of the organic components, the etching stops as soon as the SCRs of neighboring pores overlap.

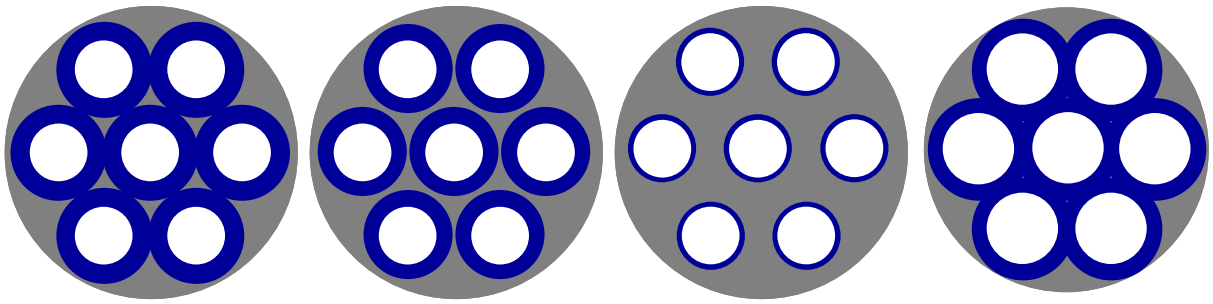

(a) (b) (c) (d)

Figure 5.3: Top view on the schematic pore array with surrounding SCR a) during anodic pore etching, b) after anodic pore etching at open circuit conditions, c) during cathodic post-etching, and d) after cathodic post-etching at open circuit conditions.

After the cathodic potential is removed, the SCRs surrounding each pore increase their width due to the potential difference between the cathodic potential and the open circuit potential, as illustrated in Fig. 5.3 d). Due to the strong decrease in the pore wall width, the SCRs overlap almost completely and the spandrels are almost completely removed. This results in an increased resistivity of the InP pore walls, because pore walls behave now almost like an insulator, since the SCR governs almost the complete pore wall diameter.

InP nanowires are obtained when a high cathodic bias ($\geq$ 1.4 V) is applied during post-etching. In this case, the SCR around each pore becomes extremely small, so that the InP pore walls are dissolved preferentially at the corners of the pores due to the field strength enhancement originating from the high curvature of the corners. The pores grow into each other with nanowires as remains of the former pore walls.

5.2 Galvanic deposition of metal nanostructures

5.2.1 Pulsed current *vs.* constant current metal deposition

In InP pore arrays the usage of the constant current deposition mode has the disadvantage of plugging the pore openings of the curro-pore array after a short time because of preferential deposition near the pore opening. This deposition behavior can be explained by the cathodic deposition conditions that also reduce the width of the SCR in the pore walls, so that conductive channels develop in the pore walls that allow for a current flow through the pore walls. This current flow results in the metal deposition on the pore walls at the InP/electrolyte interface. This is true for the InP pore array as well as for the uncoated InP membrane. Thus, in the case of galvanostatic deposition, the deposition occurs preferentially near the pore openings, because a concentration gradient is building up between the pore openings and the pore tips during the deposition. The metal ion concentration at the pore opening is close to the metal ion concentration in the electrolyte, while it is lowest at the tips of the curro-pore array.

Switching to a pulsed current deposition mode results in the deposition of Ni particles on the pore walls homogeneously distributed over the complete pore depth, as shown for an InP pore array in Fig. 4.12 a), because the concentration gradient of the metal

ions between pore openings and pore tips levels out during the recovery time where no current is applied. The size and the number of the deposited particles can be influenced by several parameters, such as pulse frequency, pulse length *et cetera*. The results shown in this work are related to the optimized deposition parameters.

The deposition of single particles on the pore walls could result in the formation of tubes – if the particles sizes are small enough, as shown by Tiginyanu [28]. The other possibility is the formation of porous nanowires in case of higher particle sizes, as presented in Fig. 4.12 b). Dense nanowires cannot be obtained because fine gaps in the middle of the tube will remain unfilled due to an extremely increasing aspect ratio of the unfilled inner tube during deposition and the associated formation of a high concentration gradient.

The deposition of particles on the pore walls can be reduced by post-etching of the InP membrane under high cathodic bias prior to the galvanic deposition, because the conductive channels are reduced due to the thinner pore walls. The deposition on pore walls is efficiently prevented by electrically passivating the InP pore walls with a thin insulating layer of Al_2O_3, because a current flow from the plating base through the pore walls is not possible anymore. Instead, the metal deposition starts on the Au plating base and continues on the previously deposited metal. Therefore, the metal deposition can be performed either by constant or by pulsed current deposition.

5.2.2 FFT-impedance spectroscopy of the Ni deposition process

As evident from the time dependence of the fit parameters depicted in Fig. 4.24, the galvanic deposition process can be subdivided into three sections. Section I is characterized by the nucleation of Ni crystallites on the plating base and the subsequent growth of early crystallites. Section II and III are characterized by the continuous growth of the nanowires. The length of the Ni nanowires increases with increasing deposition time.

The series resistance R_s reflects the features observed in the deposition voltage U. When U increases to more negative values, R_s follows in the same way. This behavior can be understood by Ohm's law taking into account that the deposition occurs at constant current. The gain in R_s could be explained by the formation and growth of gas bubbles on the sample surface. The abrupt drops in R_s are most probably due to the desorption of gas bubbles. The gas bubbles are most probably hydrogen based. Hydrogen can form as a side reaction of the metal deposition process [92]. In the recorded FFT-IS data, a process related to the hydrogen formation during Ni deposition could not be detected in the investigated frequency range, because it is most probably a very slow process [93] that is outside the investigated frequency regime.

The resistance R_p and relaxation time τ_p could describe the influence of boric acid on the Ni deposition. The negative resistance could be understood in terms of a reaction facilitating the Ni deposition. According to Hoare [94], boric acid acts as a catalyst facilitating the Ni deposition by forming a complex with Ni ions that allow for a deposition of Ni at a lower overpotential. The presence of boric acid also reduces the active area for hydrogen evolution on the metal surface during the deposition [94]. The increase in R_p towards more negative values could therefore be due to an increase in the concentration of boric acid in the pores with decreasing pore depth, since the Ni nanowires grow in length with increasing deposition time. The higher oscillations in R_p towards the end of section III may be due to a competition for adsorbing sites on the Ni nanowires surface between boric acid and other adsorbed species. The decrease in the relaxation time τ_p could be

understood in the same way as for R_p.

It is well known that several corresponding equivalent circuits describe the same impedance data. For example, two RC elements connected in series can be transformed into a Voigt model or a Maxwell model. All possible arrangements (various Voigt model arrangements, Maxwell model arrangements etc.) have been tested to describe the measured impedance data. The chosen Maxwell model appears to be the most suitable model to consistently describe the single chemical reactions taking place during the deposition experiment because of two reasons. The first is, it is expected from literature [92, 94, 95] that at least two chemical reactions take place in parallel. The second is that the decoupling of the measured impedance data *vs.* time is best with the Maxwell model compared to all other tested equivalent representations.

The Maxwell resistance R_a could be related to the charge transfer resistance associated with the Ni deposition. The rise in R_a in section III may be attributed to an increased coverage of the Ni nanowire surface by adsorbed ions inhibiting the Ni reduction on the Ni surface [92]. These adsorbed ions are probably Cl^-. The constant behavior of R_a in section I and II shows that the charge transfer resistance is independent of an increasing concentration of boric acid at the Ni nanowire surface.

The double layer capacity could be attributed to the capacity C_a. In section II, the decreasing capacity of the double layer could be correlated to the increasing concentration of boric acid at the surface of the Ni nanowires. In section III the stronger decrease in C_a could be explained by a strongly increasing concentration of a different kind of adsorbed ions in the same way as for the resistance R_a.

The Maxwell resistance R_b and the capacity C_b describe the slowest process during the Ni deposition. It could be assigned to the passivation of the Ni nanowire surface associated most commonly with adsorbed ions [95]. This passivation process takes place in parallel to the Ni deposition and inhibits the Ni deposition. The rise in R_b in section III could be associated with an increase in the concentration of anions on the Ni nanowire surface increasing this passivation.

The decreasing trend of the corresponding capacity C_b could be related to an increasing concentration of anions. This increasing concentration of anions can be understood in terms of running down of a diffusion limitation inside the pores. The end of the diffusion limitation is due to the decreasing pore length with increasing Ni nanowire length. The single sharp peak in section III at around 53 min is most probably a fitting artifact and has no physical meaning.

5.3 Structure & magnetic properties of magnetic metal nanostructures

5.3.1 Structure of the Ni particles

The pulsed current Ni deposition inside the InP pore arrays and uncoated InP membranes results in Ni particles, resp. porous Ni nanowires consisting of interconnected Ni particles with a particle diameter of about 50 nm in both cases. The XRD analysis revealed an average Ni crystallite size of about 10 nm. This strong deviation in the particle size compared to the Ni crystallite can be explained by oxidization of the Ni crystallites due to their high surface area compared to their volume. The high surface area facilitates the

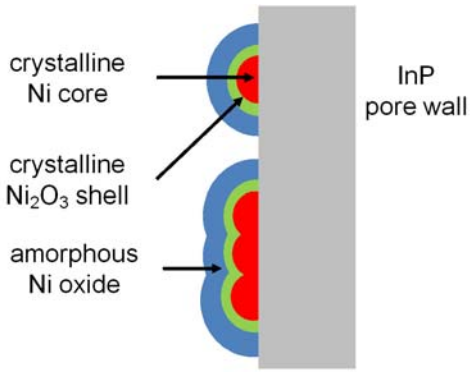

Figure 5.4: Schematic structure of the deposited single Ni particles and interconnected Ni particles on the InP pore walls.

oxidization of the Ni crystallites. Thus, the Ni crystallite size is much smaller than the observed particle size. The small peaks associated with crystalline Ni_2O_3 suggest a core shell structure with a Ni_2O_3 shell surrounding the crystalline Ni core. The outer part of the Ni particle is most probably occupied by an amorphous Ni oxide. The schematic structure of the galvanically deposited Ni nanoparticles is illustrated in the top part of Fig. 5.4, while in the bottom part the interconnected particles of the porous Ni nanowires are depicted. The less pronounced peaks for Ni_2O_3 in the XRD pattern shown in Fig. 4.12 d) could be explained by the interconnection of the Ni crystallites reducing the surface to volume ratio and thus, the effective surface for oxidation.

5.3.2 Magnetic properties

Ni nanoparticles embedded in InP pore array

From the hysteresis loops recorded along and perpendicular to the long pore axis $\boldsymbol{z}$ – shown in Fig. 4.16 a) – it is evident that an easy magnetization direction is present for the Ni particle ensemble. The easy magnetization direction is oriented along the long pore axis $\boldsymbol{z}$, because the nanoparticles are arranged in a tube-like structure [see Fig. 4.12 a) and A.1] where the particle distance between neighboring particles is much shorter along the pore axis $\boldsymbol{z}$ than perpendicular to $\boldsymbol{z}$. Thus, the magnetostatic interactions between the Ni nanoparticles are far more pronounced along $\boldsymbol{z}$. The tube-like arrangement of the Ni nanoparticles gives rise to a shape anisotropy that favors the alignment of the magnetization direction along $\boldsymbol{z}$. The easy magnetization direction along $\boldsymbol{z}$ can explain the higher remanence squareness, coercivity, and the lower saturation field for $\boldsymbol{H} \parallel \boldsymbol{z}$ compared to $\boldsymbol{H} \perp \boldsymbol{z}$. The paramagnetic crystalline Ni_2O_3 seems to have no influence on the magnetic properties of the Ni / InP composite at room temperature.

Porous Ni nanowires embedded in InP membrane

The hysteresis loops recorded in parallel to the long pore axis and perpendicular to it show a high similarity in shape, as depicted in Fig. 4.16 b). This indicates a rather isotropic magnetic behavior. This rather isotropic behavior can be understood in terms of magnetostatic interactions. Unlike for the Ni particles, the porous Ni nanowires allow for magnetostatic interactions between the single particles of the porous Ni nanowire

also in other directions than along $\boldsymbol{z}$. The significantly lower saturation field found for $\boldsymbol{H} \parallel \boldsymbol{z}$ compared to $\boldsymbol{H} \perp \boldsymbol{z}$ indicates an easy magnetization direction lying along the long nanowire axis $\boldsymbol{z}$. The big difference in the saturation fields between $\boldsymbol{H} \parallel \boldsymbol{z}$ and $\boldsymbol{H} \perp \boldsymbol{z}$ might be attributed to a slightly preferential orientation of the Ni crystallites and the porous character of the Ni nanowires. The coercivity for $\boldsymbol{H} \perp \boldsymbol{z}$ is higher compared to $\boldsymbol{H} \parallel \boldsymbol{z}$. This behavior could be understood by the porous structure of the Ni nanowires that could hinder the domain wall movement in case of $\boldsymbol{H} \perp \boldsymbol{z}$ resulting in a higher coercivity compared to the case of $\boldsymbol{H} \parallel \boldsymbol{z}$.

Ni nanowires embedded in InP membrane

When the external magnetic field is applied to the Ni nanowires perpendicular to the long wire axis $\boldsymbol{z}$ under various incidence angles β no changes in the hysteresis loops are observed. This means, the Ni nanowires seem to behave magnetically isotropic with respect to the incidence angle of the external magnetic field. Furthermore, it seems that the rectangular cross-sectional shape of the Ni nanowires seems to have no effect on the hysteresis loops of the Ni nanowires embedded in the InP membrane.

The very low remanence squareness of about 0.08 observed under an incidence angle $\alpha = 90°$ of the external magnetic field suggests that the magnetic moments are arranged perpendicular to the external magnetic field. The highest remanence squareness is found for $\alpha = 0°$. This suggests that the easy magnetization direction of the Ni nanowires is along the long axis $\boldsymbol{z}$ of the Ni nanowires. The alignment of the easy magnetization direction along $\boldsymbol{z}$ can be explained as a direct consequence of the ultra-high aspect ratio ($\approx$ 1000:1) of the Ni nanowires. The ultra-high aspect ratio of the Ni nanowires gives rise to the development of a highly pronounced shape anisotropy in the nanowires being one of the major quantities in determining the magnetic properties of the nanowire array. As an additional benefit, the slight {111}-texture of the Ni grains coincides with the easy magnetization direction of the Ni nanowires, so that both anisotropies add up.

The highest remanence squareness is found for the case that the external magnetic field and the easy magnetization direction of the nanowires are aligned in parallel ($\alpha = 0°$). The measured value of 0.36 is far smaller than for a single nanowire with the magnetization direction along the long wire axis $\boldsymbol{z}$ ($\boldsymbol{H} \parallel \boldsymbol{z}$) [96]. This behavior could result from the nucleation of domains with inverse magnetization direction at the root or at the end of the nanowire – the Ni nanowires are expected to be in a multidomain state due to the sufficiently large nanowire diameter. These domains with inverse magnetization direction would efficiently reduce stray fields and thus, explain the reduced remanence squareness.

Another possible explanation might be found in the magnetostatic interactions between neighboring Ni nanowires in the nanowire array. The energy of the magnetostatic interactions strongly depends on the distance between adjacent nanowires and increases with decreasing distance [97]. The increase is even stronger when the distance between two nanowires is in the order of the nanowire width. This suggests that the magnetostatic interactions of the Ni nanowires embedded in the InP membrane are rather strong, because the distance between adjacent nanowires (interwire distance: $\sim$ 100 nm) is only about half of the nanowire diameter width. The high magnetostatic interaction energy can be reduced by an antiparallel alignment of the magnetization direction in the nanowires as it was observed for Ni nanowires embedded in AAO membranes by magnetic force microscopy [19, 98].

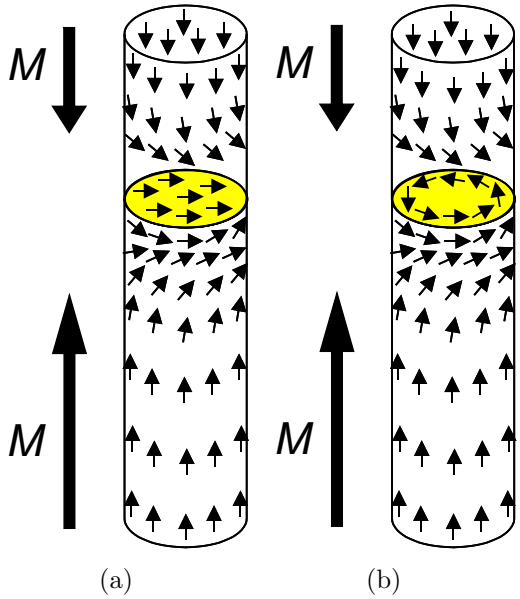

Figure 5.5: Schematic representation of a a) transverse and b) vortex wall.

As depicted in Fig. 4.18 d), the angular dependence of the coercivity exhibits an unusual behavior. One could expect to find the maximum coercivity at $\boldsymbol{H} \parallel \boldsymbol{z}$ and the minimum coercivity at $\boldsymbol{H} \perp \boldsymbol{z}$ as it is observed from the remanence squareness. The present angular dependence of the coercivity with a maximum at $\alpha = 45°$ could be explained by a combination of two magnetization reversal modes. These magnetization reversal modes could be e.g. the transversal and the vortex magnetization reversal mode [99]. These two reversal modes are depicted in Fig. 5.5.

The two peaks found in each branch of the differential susceptibility shown in Fig. 4.19 b) could be explained by two competing magnetization reversal mechanisms in the nanowires. In regime I, from $\alpha = 90°$ to $\alpha = 75°$, the magnetization reversal occurs primarily by reversal mechanism I. In regime II, from $\alpha = 0°$ to $\alpha = 30°$ (dotted line), the magnetization reversal occurs primarily by reversal mechanism II. In the transition regime from $\alpha = 45°$ to $\alpha = 60°$ the magnetization reversal seems to occur by a combination of both reversal mechanisms. Possibly, one could also determine the ratio of the nanowires that reverse their magnetization by mechanism I, resp. mechanism II by the lever rule in the transition regime.

The unusual behavior of the coercivity and the differential susceptibility of the Ni nanowires could be consistently described by the occurrence of two different reversal mechanisms that are predominant under certain incidence angles α of the external magnetic field. The type of magnetization reversal and which magnetization reversal mechanism is dominant in the two regimes could not be revealed by the performed magnetic measurements, but could be probably revealed by micromagnetic modeling of the Ni nanowire ensemble and comparison with the measured data.

Fe-Co based nanowires embedded in InP membrane

The Fe-Co based nanowires exhibit a very low remanence squareness of about 0.05 observed under an incidence angle $\alpha = 0°$ of the external magnetic field. This suggests that

the magnetic moments are arranged perpendicular to the external magnetic field. The highest remanence squareness is found for $\alpha = 90°$. This suggests that the easy magnetization direction of the Fe-Co based nanowires is aligned perpendicular to the long axis $\boldsymbol{z}$ of the nanowires. This preferential alignment of the easy magnetization direction perpendicular to $\boldsymbol{z}$ is also seen in the saturation field that is lowest for $\boldsymbol{H} \perp \boldsymbol{z}$, and the hysteresis losses that are highest for $\boldsymbol{H} \perp \boldsymbol{z}$. This arrangement of the easy magnetization direction is completely different from the one observed for the Ni nanowires (see Fig. 4.3.2). This magnetization alignment perpendicular to $\boldsymbol{z}$ could be explained as a direct consequence of a very high magnetocrystalline anisotropy of Fe_2O_3 [100]. The very high aspect ratio of the Fe-Co based nanowires of 400:1 gives rise to the development of a highly pronounced shape anisotropy in the nanowires that prefers an alignment of the easy magnetization direction along the nanowire axis. In the present case it seems that the shape anisotropy of the Fe-Co based nanowires is outreached by the high magnetocrystalline anisotropy of the Fe_2O_3 crystallites in the nanowires [100].

The low remanence squareness even for the case that the external magnetic field is applied along the easy magnetization direction ($\boldsymbol{H} \perp \boldsymbol{z}$) could be a result of the nucleation of domains with a reversed magnetization orientation to reduce stray fields.

The angular dependent coercivity of the Fe-Co based nanowires shows the lowest coercivity at $\alpha = 90°$ ($\boldsymbol{H} \perp \boldsymbol{z}$), as shown in Fig. 4.18 d). This means that the magnetization reversal is easiest perpendicular to the long wire axis $\boldsymbol{z}$. With decreasing angle α, the coercivity increases drastically reaching the maximum at $\alpha = 15°$. This increase and the minimum coercivity at $\alpha = 90°$ could be explained by an increased hindrance of the magnetization reversal, most probably due to the microstructure of the Fe-Co based nanowires. The decline in coercivity towards $\alpha = 0°$ could be explained by the occurrence of a second reversal mechanism that is preferably used for the magnetization reversal in the case of α smaller than 15°.

As depicted in Fig. 4.22 c), the Fe-Co based nanowires show only a single peak position in the differential susceptibility. The magnetization reversal occurs primarily by reversal mechanism I from $\alpha = 90°$ down to $\alpha = 30°$. With decreasing α, the reversal by mechanism I is more and more hindered. For $\alpha = 15°$ and $\alpha = 0°$, the peaks fade. This suggests that the magnetization reversal does not occur primarily by reversal mechanism I, but by a second reversal mechanism.

Similar to the Ni nanowires, the magnetization reversal types in the Fe-Co based nanowires could not be revealed based on the experimental data neither which reversal mechanism is dominant in the specific region.

5.4 Porous InP membranes as Li-ion battery anode

5.4.1 Anti-phase oscillations in the InP pore walls

The anti-phase oscillations in the pore wall width – as depicted in Fig. 4.26 – are very pronounced in the lithiated state of the anode and still detectable in the delithiated state. Generally, these self-induced anti-phase oscillations can be explained by a mechanism which combines the pressure neighboring pores exert on each other as a result of a lack of space due the volume expansion and a negative feedback for the Li-ion transport through the pore walls. A similar behavior with self-induced anti-phase oscillations in the pore

wall width was found for the growth of macropores in n-type Si [101]. The oscillations in anti-phase could be a clear hint for the periodic recovery of the Li-ion concentration in the pore wall and its surrounding neighbors.

Since only crystalline P based and In based Li alloy are found, one might speculate that the oscillations in the pore wall width shown in Fig. 4.26 are the result of a decomposition of InP into In_3Li_{13} and LiP.

5.4.2 Lithiation and delithiation reaction of porous InP

Comparing the XRD pattern of the lithiated porous InP anode – as shown in Fig. 4.28 a) – with the XRD patterns of the thin film anodes from [32, 33], one observes that two peak positions out of four are identical to the ones found by Cui, but there being assigned to In {111} and In{110}. This assignment to In is probably wrong, taking into account the tetragonal crystal structure and the lattice constant of In, which are $a = 0.325$ nm and $c = 0.495$ nm according to [102]. Instead these two peaks can be consistently assigned to In_3Li_{13} based on the data of [83]. The remaining two peaks assigned to InLi in [32, 33] are not found in the XRD pattern of the lithiated porous InP anode.

Besides crystalline In_3Li_{13} also two peaks are found in the XRD pattern of the lithiated porous InP anode that can be assigned to LiP. This is in good agreement with the findings of Pralong [103] where also only crystalline LiP was found in the lithiated state of a CoP_3 anode. For both InP thin film anodes no crystalline Li-P alloys could be identified, but the presence of Li_3P could be verified by XPS. Based on the results from the XRD pattern of the lithiated porous InP anode the lithiation reaction can be consistently written as:

$$3\,\mathrm{InP} + 16\,\mathrm{Li^+} + 16\,\mathrm{e^-} \longrightarrow \mathrm{In_3Li_{13}} + 3\,\mathrm{LiP} \tag{5.1}$$

This lithation reaction of the porous InP anode implies a Li storage of about 5.3 mol per mol of InP. This high Li storage is in good agreement with the observations found in [32].

Comparing the XRD pattern of the delithiated porous InP anode – as shown in Fig. 4.28 b) – with the XRD patterns of the thin film anodes from [32, 33], one observes that polycrystalline InP is found for the porous InP anode as well as for the InP thin film anode [33]. Additionally, crystalline In is found in case of the InP thin film anodes [32, 33], but not for the porous InP anode. Based on the results from the XRD pattern of the delithiated porous InP anode the delithiation reaction can be consistently written as:

$$\mathrm{In_3Li_{13}} + 3\,\mathrm{LiP} \longrightarrow 3\,\mathrm{InP(polycrystalline)} + 16\,\mathrm{Li^+} + 16\,\mathrm{e^-} \tag{5.2}$$

5.4.3 Cycling performance of the porous InP anode

As presented in section 4.4.3, the porous InP anode shows a good cycling performance till the seventh cycle.

The very high irreversible losses in the first cycle originate from the discharge limit in the first cycle. This means, the amount of Li associated to the gravimetric capacity of 160 mAh/g is still kept in the anode only reduced by the amount that was used for the formation of the SEI layer. Thus, it is not astonishing that no irreversible losses are observed in the second cycle simply because still Li is stored in the InP anode, so that

potential irreversible losses due to a continued SEI layer formation are compensated. Since for the first six cycles basically no fading of the gravimetric anode capacity is observed, the irreversible losses can be completely attributed to the formation of an SEI layer which itself is also an irreversible process. This matches very well with the results obtained from the cyclic voltammetry also showing the irreversibility of the SEI layer formation, presented in Fig. 4.29.

The strong fading starting in the eighth cycle could be due to a progressing detachment of the Au current collector from the InP anode due to the formation of an Au-Li alloy or due to the formation of crystalline InP during the delithiation. Thus, parts of the anode can not be charged and discharged anymore resulting in the observed fading of the gravimetric anode capacity. From cycle 8 the difference between irreversible losses and fading approaches a constant value of around 15 mAh/g. The origin of this constant loss could be assigned to ohmic losses in the anode.

Comparison with state of the art InP thin film anodes

Although the anode shows a good cycling performance without fading in the gravimetric capacity till the seventh cycle, the fading observed between cycle 7 and cycle 13 adds up to about 57 % of the original capacity (640 mAh/g). Comparing this result to the cycling performance of the InP thin film anode of Satya Kishore [32], one observes a capacity fading of 67 % of the initial gravimetric capacity after already 10 cycles when cycled at $C/5$ between 0.2 V and 1.5 V. The trend in the fading of the gravimetric capacity with increasing cycle number is similar to the one observed in the porous InP anode, referring to section 4.4.3, although the fading-free cycles are completely missing for the thin film anode.

The reduced gravimetric capacity fading could be understood by taking into account the impact of the cycling rate on the cycling stability of the anode. Typically, the cycling stability decreases if the cycling rate is increased, because the rather rapid volume expansion, resp. contraction due to the lithiation and delithiation results in higher mechanical stresses damaging or even destroying the structure of the anode. Thus, the reduced capacity fading compared to the thin film anode by Satya Kishore could be ascribed most probably to the 50 % reduced cycling rate.

The thin film InP anode of Cui [33] showed an even lower capacity fading of 42 % after 30 cycles compared to the porous InP anode. This good cycling stability can be explained by the extremely low charging / discharging rate used by Cui. The current density used for charging and discharging the porous InP anode, presented in this work, is more than a factor of 1000 higher compared to the current denisty used by Cui. Another important aspect of the thin film anodes on steel substrate is that this substrate takes part in the lithiation and delithiation process, as one can see in the XRD patterns presented in [33]. For this specific anode, the peak associated with the stainless steel substrate broadens and its position is shifted compared to the as-deposited state during the lithiation and delithiation and hence, influencing the gravimetric capacity and the cycling stability.

The gravimetric capacities given by [32, 33] are misleading, because the weight of the stainless steel substrate and additional binders are not taking into account. Therefore, the gravimetric capacity of these thin film InP anodes is by orders of magnitude lower compared to the here presented binder- and substrate-free porous InP anode.

The cycling stability of the porous InP anode might be further improved by adjusting

the voltage limits for the battery cycling. The work of Satya Kishore [32] is a clear hint that adjusted voltage limits are beneficial for the cycling performance. In the case of the here presented porous InP anode, raising the lower voltage limit above 0.2 V would prevent the formation of the Li-Au alloy and thus, excluding a possible reason for the capacity fading due to the partial delamination of the anode from the Au current collector. Decreasing the upper voltage limit down to 1.5 V or even lower could be beneficial, since the forced formation of crystalline InP is prevented, thus, reducing or even preventing mechanical stresses that could lead to a progressing damage of the anode. Besides the positive impacts, these limit adjustments have of course a big impact on the half cell voltage of the battery and thus, on the energy density of the anode.

5.4.4 Influence of the Al_2O_3 coating and the voltage limits on the anode performance

Lithiation and delithiation reaction

The cyclic voltammograms of the Al_2O_3 coated porous InP anode, shown in Fig. 4.31, suggest nearly the same lithiation and delithiation reaction as described in detail in section 5.4.2 for the uncoated porous InP anode, since the peak positions in the voltammograms are almost identical. The delithiation reaction is different from the one of the uncoated porous InP anode, because the formation of crystalline InP as final step of the delithiation is prevented due to the discharge voltage limit at 0.9 V. In addition, the delithiation of LiP is also partially hindered by this voltage limit.

Cycling performance of the porous coated anode

The cycling tests presented in Fig. 4.32 a) show that during the first two cycles of the coated porous InP anode only a small amount of charge can be stored in the anode. This can be understood if only the Al_2O_3 coating of the anode is lithiated and delithiated during cycling. Thus, the lithiation and delithiation of the InP pore walls is strongly hindered. The irreversible losses in the first two cycles can consequently be attributed to the formation of the SEI layer.

The jump in the gravimetric capacity up to about 250 mAh/g in the third cycle can be explained by the partial lithiation of the InP pore walls. This is possible as soon as a stable Li-Al_2O_3 phase is formed that allows for an indiffusion of excess Li ions through the Al_2O_3 layer into the InP pore wall [104]. Compared to the 800 mAh/g of the uncoated porous InP anode, the coated porous InP anode shows a highly reduced gravimetric capacity. This is most probably because the Al_2O_3 coating acts like a 'sausage' skin preventing the enclosed InP pore wall from free volume expansion during lithiation as it is observed for the uncoated porous InP anode. The observed partial delamination of the Al_2O_3 coating from the InP pore walls might be attributed to the volume expansion during lithiation.

The high irreversible losses may be attributed to the formation of LiP that is formed during lithiation, but is not completely delithiated, since the delithiation is stopped as soon as the voltage limit of 0.9 V is reached to prevent the formation of crystalline InP.

The subsequently decreasing gravimetric capacity from cycle 4 to 6 could be due to a cracking or partial delamination of the Al_2O_3 coating as explained above. The second abrupt increase in the gravimetric capacity after the stabilization in cycle 6 can be

understood in terms of a local extension of the volume expansion during lithiation. This assumption is supported by the absence of newly occurring high irreversible losses and the constant coulomb efficiency. The slightly higher irreversible losses can be assigned to a rebuilding / reorganization of the SEI layer at positions where the Al_2O_3 coating has detached from the InP pore walls.

The decreasing gravimetric capacity starting from cycle 7 till the complete failure of the anode can be subdivided into two sections due to the different origins of the capacity decline. In section I, ranging from cycle 7 to cycle 18, the trend of the slightly decreasing irreversible losses can be understood in terms of a reduction of the losses associated with the new formation of LiP during lithiation that is not delithiated afterwards due to the discharge voltage limit. This reduction is partially compensated by the linearly increasing fading. The origin of this fading may be found in the progressing detachment of active anode material accompanied by the formation of lateral cracks in the pore walls as observed in the SEM images of the anode after failure shown in Fig. 4.33 f).

Section II ranging from cycle 18 to the complete failure of the anode in cycle 30 is marked by the strong decay in the gravimetric capacity. The irreversible losses in this section are mostly due to fading, because both exhibit the same declining trend. The higher fading in the 30^{th} cycle is due to the complete failure of the anode. The decline in the coulomb efficiency from cycle 17 to 22 can be most probably assigned to a rebuilding / reorganization of the SEI layer. The gain in efficiency starting from cycle 23 is due to the decay of irreversible losses that are not related to the fading. The origin of this fading could be found in the local detachment of the anode from the current collector as observed in the SEM images of the anode after failure shown in Fig. 4.33 f).

Comparison to the uncoated porous InP anode The application of an Al_2O_3 coating of the porous InP anode allows for the formation of a stable SEI layer already in the first cycle at a lower voltage compared to the uncoated porous InP anode (1.08 V *vs.* 0.9 V with respect to the Li-metal cathode).

The coating prevents the formation of the bulging and necking structure of the pore walls during lithiation as found for the uncoated porous InP anode. This reduces the possibility for snagging of the pore walls and thus, for losses due to the rupture of bulged pore wall parts.

The Al_2O_3 coating and the charge/discharge voltage limit have a beneficial effect on the reduction of irreversible losses during cycling, but at the expense of a limitation of the gravimetric anode capacity. A thickness reduction of the Al_2O_3 coating could reduce the barrier for lithiation, but maintain the positive effect on the SEI layer. The increase of the discharge voltage limit from 0.9 V to about 1.1 V / 1.2 V would allow for an enhanced delithiation of LiP and thus, a strong gain in the gravimetric capacity, but probably still prevent the formation of crystalline InP.

Chapter 6

Summary & Outlook

In the present work a process for fabricating single-crystalline InP membranes was developed, characterized by *in situ* FFT-impedance spectroscopy and optimized for various structures.

The presented work describes the fabrication of single-crystalline InP membranes in a three-step fabrication process based on the self-organized formation of an almost perfectly hexagonally close-packed curro-pore array with a very high pore correlation length up to the fifth nearest neighbor. The membrane was formed by opening the curro-pore array from the bulk back side involving the formation and subsequent dissolution of a crysto-porous layer in a photo-electrochemical and purely photochemical etching process. The formation of the curro-pore array and the membrane fabrication process are performed in the same double cell preventing a misalignment of the sample between the process steps.

The photo-electrochemical and photochemical etching step were investigated by *in situ* FFT-IS. The measured impedance data could be described by a fit model consisting of a series resistor and an RC element. The fitted FFT-IS data allowed to identify characteristic stages in the photo-electrochemical (complete porosification of the bulk wafer back side etc.) and in the photochemical step (complete dissolution of the crysto-porous layer) as well as malfunctions during the etching process, e.g. by evolving gas bubbles. Besides the characterization of the process functionality, the FFT-IS also allows to predict the morphology of the membrane surface after completion of the etching process and for an easy adjustment of the etching parameters for the fabrication of membranes with arbitrary thicknesses.

The membrane itself can be customized in a large variety. The thickness of the membrane is freely adjustable between the natural limits of the wafer thickness and the mechanical stability of very thin membranes. The membrane surface can be tailored as well – from flat to cone-like pore opening, even up to a self-organized 3D-structured highly crysto-porous layer on the membrane back side with an ultra-high surface area. In addition, the pore shape can be tuned from elliptic to perfectly rectangular by post-etching under cathodic bias resulting even in the formation of InP nanowires. Beside the effect on the pore shape, the post-etching under cathodic bias results in a further reduction and homogenization of the pore wall width compared to the state after electrochemical etching of the curro-pore array. This further reduction in the pore wall width is accompanied by an increase in the resistivity of the membrane due to the increased SCR overlap within the InP pore walls. It has also been shown that it is possible to perform the cathodic post-etching with up to nine membranes in parallel which was necessary due

to the very long etching time of this process.

There is a huge field of possible applications for this kind of membrane. In this work the formation of a multifunctional composite consisting of the piezoelectric InP membrane and a magnetic filler and the usage as anode in Li-ion batteries have been investigated.

Multifunctional composites have been formed by galvanic deposition in InP pore arrays and membranes. The galvanic metal deposition in semiconductor pore arrays or membranes with very high and even ultra high aspect ratios (≈1000:1) is a very challenging task. It has been shown in this work that it is possible to grow dense Ni and Fe-Co based nanowires inside ultra-high aspect ratio InP membranes when depositing a thin dielectric Al_2O_3 interlayer by ALD prior to the galvanic deposition process. Without this dielectric interlayer it was only possible to grow porous Ni nanowires, resp. tubular-like structures in pore arrays due to the preferential nucleation of Ni crystallites on the InP pore walls. The galvanic growth of dense Ni nanowires has been characterized via FFT-IS. The measured impedance data could be described by a fit model consisting of a series resistor and a three *RC* elements. The fitted data could be separated into different stages and consistently interpreted by adsorption of boric acid on the growing Ni surface facilitating the Ni deposition, the Ni deposition reaction itself, and the increasing passivation of the Ni surface by a diffusion-limited species, probably Cl^-, counteracting the adsorption of boric acid molecules.

The magnetic characterization of the Ni and Fe-Co based nanowires showed that the easy magnetization direction of the Ni nanowires is along the long nanowire axis due to the ultra-high aspect-ratio of the nanowires giving rise to a pronounced shape anisotropy. In case of the Fe-Co based nanowires the easy magnetization direction is perpendicular to the long nanowire axis most probably due to the high magnetocrystalline anisotropy of the Fe_2O_3 component. In both cases the coercivity exhibited a maximum in between $\boldsymbol{H} \parallel \boldsymbol{z}$ and $\boldsymbol{H} \perp \boldsymbol{z}$, which could be explained by a combination of two magnetization reversal mechanisms that are each energetically favorable under certain angles α. This change in the reversal mechanism can be seen best for the Ni nanowires in the differential susceptibility curves where two characteristic peak positions are present in the transition region between both reversal mechanisms. In the region where each reversal mechanism is predominant only a single peak at the characteristic position is observed in the differential susceptibility curve. In case of the Fe-Co based nanowires only one peak position is observed that fades when the reversal mechanism changes. Especially the Fe-Co based nanowire / InP composite is of considerable interest for magnetoelectric sensors due to the higher magnetostriction coefficient and the alignment of the easy magnetization direction perpendicular to the long nanowire axis.

The application of porous InP membranes as anode in Li-ion batteries was successful. The anode concept exhibited a very high capacity per area and manages to work without any additives, binders or other passive materials such as a substrate material for mechanical support, unlike all other state of the art InP anodes. It was found that the pore walls undergo drastic structural changes during the lithiation reaction where InP is transformed into crystalline LiP and In_3Li_{13}. The structural changes become visible as oscillations in the pore wall widths in the form of a regular sequence of bulges and necks that are in anti-phase to neighboring pore walls. These anti-phase oscillation evolve most probably from the lack of space for the volume expansion and a negative feedback loop for the Li transport through the InP pore walls. These anti-phase oscillations are maintained in the delithiated state of the porous anode, when nanocrystalline InP is formed. The lithiation

and delithiation process is shown to be reversible with a Li storage of about 5.3 mol per mol InP. No delamination or large scale pulverization of the InP pore walls were observed indicating the capability of porous anodes to compensate for the high volume expansion during lithiation compared to bulk or thin film anodes. The cycling performance of the porous InP anode is good compared to other InP anode concepts. The anode showed no capacity losses in the first seven cycles, but a progressive degradation in the following cycles most probably due to detachments of anode parts from the Au current collector. The application of an 8 nm Al_2O_3 coating of the pore walls proved to be beneficial for the formation of the SEI layer around the pore walls evident from the cyclo voltammograms. The combination of the Al_2O_3 coating and the lower discharge voltage limit reduced the gravimetric capacity to less than 50 % of the uncoated anode, but had a beneficial effect on the cycling stability of the anode. Nevertheless, porous InP anodes cannot compete with state of the art Si microwire anodes in terms of price and also gravimetric capacity [105], but give interesting insights in the lithiation and delithitation mechanisms.

6.1 Outlook

Besides the presented results of this work, open questions remain, e.g. in the galvanic metal deposition process. The FFT-IS is a powerful tool to provide insight in the Ni deposition process and associated side reactions, but it does not allow to identify the chemical species, e.g. responsible for the passivation. This knowledge might be obtained indirectly from deposition experiments with modified electrolytes. This further knowledge could be used to understand and eventually fine-tune, e.g. the development of grain texture in the Ni nanowires and thus, also the magnetic properties.

The Ni nanowire / InP composite is currently investigated by synchrotron radiation under the application of an external magnetic field to investigate the impact of the magnetostriction of the Ni nanowires on the lattice parameters of the InP membrane. Especially, the Fe-Co based nanowire / InP composite needs to be further investigated with respect to the magnetoelectric properties of the composite due to the higher magnetostriction coefficient and the easy magnetization direction perpendicular to the long wire axis. For the application as a magnetoelectric composite sensor, it might be advantageous to use a softer magnetic metal, such as FeGa to reduce the saturation field and coercivity of the nanowires. One could also think of future applications in magnonics [106, 107].

In terms of the porous InP anode further work is needed to clarify the nature of the bulging and necking of the InP pore walls after complete lithiation, if it is e.g. the result of a self-organized phase separation in LiP and In_3Li_{13}. The exact degradation mechanism of the InP anode requires also further investigation, e.g. by FFT-IS, in order to understand how the cycling performance of porous anodes can be improved in detail. A different coating of the InP pore walls, e.g. with carbon to improve and stabilize the SEI layer, might be also beneficial for the cycling performance as well as an improved connection with the current collector, so that a delamination from the anode is prevented.

Beside the applications for single crystalline InP membranes presented in this work, possible further fields of application could be found in the field of biology where the highly versatile surface of InP membranes could be used to study the influence of the surface morphology on the adhesion of different cell types, such as nerve cells. In this context the piezoelectric properties of the InP membrane might be also of interest as an additional

free parameter. The InP membrane in combination with the crysto-porous layer offers an ultra-high surface area with a 3D structuring that might be of interest as substrate material for chemical sensors after suitable functionalization.

Appendix A

Galvanic deposition of magnetic nanostructures

In this section additional SEM images of the galvanically deposited nanostructures inside InP pore arrays and InP membranes, uncoated or coated with an Al_2O_3 interlayer, are presented.

Figure A.1 shows further images of the galvanically deposited Ni nanostructures (pulsed current deposition, $j = -20$ mA/cm^2, pulse length = 0.8 s, recovery time = 4.6 s, deposition time = 60 min) in an InP pore array (12 V for 1 s, 7 V for 1.5 min, 60 µm deep curro-pores, post-etching: 48 h, open circuit conditions).

Figure A.2 shows further images of the galvanically deposited porous Ni nanowires (pulsed current deposition, $j = -20$ mA/cm^2, pulse length = 1 s, recovery time = 4.6 s, deposition time = 60 min) in an InP membrane (17 V for 1 s, 8 V for 50 min, 340 µm membrane thickness, post-etching: 48 h, −1.0 V cathodic bias).

Figure A.3 shows further images of the galvanically deposited Ni nanowires (galvanostatic deposition, $j = -17$ mA/cm^2, deposition time = 120 min) in an InP membrane (17 V for 1 s, 10 V for 41 min, 340 µm membrane thickness, post-etching: 1060 min, −0.8 V cathodic bias) coated with an 8 nm Al_2O_3 layer.

Figure A.4 shows further images of the galvanically deposited Fe-Co based nanowires (pulsed current deposition, $j = -15$ mA/cm^2 for 0.8 s, $j = -5$ mA/cm^2 for 4.6 s, deposition time = 120 min) in an InP membrane (15 V for 1 s, 8 V for 22 min, 240 µm membrane thickness, post-etching: 48 h, −0.8 V cathodic bias) coated with an 8 nm Al_2O_3 layer.

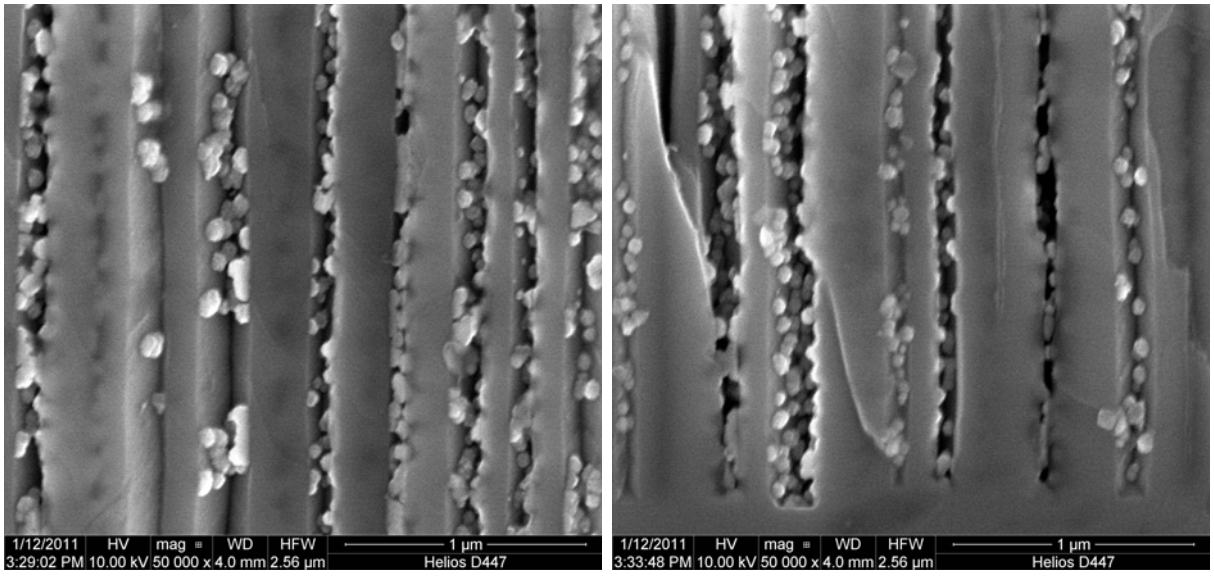

(a) (b)

Figure A.1: Cross-sectional SEM view on the Ni nanoparticles embedded in an InP pore array at a) half of the pore depth and b) the pore tips. No preferential deposition at the pore tips is observed. The wall coverage with Ni particles is homogeneous along the entire pore depth. The Ni particles show an average size of about 50 nm and tend to form partially interconnected structures.

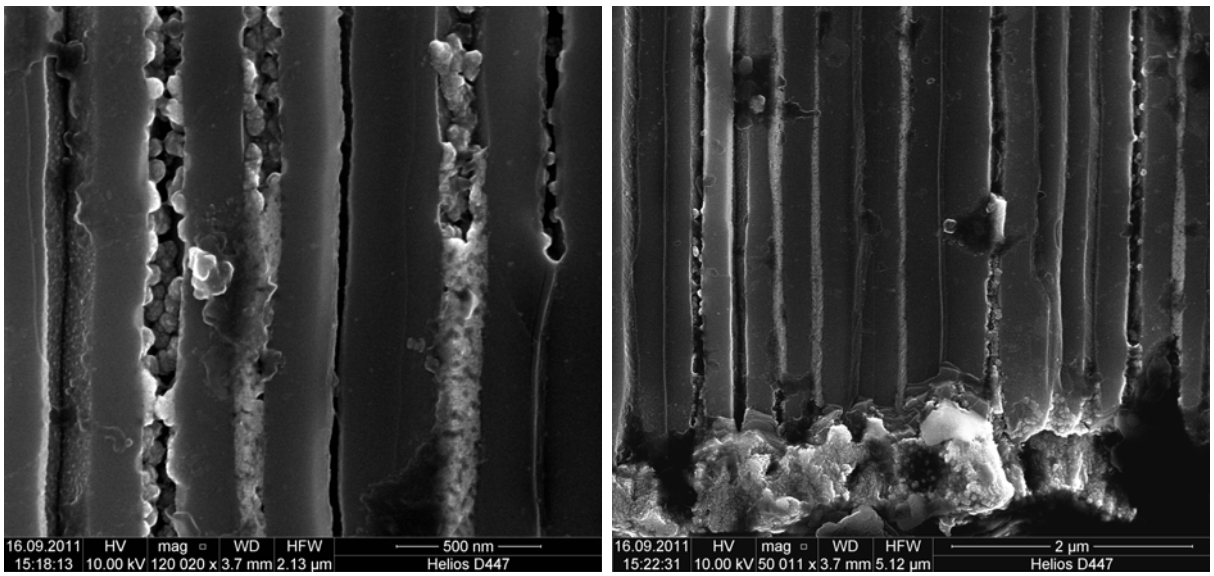

(a) (b)

Figure A.2: Cross-sectional SEM view on the porous Ni nanowires embedded in an InP membrane at a) a middle position and b) at the plating base.The porous Ni nanowires consist of single Ni particles deposited on the pore walls. Interconnected Ni particles form an almost closed outer shell. The inside of the nanowires consists of voids.

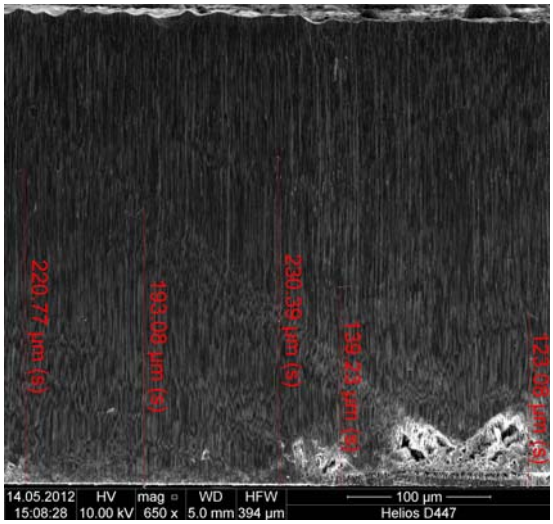

(a)

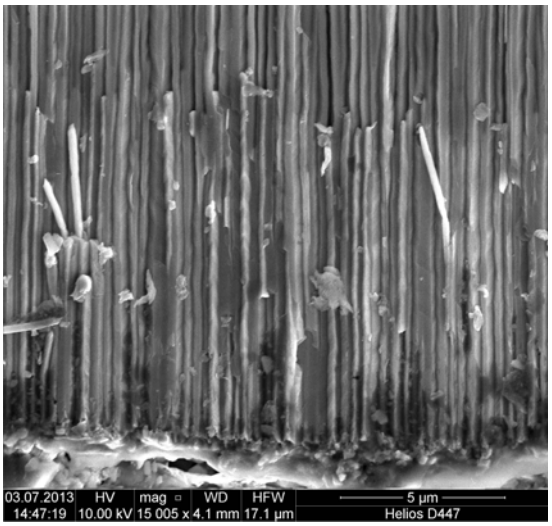

(b)

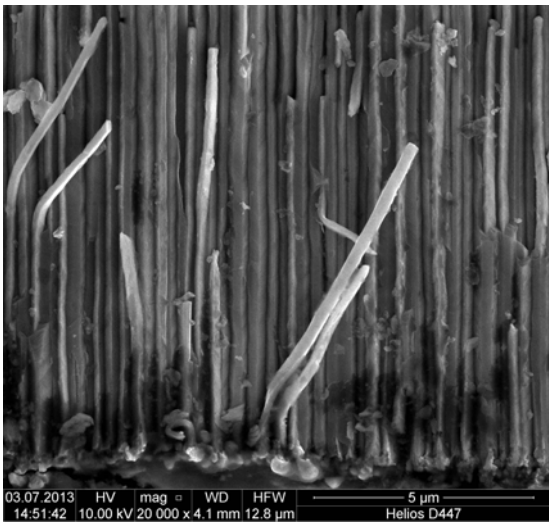

(c)

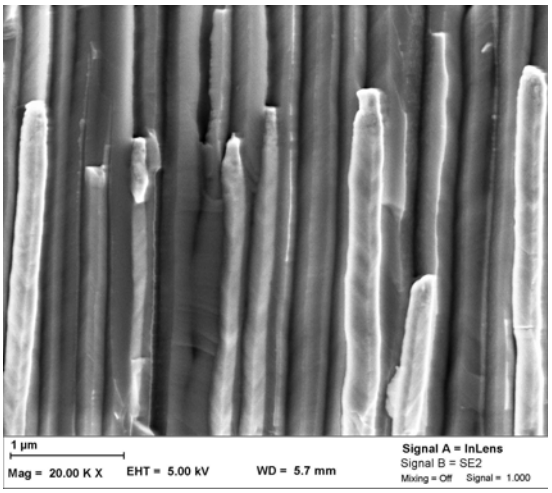

(d)

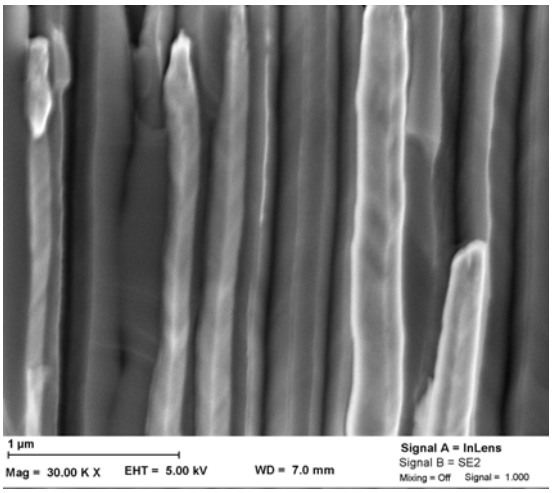

(e)

Figure A.3: Cross-sectional SEM view on the Ni nanowires embedded in an Al_2O_3 coated InP membrane a) over the entire membrane (partial membrane break-off due to sample cleavage), at the b) plating base, c) plating base at a different position, and at about d) half of the pore depth, e) half of the pore depth at a different position.

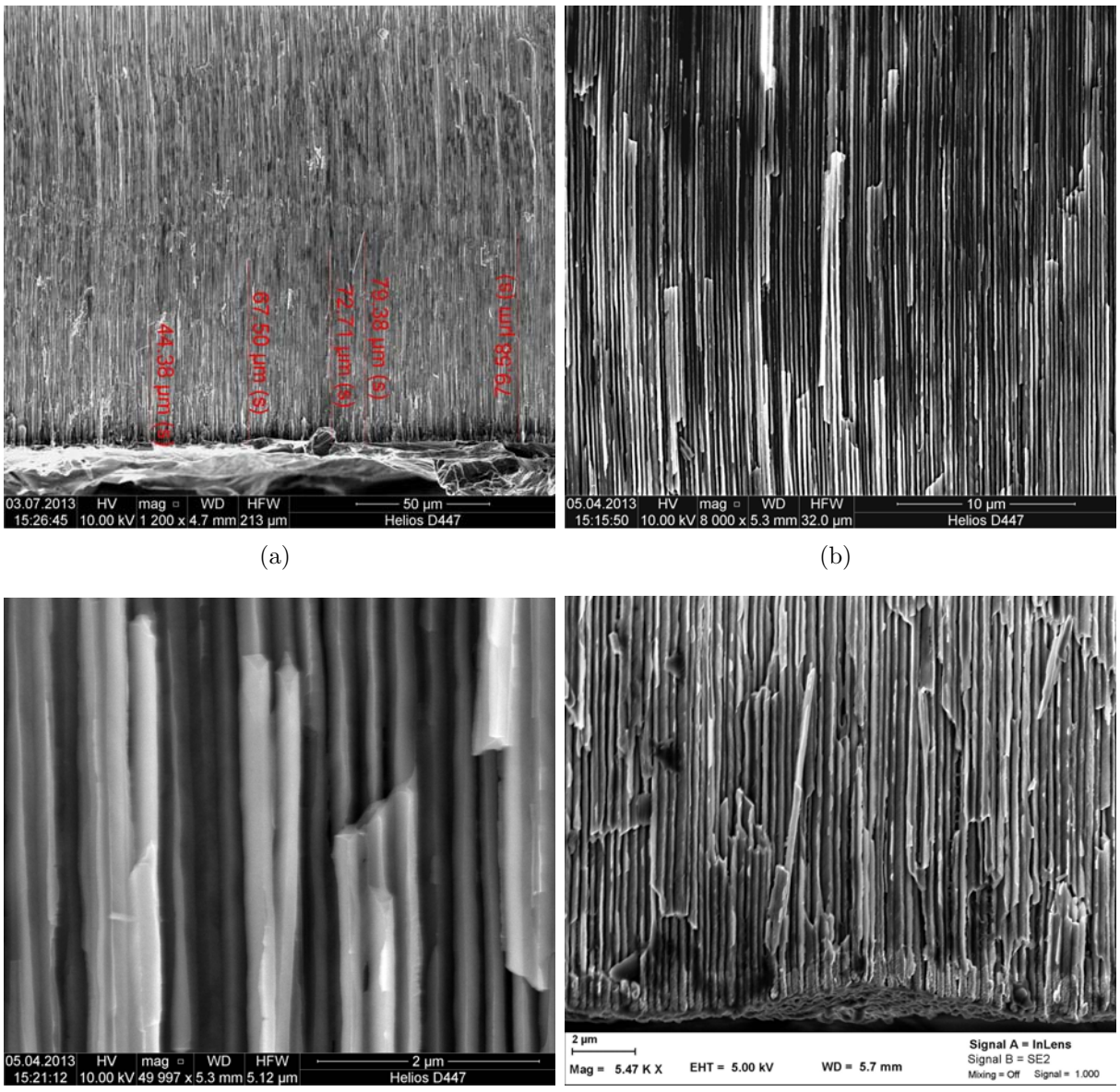

Figure A.4: Cross-sectional SEM view on the porous Fe-Co based nanowires embedded in an Al_2O_3 coated InP membrane a) over almost the complete membrane, at a about b) half of the pore depth, c) half of the pore depth in higher magnification, and at the d) plating base.

Bibliography

[1] V. Lehmann and H. Föll. Formation mechanism and properties of electrochemically etched trenches in n-type silicon. *J. Electrochem. Soc.*, 137(2):653–659, 1990.

[2] V. Lehmann and U. Gösele. Porous silicon formation: a quantum wire effect. *Appl. Phys. Lett.*, 58(8):856–858, 1991.

[3] L.T. Canham. Silicon quantum wire array fabrication by electrochemical and chemical dissolution of wafers. *Appl. Phys. Lett.*, 57(10):1046–1048, 1990.

[4] S. Langa, J. Carstensen, I.M. Tiginyanu, and H. Föll. Nucleation and growth of macro pores on (100) n-type Ge. *Phys. Status Solidi C*, 2(9):3237, 2005.

[5] E. Garralaga Rojas, J. Hensen, J. Carstensen, H. Föll, and R. Brendel. Lift-off of porous germanium layers. *J. Electrochem. Soc.*, 158(6):D408–D411, 2011.

[6] E. Monaico, I.M. Tiginyanu, V.V. Ursaki, A. Saruna, M. Kuball, D.D. Nedeoglo, and V.P. Sirkeli. Photoluminescence and vibrational properties of nanostructured ZnSe templates. *Semicond. Sci. Technol.*, 22:1115–1121, 2007.

[7] J.P. Krumme and M.E. Straumanis. Anodic behavior of GaAs single crystals at increased current densities in alkaline and acidic solutions. *Trans. Met. Soc. AIME*, 239:395, 1967.

[8] T. Takizawa, S. Arai, and M. Nakahara. Fabrication of vertical and uniform-size porous InP structure by electrochemical anodization. *Japan J. Appl. Phys.*, 33(2, 5A):L643–L645, 1994.

[9] M. Leisner, J. Carstensen, and H. Föll. Pores in n-type InP - a model system for electrochemical pore etching. *Nanoscale Res. Lett.*, 5(7):1190–1194, 2010.

[10] M. Leisner, D. Dorow-Gerspach, J. Carstensen, and H. Föll. Influence of the doping concentration on crystallographic pore growth on n-type InP and GaAs. *Phys. Status Solidi A*, 208(6):1378–1382, 2011.

[11] L. Santinacci, M. Bouttemy, I. Gerard, and A. Etcheberry. Unexpected Dissolution Process at Porous n-InP Electrodes. *ECS Trans.*, 19(3):313, 2009.

[12] K. Radhanpura, S. Hargreaves, R.A. Lewis, L. Sirbu, and I.M. Tiginyanu. Heavy noble gas (Kr, Xe) irradiated (111) InP nanoporous honeycomb membranes with enhanced ultrafast all-optical terahertz emission. *Appl. Phys. Lett.*, 97:181921, 2010.

[13] M. Leisner, J. Carstensen, A. Cojocaru, and H. Föll. Pore growth on n-InP investigated by in situ FFT impedance spectroscopy. *Phys. Status Solidi C*, 206(7):1566–1570, 2009.

[14] Z. Weng, A. Liu, Y. Sang, J. Zhang, Z. Hu, Y. Liu, and W. Liu. Anodic etching of InP using neutral NaCl electrolyte. *J. Porous Mater.*, 16:707, 2009.

[15] C. O'Dwyer, D.N. Buckley, and S.B. Newcomb. Simultaneous observation of current oscillations and porous film growth during anodization of InP. *Langmuir*, 21(18):8090, 2005.

[16] C. O'Dwyer, D.N. Buckley, D. Sutton, and S.B. Newcomb. Anodic formation and characterization of nanoporous InP in aqueous KOH electrolytes. *J. Electrochem. Soc.*, 153(12):G1039–G1046, 2006.

[17] M. Leisner, J. Carstensen, A. Cojocaru, and H. Föll. In-situ FFT impedance spectroscopy during the growth of crystallographically oriented pores in InP. *ECS Trans.*, 16(3):133–142, 2008.

[18] H. Masuda and F. Fukuda. Ordered metal nanohole arrays by a two-step replication of honeycomb structures of anodic alumina. *Science*, 268:1466, 1995.

[19] K. Nielsch, R.B. Wehrspohn, J. Barthel, J. Kirschner, S.F. Fischer, H. Kronmüller, T. Schweinböck, D. Weiss, and U. Gösele. High density hexagonal nickel nanowire array. *J. Magn. Magn. Mater.*, 249:234, 2002.

[20] P. Göring, E. Pippel, H. Hofmeister, R.B. Wehrspohn, M. Steinhart, and U. Gösele. Gold/carbon composite tubes and gold nanowires by impregnating templates with hydrogen tetrachloroaurate/acetone solutions. *Nano Letters*, 4(6):1121, 2004.

[21] P.D. McGary, L. Tan, J. Zou, B.J.H. Stadler, P.R. Downey, and A.B. Flatau. Magnetic nanowires for acoustic sensors (invited). *J. Appl. Phys.*, 99:08B310, 2006.

[22] C. Fang, E. Foca, S. Xu, J. Carstensen, and H. Föll. Deep silicon macropores filled with copper by electrodeposition. *J. Electrochem. Soc.*, 154(1):D45–D49, 2007.

[23] H. Föll, M.-D. Gerngross, A. Cojocaru, M. Leisner, J. Bahr, and J. Carstensen. How to make single small holes with large aspect ratios. *Phys. Status Solidi RRL*, 3(2):55–57, 2009.

[24] P. Granitzer, K. Rumpf, P. Pölt, A. Reichmann, and H. Krenn. Self-assembled mesoporous silicon in the crossover between irregular and regular arrangement applicable for Ni filling. *Physica E*, 38:205, 2007.

[25] K. Rumpf, P. Granitzer, P. Pölt, S. Simic, and H. Krenn. Ferromagnetic nanoparticles embedded in self-arranged matrices. *Phys. Status Solidi A*, 205(6):1354, 2008.

[26] A.L. Dolgiy, S.V. Redko, I. Komissarow, V.P. Bondarenko, K.I. Yanushkevich, and S.L. Prischepa. Structural and magnetic properties of Ni nanowires grown in mesoporous silicon templates. *Thin solid films*, page DOI: 10.1016/j.tsf.2013.01.049, 2013.

[27] C. Fang, E. Foca, L. Sirbu, J. Carstensen, I.M. Tiginyanu, and H. Föll. Formation of metal wire arrays via electrodeposition in pores of Si, Ge and III-V semiconductors. *Phys. Status Solidi A*, 204(5):1388, 2007.

[28] I. Tiginyanu, E. Monaico, and E. Monaico. Ordered arrays of metal nanotubes in semiconductor envelope. *Electrochem. Comm.*, 10(5):731, 2008.

[29] C.K. Chan, H. Peng, G. Liu, K. McIlwrath, X.F. Zhang, R.A. Huggins, and Y. Cui. High-performance lithium battery anodes using silicon nanowires. *Nat. Nanotechnol.*, 3(1):31–35, 2008.

[30] H. Föll, H. Hartz, E.K. Ossei-Wusu, J. Carstensen, and O. Riemenschneider. Si nanowires arrays as anodes in Li ion batteries. *Phys. Status Solidi RRL*, 4(1):4–6, 2010.

[31] Y. Lu, J.P. Tu, C.-D. Gu, X.-L. Wang, and S.X. Mao. In situ growth and electrochemical characterization versus lithium of a core/shell-structured Ni2P@C nanocomposite synthesized by a facile organic-phase strategy. *J. Mater. Chem.*, 21:17988–17997, 2011.

[32] M.V.V.M. Satya Kishore and U.V. Varadaraju. Phosphides with zinc blende structure as anodes for lithium-ion batteries. *J. Power Sources*, 328:594–597, 2006.

[33] Y.-H. Cui, M.-Z. Xue, X.-L. Wang, K. Hu, and Z.-W. Fu. Inp as new anode material for lithium ion batteries. *Electrochem Commun.*, 11:1045–1047, 2009.

[34] T.P. Pearsall. *Properties, processing and applications of indium phosphide*. IEEE, London, 2000.

[35] H.C. Gatos and M.C. Lavine. Characteristics of the (111) surfaces of the III-V intermetallic compounds. *J. Electrochem. Soc.*, 108(7):645–649, 1960.

[36] H. Gerischer and W. Mindt. The mechanisms of the decomposition of semiconductors by electrochemical oxidation and reduction. *Electrochim. Acta*, 13(6):1329–1341, 1968.

[37] C. Kaneshiro, T. Sato, and H. Hasegawa. Electrochemical etching of indium phosphide surfaces studied by voltammetry and scanned probe microscopes. *Jpn. J. Appl. Phys*, 2B(38):1147–1152, 1999.

[38] M. Christophersen, J. Carstensen, K. Voigt, and H. Föll. Organic and aqueous electrolytes used for etching macro- and mesoporous silicon. *Phys. Status Solidi A*, 197(1):34–38, 2003.

[39] M. Dionizio Moreira, P. Venezuela, and T.M. Schmidt. The effects of oxygen an the surface passivation of InP nanowires. *Nanotechnology*, 19:065203, 2008.

[40] Z.H. Lu, T. Tyliszczak, and A.P. Hitchcock. Structure of Cl-passivated GaAs(111) surface. *Phys. Rev. B*, 58(20):13 820, 1998.

[41] E. Spiecker, M. Rudel, W. Jäger, M. Leisner, and H. Föll. Morphology, interface polarity and branching of electrochemically etched pores in InP. *Phys. Status Solidi A*, 202(15):2950–2962, 2005.

[42] S. Langa. *Electrochemical pore etching in III-V compounds*. Dissertation, Christian-Albrechts-Universität zu Kiel, 2004.

[43] M. Christophersen, J. Carstensen, S. Rönnebeck, C. Jäger, W. Jäger, and H. Föll. Crystal orientation dependance and anisotropic properties of macropore formation of p- and n-type silicon. *J. Electrochem. Soc.*, 148(6):E267–E275, 2001.

[44] A.I. Belogorokhov, V.A. Karavanskii, A.N. Obraztsov, and V.Yu. Timoshenco. Intense photoluminescence in porous gallium phosphide. *JETP Lett.*, 60:264, 1994.

[45] I.M. Tiginyanu, E. Monaico, S. Albu, and V.V. Ursaki. Environmentally friendly approach for nonlithographic nanostructuring of materials. *Phys. Status Solidi RRL*, 1(3):98, 2007.

[46] E. Kikuno, M. Amiotti, T. Takizawa, and S. Arai. Anisotropic refractive index of porous InP fabricated by anodization of (111)A surface. *Japan J. Appl. Phys.*, 34(1, 1):177–178, 1995.

[47] R.B. Wehrspohn, J. Schilling, J. Choi, Y. Luo, S. Matthias, S. Schweizer, F. Müller, U. Gösele, S. Lölkes, S. Langa, J. Carstensen, and H. Föll. *Electrochemically-perpared 2D and 3D photonic crystals*. Wiley-VCH, Weinheim, 2004.

[48] M. Leisner, J. Carstensen, and H. Föll. Quantitative analysis of curro pore growth on n-type InP. *Phys. Status Solidi C*, 8(6):1923–1927, 2011.

[49] M.A. Stevens-Kalceff, I.M. Tiginyanu, S. Langa, and H. Föll. Correlation between morphology and cathodoluminescence in porous GaP. *J. Appl. Phys.*, 89(5):2560–2565, 2001.

[50] E. Monaico, V.V. Ursaki, A. Urbieta, P. Fernández, J. Piqueras, R.W. Boyd, and I.M. Tiginyanu. Porosity-induced gain of luminescence in CdSe. *Semicond. Sci. Technol.*, 19(12):L121–L123, 2004.

[51] P. Atkins and J.D. Paula. *Physical chemistry, 9th*. Oxford University Press, New York, 2010.

[52] D.L. Chapman. A contribution to the theory of electrocapillarity. *Phil. Mag.*, 25:475–481, 1913.

[53] J.R. MacDonald. *Impedance spectroscopy*. John Wiley & Sons, 1987.

[54] P. Scherrer. Bestimmung der Größe und der inneren Struktur von Kolloidteilchen mittels Röntgenstrahlen. *Nachrichten von der Gesellschaft der Wissenschaften zu Göttingen, Mathematisch-Physikalische Klasse*, 1918:98, 1918.

[55] B.D. Cullity. *Elements of x-ray diffraction*. Addison-Wesley, Reading, 1978.

[56] N. Kanani. *Galvanotechnik – Grundlagen, Verfahren, Praxis.* Karl Hanser Verlag München Wien, 2000.

[57] O.P. Watts. Rapid nickel plating. *Trans. Am. Electrochem. Soc.*, 29:395–403, 1916.

[58] K. Nielsch, F. Müller, A.-P. Li, and U. Gösele. Uniform nickel deposition into ordered alumina pores by pulsed electrodeposition. *Adv. Mater.*, 12(8):582, 2000.

[59] D.H. Qin, L. Cao, Q.Y. sun, Y. Huang, and H.L. Li. Fine magnetic properties obtained in FeCo alloy nanowire arrays. *Chem. Phys. Lett.*, 358:484–488, 2002.

[60] L. Cao, X. Qiu, J. Sing, H. Li, and L.Chen. The effects of composition and thermal treatment on the magnetic properties of $Fe_{100-x}Co_x$ nanowire arrays based on AAO templates. *J. Mater. Sci.*, 41:2211–2218, 2006.

[61] R. Hilzinger and W. Rodewald. *Magnetic Material – Fundamentals, Products, Properties, Application.* Publicis Publishing, Erlangen, 2013.

[62] H.Singh Nalwa. *Handbook of thin films: deposition and processing.* Academic Press, San Diego, 2002.

[63] B.D. Cullity and C.D. Graham. *Introduction to magnetic materials.* John Wiley & Sons, Hoboken, 2009.

[64] J.M.D. Coey. *Magnetism and magnetic materials.* Cambridge University Press, Cambridge, 2010.

[65] E.C. Stoner and E.P. Wohlfarth. A mechanism of magnetic hysteresis in heterogeneous alloys. *Phil. Trans. R. Soc. Lond. A*, 240:599–642, 1948.

[66] R. Hertel and J. Kirschner. Magnetization reversal dynamic in nickel nanowires. *Physica B*, 343:206–2010, 2004.

[67] M. Kläui and C.A. Fernandes Vaz. *Magnetization configurations and reversal in small magnetic elements*, pages 881–916. John Wiley & Sons, 2007.

[68] T. Reddy and D. Linden. *Linden's Handbook of Batteries.* McGraw Hill, United States of America, 2011.

[69] A. Jossen and W. Weydanz. *Moderne Akkumulatoren richtig einsetzen.* Reichardt Verlag, Untermeitingen, 2006.

[70] K. Xu. Nonaqueous liquid electrolytes for lithium-based rechargeable batteries. *Chem. Rev.*, 104:4303–4417, 2004.

[71] P. Arora and R.E. White. Capacity fade mechanisms and side reactions in lithium-ion batteries. *J. Electrochem. Soc.*, 145(10):3647–3667, 1998.

[72] D.-T. Shieh, J. Yin, K. Yamamoto, M. Wada, S. Tanase, and T. Sakai. Surface characterization on lithium insertion/deinsertion process for sputter-deposited AgSn thin-film electrodes by XPS. *J. Electrochem. Soc.*, 153(1):A106–A112, 2006.

[73] V. Agubra and J. Fergus. Lithium ion battery anode aging mechanisms. *Materials*, 6:1310–1325, 2013.

[74] S. Mishra, N. Liu, J. Nelson, S.S. Hong, Y. Cui, and M.F. Toney. In situ x-ray diffraction studies of (de)lithiation mechanism in silicon nanowire anodes. *ACS Nano*, 6(6):5465–5473, 2012.

[75] S. Foner. Versatile and sensitive vibrating-sample magnetometer. *Rev. Sci. Instrum.*, 30(7):548, 1959.

[76] E. Gileadi. *Physical Electrochemistry.* Wiley-VCH Verlag GmbH & Co. KGaA, Weinheim, 2011.

[77] M.-D. Gerngross. *Characterization and optimization of electrochemically etched porous indium phosphide structures for possible piezoelectric applications.* Masterthesis, Universität Kiel, 2010.

[78] M. Leisner. *Untersuchung und Modellierung des elektrochemischen Porenwachstums in InP mit In-situ-FFT-Impedanzspektroskopie und Monte-Carlo-Simulation.* Doktorarbeit, Universität Kiel, 2011.

[79] S. Langa, I.M. Tiginyanu, J. Carstensen, M. Christophersen, and H. Föll. Formation of porous layers with different morphologies during anodic etching of n-InP. *Electrochem. Solid-State Lett.*, 3(11):514–516, 2000.

[80] L. Barrientos, S. Rodriguez-Llamazares, J. Merchani, P. Jara, N. Yutronic, and V. Lavayen. Unveiling the structure of Ni/Ni oxide nanoparticles system. *J. Chil. Chem. Soc.*, 54(4):391–393, 2009.

[81] J. Staun Olsen, C:S:G: Cousins, L. Gerward, H. Jhans, and B.J. Sheldon. A study of the crystal structure of Fe_2O_3 in the pressure range up to 65 GPa using syncrotron radiation. *Physica Scripta*, 43:327–330, 1991.

[82] I.D. Belova, Y.E. Roginskaya, and Y.N. Venevtsev. Crystal and electronic structure of non-stoichiometri $Co_{3-X}O_4$ films. *Russ. J. Inorg. Chem.*, 28(12):1706–1709, 1983.

[83] J. Stöhr, W. Müller, and H. Schäfer. Darstellung und Kristallstruktur von Li_2In und $Li_{13}In_3$. *Z. Naturforsch.*, B 33:1434, 1978.

[84] W. Honle and H. von Schnering. Zur Struktur von LiP und KSb. *Z. Kristallogr.*, 155:307, 1981.

[85] R. Alcantara, J.L. Tirado, J.C. Jumas, L. Monconduit, and J. Olivier-Fourcade. Electrochemical reaction of lithium with CoP_3. *J. Power Sources*, 109:308, 2002.

[86] B. Leon, J.I. Corredor, J.L. Tirado, and C. Perez-Vicentez. On the mechanism of the electrochemical reaction of tin phosphide with lithium. *J. Electrochem. Soc.*, 153:A1829, 2006.

[87] B. Laik, L. Eude, J.P. Pereira-Ramos, C. Sorin Cojocaru, D. Pribat, and E. Rouvière. Silicon nanowires as negative electrode for lithium-ion microbatteries. *Electrochem. Acta*, 53:5528–5532, 2008.

[88] C.K. Chan, R. Ruffo, S.S. Hong, R.A. Huggins, and Y. Cui. Structural and electrochemical study of the reaction of lithium with silicon nanowires. *J. Power Sources*, 189:34–39, 2009.

[89] H.-G. Ahn, H.-J. Sohn, and T. Kang. Electrochemical characteristics of indium phosphide negative electrode for lithium ion secondary batteries. In *Proceedings, 202nd meeting of the electrochemical society*, Salt Lake City, USA, 20-24 October 2002.

[90] C.-M. Park, J.-H. Kim, H. Kim, and H.-J. Sohn. Li-alloy based anode materials for Li secondary batteries. *Chem. Soc. Rev.*, 39:3115–3141, 2010.

[91] E. Quiroga-González, J. Carstensen, and H. Föll. Good cycling performance of high-density arrays of Si microwires as anodes for Li ion batteries. *Electrochim. Acta*, 101:93–98, 2013.

[92] E. Chassaing, M. Joussellin, and R. Wiart. The kinetics of nickel electrodeposition inhibition by adsorbed hydrogen and anions. *J. Electroanal. Chem.*, 157:75–88, 1983.

[93] C.E. Davalos, J.R. Lopez, H. Ruiz, A. Mendez, R. Antano-Lopez, and G. Trejo. Study of the role of boric acid during the electrochemical deposition of Ni in a sulfamate bath. *Int.J.Electrochem.Sci.*, 8:9785–9800, 2013.

[94] J.P. Hoare. On the role of boric acid in the Watts bath. *J. Electrochem. Soc.*, 133(12):2491–2494, 1986.

[95] R. Wiart. Elementary steps of electrodeposition analysed by means of impedance spectroscopy. *Electrochim. Acta*, 35(10):1587–1593, 1990.

[96] D.-L. Sun, J.-H. Gao, X.-Q. Zhang, Q.-F.Zhan, W. He, Y. Sun, and Z.H. Cheng. Contribution of magnetostatic interaction to magnetization reversal of Fe_3Pt nanowires arrays: A micromagnetic simulation. *J. Magn. Magn. Mater.*, 321(18):2737–2741, 2009.

[97] D. Vokout, M. Beleggia, L. Heller, and P. Sittner. Magnetostatic interaction and forces between cylindrical permanent magnets. *J. Magn. Magn. Mater.*, 321:3758–3763, 2009.

[98] K. Nielsch, R. Hertel, R.B. Wehrspon, J. Barthel, J. Kirschner, U. Gösele, S.F. Fischer, and H. Kronmüller. Switching behavior of single nanowires inside dense nickel nanowire arrays. *IEEE Trans. Magn.*, 38(5):2571–2573, 2002.

[99] N. Han, G. Guo, L. Zhang, G. Zhang, and W. Song. Magnetization reversal for Ni nanowires studied by micromagnetic simulations. *J. Mater. Sci. Technol.*, 25(2):151, 2009.

[100] L. Machala, J. Tucek, and R. Zboril. Polymorphous transformation of nanometric iron(III) oxide: a review. *Chem. Mater.*, 23:3255–3272, 2011.

[101] A. Cojocaru, J. Carstensen, M. Leisner, H. Föll, and I.M. Tiginyanu. Self-induced oscillation of the macropore diameter in n-type silicon. *Phys. Status Solidi C*, 206(7):1533–1535, 2009.

[102] S.S. Oh, D.H. Kim, M.W. Moon, A. Vaziri, M. Kim, E. Yoon, K.H. Oh, and J.W. Hutchinson. Indium nanowires synthesized at an ultrafast rate. *Adv. Mater.*, 20:1093, 2008.

[103] V. Pralong, D.C.S. Souza, K.T. Leung, and L.F. Nazar. Reversible lithium uptake by CoP_3 at low potential: role of the anion. *Electrochem. Commun.*, 4:516, 2002.

[104] S.C. Jung and Y.-K. Han. How do Li atoms pass through the Al_2O_3 coating layer during lithiation in Li-ion batteries? *J. Phys. Chem. Lett.*, 16(4):2681–2685, 2013.

[105] E. Quiroga-González, J. Carstensen, and H. Föll. Structural and electrochemical investigation during the first charging cycles of silicon microwire array anodes for high capacity lithium ion batteries. *Materials*, 6:626–636, 2013.

[106] G. Gubbiotti, S. Tacchi, M. Madami, . Carlotti, A.O. Adeyeye, and M. Kostylev. Brillouin light scattering studies of planar metallic magnonic crystals. *J. Phys.D: Appl. Phys.*, 43(26):264003, 2010.

[107] J. Topp, D. Heitman, M.P. Kostylev, and D. Grundler. Making a reconfigurable artificial crystal by ordering bistable magnetic nanowires. *Phys. Rev. Lett.*, 104(20):207205, 2010.

Acknowledgement

At this point, I would like to say thank you to all of those, who contributed to the success of this work.

First, I would like to thank Prof. Dr. Helmut Föll for the opportunity to do my research in the framework of the collaborative research center "SFB 855 – *Magnetoelectric composites – future biomagnetic interfaces*". It means a lot to me that you made it possible for me to present my research on several international conferences all around the world. The experience of teaching was a good and important experience for me, both from the scientific, but also from the human perspective. In summary, it was a pleasure to work in your research group.

Special thanks also to Dr. Jürgen Carstensen for his excellent scientific support, guidance and the extensive discussions during the time of my research. Especially the discussions with you pushed me really forward and provided lots of new insights and ideas for me.

Another special thanks to Dr. Enrique Quiroga-Gonzalez for his great help in the conduction and analysis of the battery experiments as well as for the discussions. I will miss our collaborations in the future. Good luck for your future, back in Mexico!

I cordially thank Prof. Dr. Jeffrey McCord and Dr. habil. Georgi Popkirov for the fruitful discussions where you shared a part of your experience in your research field with me.

I would also like to thank Dipl.-Ing. Jörg Bahr for his excellent technical support in the lab. You made all my requests for changes in the cell design etc. come true which was very important for the success of this work.

Many thanks also to Dr. Jan-Martin Wagner for the longtime teaching cooperation, proof-reading and lessons about grammar and orthography in general and the proper use of dashes and hyphens. These, – -, are for you.

I want to thank Dr. Steffen Chemnitz for the Al_2O_3 coating of my sample by ALD, which turned out to be one of the decisive steps for the successful metal deposition in the InP membranes.

I would also like to thank Katrin Brandenburg for her great help in managing all administrative things from proof-reading over travel planning and accounting, keeping all bureaucracy away from me.

I would like to thank my colleagues in the office, Dr. Jan-Martin Wagner, Dipl.-Ing. Andreas Schütt, M.Sc. Emmanuel Ossei-Wusu, M.Sc. Sandra Nöhren, and M.Sc. Melike Baytekin-Gerngroß, and my former colleagues Dr. Ala Cojacaru, Dr. Malte Leisner and Dipl.-Ing. Anselm Pape for the nice working atmosphere with lots of chats about all kinds of topics that enriched the working hours in the lab and in the office. Furthermore, I would like to thank all my colleagues from the SFB 855 for the good cooperation and

amusing time at our status seminars.

I would like to acknowledge also the funding of the German Science foundation (DFG) for the collaborative research center "SFB 855" headed by Prof. Dr. Eckhard Quandt. This whole work would be hardly possible without this special funding.

Finally, I would like to thank my wife Melike for her great patience, great support and all her love in the last years, but especially in the last months where I was often too stressed and had little time for her.

Last but not least, I want to express my deep gratitude to my family for their encouragement, great support and all their love throughout my life.

Statement of Authorship

I hereby certify that I have never submitted or published this Ph.D thesis entitled as 'Fabrication and Characterization of single-crystalline InP Membranes for several Applications' neither in complete nor in parts in any doctorate procedure. I have never undergone an oral examination in the framework of a doctorate procedure at any university.

The present thesis has been composed by me without illegal help of others and without using any resources that have not been denoted.Thoughts taken directly or indirectly from other sources have been denoted.

I received support from the following persons in the following fields:

Dr. Jürgen Carstensen, Chair for Allgemeine Materialwissenschaft, CAU zu Kiel: Selection and analysis of the material and production of the manuscript

Dr. Enrique Quiroga-Gonzalez, Chair for Allgemeine Materialwissenschaft, CAU zu: Kiel Conduction and analysis of the battery experiments

No other persons were involved in the preparation of this work. I did not use the help of a doctorate consultant. I neither paid nor provided monetary benefits directly or indirectly to others for work that is connected to the contents of this thesis.
This work was conducted under obedience of the rules for good scientific practice of the German Science Foundation (DFG). This work has already been published in parts in the following journals:

Publications

Scientific journals

1. M.-D. Gerngross, J. Carstensen, and H. Föll. Electrochemical and Galvanic Fabrication of a Magnetoelectric Composite Sensor Based on InP. *Nanoscale Res. Lett.*, **(7)**:379–383, 2012.

2. M.-D. Gerngross and J. Carstensen and H. Föll. Single-Crystalline Membranes in Indium Phosphide: Fabrication Process and Characterization Using FFT Impedance Analysis. *J. Electrochem. Soc.*, **159(11)**:H857–H863 , 2012.

3. M.-D. Gerngross and E. Quiroga-Gonzalez and J. Carstensen and H. Föll. Single-crystalline porous indium phosphide as novel anode material for Li-ion batteries. *J.*

Electrochem. Soc., **159(12)**:A1941-A1948 , 2012.

4. M.-D. Gerngross and S. Chemnitz and B. Wagner and J. Carstensen and H. Föll. Ultra-high aspect ratio Ni nanowires in single-crystalline InP membranes as multiferroic composite. *Phys. Status Solidi RRL*, **7(5)**:352–354 , 2013.

Proceedings

1. M.-D. Gerngross, V. Sprincean, M. Leisner, J. Carstensen, and H. Föll and I. Tiginyanu. Porous InP as piezoelectric component in magneto-electric composite sensors. *ECS Trans.*, **35(8)**:67–72, 2011.

2. M.-D. Gerngross, M. Leisner, J. Carstensen and H. Föll. Porous InP as piezoelectric matrix material in 1-3 magnetoelectric composite sensors. In *Proceedings of the 1st international conference on "Nanotechnologies and Biomedical Engineering" (Volume 1)*, page 16, Technical University of Moldova, Chisinau, 2011.

3. M.-D. Gerngross, V. Hrkac, L. Kienle, J. Carstensen and H. Föll. Formation and characterization of Ni nanostructures in porous InP – from crystallites to wires. In *Proceedings of the 2nd international conference on "Nanotechnologies and Biomedical Engineering" (Volume 1)*, page 43, Technical University of Moldova, Chisinau, 2013.

4. M.-D. Gerngross, E. Quiroga-Gonzalez, J. Carstensen and H. Föll. Characterization of three-dimensional single-crystalline porous InP anodes for Li-ion batteries. *ECS Trans.*, **50(26)**:139–150, 2013.

5. M.-D. Gerngross, J. Carstensen and H. Föll. How to make single-crystalline membranes in indium phosphide. *ECS Trans.*, **50(37)**:121–130, 2013.

Conference Talks

1. M.-D. Gerngross, V. Sprincean, M. Leisner, J. Carstensen, and H. Föll and I. Tiginyanu. Porous InP as piezoelectric component in magneto-electric composite sensors. *219th Meeting of the Electrochemical Society*, Montreal, Canada, 02.-06.05.2011.

2. M.-D. Gerngross, M. Leisner, J. Carstensen, and H. Föll. Porous InP as piezoelectric matrix material in 1-3 magnetoelectric composite sensors. *1st International Conference on Nanotechnologies and Biomedical Engineering*, Chisinau, Moldova, 07.-08.07.2011.

3. M.-D. Gerngross, J. Carstensen, and H. Föll. Electrochemical and galvanic fabrication of a magnetoelectric composite sensor based on InP. *Porous Semiconductors - Science and Technology 2012*, Malaga, Spain, 25.-30.03.2012.

4. M.-D. Gerngross, J. Carstensen, and H. Föll. Fabrication of a single-crystalline porous InP membrane by electrochemical and photoelectrochemical etching. *222th Meeting of the Electrochemical Society*, Honolulu - Hawaii, USA, 07.-12.10.2012.

5. M.-D. Gerngross, J. Carstensen, and H. Föll. Single-crystalline porous indium phosphide as novel anode material for Li-ion batteries. *222th Meeting of the Electrochemical Society*, Honolulu - Hawaii, USA, 07.-12.10.2012.

6. M.-D. Gerngross, V. Hrkac, L. Kienle, J. Carstensen and H. Föll. Formation and characterization of Ni nanostructures in porous InP – from crystallites to wires. *2nd International Conference on Nanotechnologies and Biomedical Engineering*, Chisinau, Moldova, 18.-19.04.2013.

7. M.-D. Gerngross, J. Carstensen and H. Föll. Galvanic fabrication of a 1-3 multifunctional composite based on Ni nanostructures deposited in porous InP . *Euro Intelligent Materials*, Kiel, Germany, 25-27 September, 2013.

Posters

1. M.-D. Gerngross, J. Carstensen, and H. Föll. Fabrication and characterization of a ME composite based on piezoelectric porous InP with magnetostrictive metals. *Materials Science Engineering*, Darmstadt, Germany, 25-27 September, 2012.

2. M.-D. Gerngross, J. Carstensen, and H. Föll. Characterization of Li-ion battery anodes made from single-crystalline InP membranes. *Euro Intelligent Materials*, Kiel, Germany, 25-27 September, 2013.

Kiel, the 15.05.2014 Mark-Daniel Gerngroß